UNIVERSITY OF PADOVA

Department of Physics and Astronomy "Galileo Galilei"

MASTER'S DEGREE IN ASTROPHYSICS AND COSMOLOGY

Observations of the Galaxy Cluster MACS J1752.0+4440 with the Sardinia Radio Telescope

Supervisor
RODIGHIERO GIULIA

Master Candidate
COCCHI SILVIA

Co-supervisor
LOI FRANCESCA

THIS THESIS HAS BEEN DONE IN THE CONTEXT OF THE SCIENTIFIC RESEARCH ACTIVITY OF THE "OSSERVATORIO ASTRONOMICO DI CAGLIARI - ISTITUTO NAZIONALE DI ASTROFISICA"

Abstract

Radio relics are highly polarized, diffuse synchrotron sources typically found in the outskirts of galaxy clusters, where they trace shock waves in the intracluster medium (ICM) generated by cluster mergers. They represent a non-thermal component of the ICM: cosmic-ray electrons re-accelerated to relativistic energies emit synchrotron radiation in the presence of the cluster's magnetic field. The physical mechanisms behind this emission remain poorly understood.

This thesis presents an analysis of MACS J1752.0+4440, a galaxy cluster hosting a remarkable double radio relic system, with components located to the NE and SW of the cluster center. The study is based on new observations with the Sardinia Radio Telescope (SRT) at 18.6 GHz, complemented by archival JVLA data at 1.6 GHz. This is only the third study of a relic system at frequencies up to $\sim$20 GHz, increasing the current high-frequency sample by 50%. Expanding this sample is essential for constraining relic spectra and testing particle acceleration models in the ICM. The integrated spectrum follows a power law consistent with diffusive shock acceleration (DSA), with spectral indices of 1.24 ± 0.03 (NE) and 1.17 ± 0.03 (SW).

Thanks to the reduced Faraday depolarization at $\sim$19 GHz, it was possible to probe the intrinsic polarization of the northern relic, finding an average fractional polarization of $33 \pm 4\%$, with peaks of 60% in the outer regions. JVLA RM synthesis confirms high polarization levels, with averages of $35 \pm 3\%$ (NE) and $41 \pm 4\%$ (SW).

The SRT data also reveal, for the first time, the Sunyaev–Zel'dovich effect at $\sim$19 GHz in this cluster. A Bayesian analysis yields a Compton-y parameter of order 10^{-5}. Combining the SZ-derived density profile with RM measurements gives an average line-of-sight magnetic field strength of $\sim 2\,\mu G$. This result opens the path to follow-up SZ observations at higher frequencies, for example with the MISTRAL receiver, and highlights the potential of combining radio polarimetry with SZ measurements to jointly probe the non-thermal and thermal components of the ICM, providing a key precursor to future SKA-Mid multifrequency studies.

Contents

8 Conclusions   **86**

References   **88**

Appendix   **96**

1

Introduction

Within the filamentary web that constitutes the large scale structure of the Universe, merging galaxy clusters stand out as some of the most energetic events since the Big Bang. These spectacular phenomena have been extensively observed in X-rays, from early missions such as Einstein to more recent ones like Chandra, often followed by optical surveys, including DESI (Dark Energy Spectroscopic Instrument). Moving to the radio band, which is being increasingly explored today, a growing number of merging clusters has been shown to host radio structures with no optical or X-ray counterparts. These structures, still not completely understood, have proven fundamental for constraining the physical processes underlying these phenomena.

Radio observations have revealed the presence of a population of cosmic ray (CR) electrons in the intracluster medium (ICM), not associated with specific radio galaxies as expected, but instead with the ICM itself. These GeV electrons (i.e., Lorentz factors $\gamma > 10^3$) emit synchrotron radiation in the presence of $\sim \mu$Gauss magnetic fields within the ICM.

Over the past decade, significant progress has been made in understanding this non-thermal components through a combination of observational, theoretical, and numerical studies. There is now compelling evidence that ICM shock waves and turbulence produced during cluster mergers can re-accelerate particles to relativistic energies, giving rise to this diffuse non-thermal emission.

Combining radio data with X-ray and optical observations holds immense potential for deepening our understanding of the physical processes driving cluster mergers.

Among those that are called diffused radio sources, radio relics, or radio shocks, are of particular interest: they present themselves extended radio sources typically located in the outskirts of galaxy clusters, often exhibiting high degrees of polarization (typically $\gtrsim 10\%$ at GHz frequencies). The number of well-studied relics remains limited. Due to the steep power-law nature of synchrotron emission, detecting such sources becomes increasingly challenging at higher frequencies. The standard model used to explain the emission from radio relics is the diffusive shock acceleration (DSA). According to this theory, particles scatter off magnetic field irregularities and cross the shock front multiple times, gaining energy with each crossing. This mechanism produces a power-law energy distribution, and if the injection of relativistic particles balances energy losses, the resulting flux density spectrum also follows a power-law with frequency. However, recent high-frequency observations have revealed deviations from this expected behaviour, raising questions about the validity of the DSA model. This highlights the importance of observing radio relics at high frequencies to either confirm or challenge the standard theoretical framework, shedding light on the particle acceleration mechanisms taking place in the intracluster medium.

This thesis presents a study of MACS J1752.0+4440, a merging galaxy cluster that hosts a remarkable example of a double radio relic system, located to the northeast and southwest of the cluster center. It serves as a compelling example of an idealized binary merger scenario, in which equatorial shocks initially form and propagate outward in the plane perpendicular to the merger axis, followed by shocks on the merger axis that explain the double relics. Previous studies on this cluster reached up to 1.7 GHz and showed a behavior consistent

with the DSA model.

The analysis in this work is based on observations conducted with the Sardinia Radio Telescope (SRT) at 18.6 GHz, complemented by archival data from the JVLA at 1.6 GHz. This work represents only the third study of a radio relic system at frequencies reaching up to $\sim$20 GHz, thereby increasing by 50% the current sample available at such high frequencies. Expanding this limited sample is essential for constraining the spectral behavior of radio relics and improving our understanding of the underlying physical mechanisms driving particle acceleration in the intracluster medium. Moreover, since the $\sim$19 GHz data are expected to be minimally affected by Faraday depolarization, it was possible to investigate the intrinsic polarization structure of the northern relic. The southern one was too faint to be detected in polarization at these frequencies. Polarization studies give fundamental information on galaxy clusters magnetic fields, and are become increasingly more implemented nowadays.

This thesis is organized as follows.

Section 2 provides an introduction to galaxy clusters, with a focus on magnetic fields and the associated radiation processes. Particular attention is given to the Sunyaev–Zel'dovich (SZ) effect and to the classification of diffuse radio sources commonly observed in merging systems.

Section 3 is dedicated to radio relics, covering their morphology, spectral characteristics, and the challenges they present to current observational techniques. A review of past observations and publications related to MACS J1752.0+4440 is also included.

Section 4 outlines the fundamental principles of radio emission, the operation of single-dish radio telescopes and interferometers, and details the instrumental characteristics of both the SRT and the JVLA. This section sets the foundation for the data reduction procedures that follow.

Section 5 focuses on the data reduction workflow, from calibration steps to imaging for both SRT and JVLA datasets.

Section 6 presents the data analysis in total intensity: flux measurements and source characterization are performed for both telescopes. This is followed by a spectral fit incorporating literature data and a discussion on multiple possible models applicable.
Notably, this section also reports the unexpected detection of the SZ effect in this cluster and includes a Bayesian estimation of the cluster's physical parameters, culminating in an estimate of the Compton-y parameter. This result paves the way for future SRT observations at higher frequencies, and represents an important precursor study for forthcoming science with SKA (Square Kilometer Array).

Section 7 reports a polarization analysis for both SRT and JVLA data. JVLA data are analyzed through a Rotation Measure (RM) synthesis, fundamental to derive information on the magnetic field in the cluster. The section concludes with rough estimates of the order of magnitude of the magnetic field in the system.

Finally, Section 8 summarizes the key findings of this study and offers a discussion on the prospects and importance of future high-frequency observations of radio relics.

Galaxy clusters

In the intricate structure of the cosmic web, clusters of galaxies stand out as the largest gravitationally bound systems in the Universe, with typical masses of about 10^{15} $M_\odot$, and volumes of about 100 Mpc^3 [43]. These structures are usually found at the nodes of cosmic filaments, like spiders in the cosmic web. Most of the gravitating matter in any cluster is in the form of dark matter ($\sim 80\%$). Some of the luminous matter is in galaxies ($\sim 3\% - 5\%$), the rest is in diffuse hot gas ($\sim 15\% - 17\%$), detected in X-ray through its thermal bremsstrahlung emission. This thermal plasma, consisting of particles of energies of several keV, held together by the cluster's gravitational pull, is commonly referred to as intracluster medium. The hot gas is visible through spatially extended thermal X-ray emission, and it has been studied extensively both for assessing its physical properties and as a tracer of the large-scale structure of the Universe.
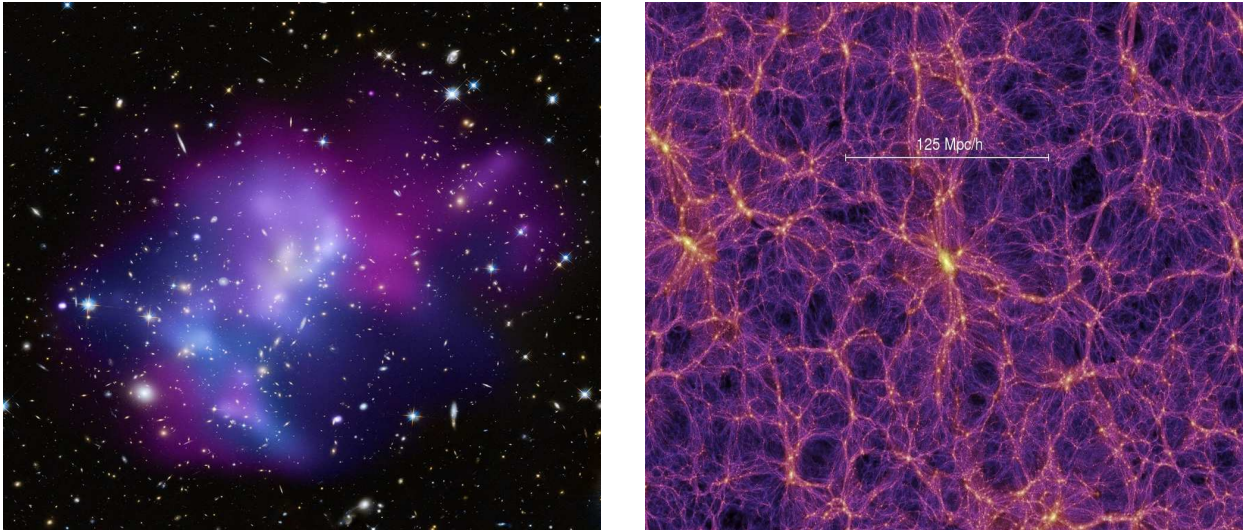
Figure 1. *Left:* MACS J0717.5+3745, an example of galaxy cluster where four separate components have been involved in a collision. Hot gas is shown in an image from NASA's Chandra X-ray Observatory, and galaxies are shown in an optical image from NASA's Hubble Space Telescope. The hot gas is color-coded to show temperature, where the coolest gas is reddish purple, the hottest gas is blue, and the temperatures in between are purple. From `https://science.nasa.gov/mission/hubble/science/science-highlights/mapping-the-cosmic-web/`. *Right:* Simulation of the cosmic web from the Millennium Simulation Project `https://wwwmpa.mpa-garching.mpg.de/galform/virgo/millennium/`.

Galaxy clusters are formed through the gradual hierarchical assembly of matter over cosmic time. In this scenario, smaller units (galaxies, groups and small clusters) form first and merge under gravitational pull to larger and larger units in the course of time. Denser regions form a filamentary structure in the Universe, and clusters are formed accreting matter within filaments, often at their intersection, by a combination of large and small mergers. Major cluster mergers are the most energetic events in the Universe since the Big Bang [116], releasing energies up to $\sim 10^{64}$ ergs on a few Gyr timescale. This energy is

dissipated through low Mach number shocks and turbulence, heating the ICM (e.g. [79]). When clusters collide, their dark matter and galaxies pass through relatively unaffected, but their gas interacts violently – it can be shock-heated, producing shock fronts that raise the gas temperature to tens of millions of degrees. Major mergers can temporarily disturb a cluster's morphology and often create substructures (like double-cluster systems) before relaxing into a more stable state. Over time, repeated mergers and accretion lead to the massive, virialized clusters we observe in the present day. Clusters can thus be divided as either relaxed (undisturbed) or merging (disturbed) systems, depending on their dynamical state.

Another way to characterize galaxy clusters is through their optical observations: centrally dominant clusters are regular and compact, with a dense core of galaxies, a high fraction of elliptical galaxies, a more or less clear morphology-density relation (with more elliptical galaxies in high-density regions), and show signs of mass segregation; spiral-rich clusters have irregular structures, more spread-out galaxies, a similar distribution of early- and late-type galaxies and they seem less dynamically evolved; spiral-poor clusters show intermediate properties [115].

Because clusters are the most massive virialized structures in the Universe and form late in cosmic history, their abundance and properties (as a function of redshift) are highly sensitive to cosmology. Thus, studying cluster evolution - from proto-cluster seeds in the early universe to mature clusters today - provides key tests of structure formation models and the underlying cosmological parameters.

Clusters of galaxies are studied using a variety of observational techniques across the electromagnetic spectrum. Each technique probes a different component of the cluster and reveals unique information:

1. **Optical and Infrared (IR) Observations**. Large cluster surveys (e.g. Sloan Digital Sky Survey) detect clusters as overdensities of galaxies on the sky. The member galaxies can be studied to determine the cluster's distance (via redshift), velocity dispersion, and galaxy population. In addition, gravitational lensing is a key tool: the cluster's mass bends and distorts light from background galaxies, an effect visible in deep optical/IR images as stretched arcs or multiple images. By analyzing these lensing patterns, astronomers can map the distribution of dark matter in clusters and measure the cluster's total mass.

2. **X-ray observations**. Starting with the Einstein satellite and continuing with ROSAT, ASCA, Chandra, e-Rosita and XMM-Newton, X-ray observations have been crucial in characterizing the physics of clusters of galaxies, detecting a relative abundance of substructure and temperature gradients. The X-ray brightness and temperature profiles of a cluster can yield its total mass (under the assumption of hydrostatic equilibrium) and reveal substructures or recent merger activity. High-resolution X-ray spectroscopy can detect emission lines from heavy elements (iron, oxygen, etc.) in the gas, which tell us the gas's metallicity and even the gas's motion via Doppler shifts. High-resolution imaging of cluster cores revealed the presence of optical-line emitting filaments, cavities, and weak shocks possibly created by the AGN (Active Galactic Nuclei) feedback; on larger scales, radio-luminous shocks by mergers have been observed.

   Gas in the central regions of many relaxed clusters has a radiative cooling time that is much shorter than the Hubble time. In the absence of a heating source, the hot gas in the ICM is expected to become dense enough that a cooling flow is expected

to develop, whereby the temperature in the central region of the cluster drops and gas flows inwards (e.g. [81]). X-ray observations do show these temperature drops in some cluster cores (cool-core clusters), but there is much less cool gas than what would be expected from the short radiative cooling time (e.g. [66],[26],[109]). This is known as the cooling flow problem. This implies the presence of energy sources that suppress the cooling, with the most likely being feedback from an AGN. X-ray observations suggest that this is achieved by bipolar radio jets emitted from the AGN, which inject mechanical energy and drive turbulence in the surrounding ICM, as well as inflate large buoyant cavities or 'bubbles' of plasma that can transport low-entropy gas outwards.

Moreover, X-ray observations have revealed previously unseen hydrodynamic phenomena in clusters: classic bow shocks driven by the infalling subclusters, and the unanticipated "cold fronts," or sharp contact discontinuities between regions of gas with different entropies. The ubiquitous cold fronts are found in mergers as well as around the central density peaks in "relaxed" clusters. They are caused by motion of cool, dense gas clouds in the ambient higher-entropy gas, left from merger events between galaxy clusters. These clouds are either remnants of the infalling subclusters, or the displaced gas from the cluster's own cool cores [66]. Cold fronts and merger shocks offer unique insights into the cluster physics, including the determination of the gas bulk velocity, its acceleration, the growth of plasma instabilities, the strength and structure of magnetic fields and the thermal conductivity [56].

3. **Sunyaev–Zel'dovich (SZ) Effect**. The hot electrons in the ICM can be detected through the SZ effect – a distortion of the cosmic microwave background (CMB) spectrum caused when CMB photons inverse-Compton (IC) scatter off the energetic electrons (see section 6.4). The SZ effect is observed as a small temperature decrement in the CMB in the direction of a cluster at radio/microwave frequencies and an increment at millimeter/submm wavelengths. Importantly, the SZ signal of a cluster is essentially redshift-independent, allowing detection of distant clusters. Experiments like the Planck satellite, the Atacama Cosmology Telescope (ACT), and the South Pole Telescope (SPT) have catalogued hundreds of clusters via the SZ effect.

4. **Radio Observations**. To offer a more complete view of the physics of galaxy clusters, a precise physical description of the ICM necessitates also adequate knowledge of the role of non-thermal components, for which detailed evidence comes from radio observations, through the detection of both discrete and diffuse radio sources.

Discrete sources in galaxy clusters include both star-forming galaxies and radio-loud AGN. Star-forming galaxies emit radio waves primarily through synchrotron radiation produced by cosmic rays accelerated in supernova remnants, and thermal free–free emission from HII regions. Their radio luminosity is generally correlated with their star formation rate, making them useful tracers of ongoing star formation activity within clusters. Radio-loud AGNs, or radio galaxies, are instead powered by accretion onto supermassive black holes hosted in old elliptical galaxies. They produce collimated relativistic jets that can extend well beyond the host galaxy. These radio lobes inflate the cavities seen in X-ray images, and radio maps reveal the synchrotron plasma filling those cavities.

Regarding diffuse sources, radio telescopes also reveal the presence of a population of cosmic ray (CR) electrons in the intracluster medium , not associated with specific radio galaxies, but instead with the intracluster medium itself. These GeV electrons

(i.e., Lorentz factors $\gamma > 10^3$) emit synchrotron radiation in the presence of $\sim \mu$Gauss magnetic fields within the ICM. Some clusters host diffuse radio halos or mini-halos (covering the cluster center) or radio relics (at the periphery), believed to be associated with turbulent acceleration or merger shock fronts, respectively.

Galaxy Clusters Properties

Virial mass $M_{vir} \sim 10^{13} - 10^{15} M_\odot$: from hot gas hydrostatic equilibrium, galaxy dynamics gravitational lensing.

Size: estimated from angular extent and redshift distance. Volumes are around 100 Mpc^3.

Dark matter: $\sim$80% of the cluster mass, inferred as $M_{\mathrm{DM}} = M_{\mathrm{total}} - M_{\mathrm{baryonic}}$.

Hot gas: $\sim 15\% - 17\%$ observed in X-rays through imaging and spectroscopy (yields spatial distribution, density, temperature, metallicity, etc.).

Cold gas: usually a negligible mass fraction in clusters, traced from radio to optical observations.

Galaxies: from a few tens in low-mass groups to $\gtrsim 10^3$ in the most massive clusters, $\sim$ 3–5% of the cluster mass, studied mainly through optical and near-IR data, revealing spatial distribution, stellar ages, star formation histories, and dynamics.

Magnetic fields and relativistic particles: $\sim 0.1-10$ μG, detected via synchrotron radiation in radio observations.

2.1 Magnetic fields in Galaxy Clusters

The existence of magnetic fields associated with the intracluster medium in clusters of galaxies is now well established through different methods of analysis, from observations of diffuse synchrotron emission to Faraday rotation measures of background/cluster polarized radio sources. Intracluster magnetic fields permeate galaxy clusters and the intergalactic medium on Mpc-scales. These fields play key roles in particle acceleration and on the process of large scale structure formation, having effects on turbulence, cloud collapse, large-scale motions, heat and momentum transport, convection, viscous dissipation, etc. In particular, cluster magnetic fields inhibit transport processes like heat conduction, spatial mixing of gas, and propagation of cosmic rays [56].

A fraction of galaxy clusters hosts diffuse and extended synchrotron sources that reveal the presence in these systems of $\sim \mu$G magnetic fields and ultra-relativistic electrons at their center (see Vacca et al. [125]). Despite the fact that these sources have been detected only in tens of galaxy clusters, the presence of magnetic fields has been recognized in all galaxy clusters thanks to the Faraday effect (see Section 2.1.3). Magneto-hydro-dynamical simulations suggest that also filaments connecting galaxy clusters should be magnetized with

strengths of nG. This is further backed by observations of synchrotron sources (e.g. Govoni et al. [54]) and rotation measure analyses (e.g. Carretti et al. [22]).

Presently, there is a general agreement on a primordial seed field modified in strength and geometry by structure formation processes. Galaxy clusters mergers, for example, not only accelerate particles but also amplify and compress magnetic fields in the ICM, completely changing their strength and structure. Therefore, intracluster magnetic fields are thought to reflect the present level of turbulence in the environment and, consequently, the evolutionary processes. This is supported by numerical simulations, such as those presented by Vacca et al. [125], which provide a detailed study of magnetic fields in galaxy clusters using both numerical and analytical approaches. These studies find that young, merging galaxy clusters are expected to be less magnetized than older, relaxed systems, since the amplification of magnetic field strength requires long timescales. During the formation of galaxy clusters, a significant amount of energy is released into the intracluster medium, injected on large spatial scales and subsequently cascading to smaller and smaller scales through turbulence. This expectation is confirmed by current radio observations: in merging systems, magnetic fields typically have central strengths of order $\sim \mu$G and fluctuation scales up to a few hundred kpc, whereas in relaxed systems central strengths can reach $\sim 10~\mu$G, with fluctuation scales ranging from a few tens of kpc down to a few kpc or less.

A detailed overview of magnetic field properties in these environments is essential for shedding light on cosmic magnetism but the detection and measurement of these magnetic fields are very challenging due to their extremely weak strengths. High-quality observations obtained with the new generation of radio telescopes in combination with advanced tools of analysis will play a key role in the study of magnetic fields from galaxy clusters to filaments and voids.

Next sections highlight the most relevant processes that allow us to characterize magnetic fields in galaxy clusters.

2.1.1   Synchrotron radiation
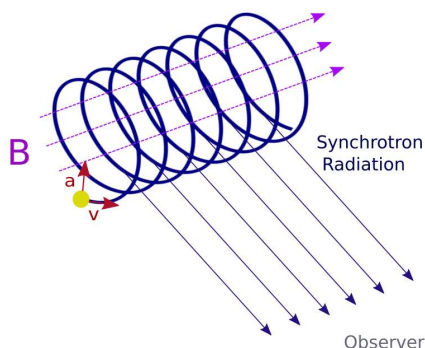
Figure 2. Synchrotron radiation is generated by relativistic electrons spiraling along a magnetic field's lines.

The synchrotron emission is produced by the spiraling motion of relativistic electrons in a magnetic field [56].

Synchrotron radiation is ubiquitous in astronomy. It accounts for most of the radio emission from active galactic nuclei thought to be powered by supermassive black holes in galaxies and quasars, and it dominates the radio continuum emission from star-forming galaxies like our own at frequencies below $\nu \sim 30$ GHz.

The total synchrotron emission from a source provides an estimate of the strength of magnetic fields, while the degree of po-

larization is an important indicator of the field uniformity and structure.

The magnetic force $\vec{F}$ exerted on a particle of charge q with velocity $\vec{v}$ by a magnetic field $\vec{B}$ is given by

$$\vec{F} = \frac{q}{c}\left(\vec{v} \times \vec{B}\right).$$

where c is the speed of light.

The magnetic force is perpendicular to the particle velocity, so $\vec{F} \cdot \vec{v} = 0$. Consequently, the magnetic force does no work on the particle, does not change the particle's kinetic energy $\frac{1}{2}mv^2$, and does not change the component of velocity $v_\parallel$ parallel to the magnetic field. Because both $|\vec{v}|$ and $v_\parallel$ are constant, the magnitude of the velocity component $|\vec{v}_\perp|$ perpendicular to the magnetic field must also be constant.

An electron of energy $\epsilon = \gamma m_e c^2$ (where γ is the Lorentz factor) in a magnetic field B experiences a $\vec{v} \times \vec{B}$ force that causes it to follow a helical path along the field lines, emitting radiation into a cone of half-angle $\sim \gamma^{-1}$ about its instantaneous velocity. To the observer, the radiation is essentially a continuum with a fairly peaked spectrum concentrated near the critical frequency

$$\nu_c = c_1 B sin\theta \epsilon^2. \tag{2.1}$$

The synchrotron power emitted by a relativistic electron is

$$-\frac{d\epsilon}{dt} = c_2 (B sin\theta)^2 \epsilon^2 \tag{2.2}$$

where θ is the pitch angle between the electron velocity and the magnetic field direction while c_1 and c_2 depend only on fundamental physical constants:

$$c_1 = \frac{3e}{4\pi m_e^3 c^5}, \qquad c_2 = \frac{2e^4}{3m_e^4 c^7} \qquad . \tag{2.3}$$

The relativistic electrons in nearly all synchrotron sources have power-law energy distributions, so they are not in local thermodynamic equilibrium (LTE). Consequently, synchrotron sources are often called "non-thermal" sources.

For an homogeneous and isotropic population of electrons with a power-law energy distribution, i.e. with the particle density between ϵ and $\epsilon + d\epsilon$ given by

$$N(\epsilon)d\epsilon = N_0 \epsilon^{-\delta} d\epsilon, \tag{2.4}$$

the total intensity spectrum, in regions which are optically thin to their own radiation, varies as:

$$S(\nu) \propto \nu^{-\alpha} \tag{2.5}$$

where $\alpha = (\delta\text{-}1)/2$ is called spectral index. The synchrotron emission radiating from a population of relativistic electrons in a uniform magnetic field is linearly polarized. In the optically thin case, the degree of intrinsic linear polarization, for a homogeneous and isotropic distribution of relativistic electrons with a power-law spectrum as in eq. 2.4, is

$$P_{int} = \frac{3\delta + 3}{3\delta + 7} = \frac{\alpha + 1}{\alpha + 5/3}. \tag{2.6}$$

In practice, the polarization degree detected in radio sources is much lower than expected by the above equations. A reduction in polarization could be due to a complex magnetic field structure whose orientation varies either with depth in the source or across the angular scale probed by the instrument's resolution. For instance, if one describes the magnetic field inside an optically thin source as the superposition of two components, one uniform B_u, the other isotropic and random B_r, the observed degree of polarization can be approximated by

$$P_{obs} = P_{int} \frac{B_u^2}{B_u^2 + B_r^2}. \tag{2.7}$$

From the synchrotron emissivity it is not possible to derive unambiguously the magnetic field value. A possible way to estimate the magnetic field strength in a radio source is to minimize its total energy content U_{tot}. The total energy of a synchrotron source is due to the energy in relativistic particles (electrons and protons) plus the energy in magnetic fields:

$$U_{\text{tot}} = U_{\text{el}} + U_{\text{pr}} + U_B \quad . \tag{2.8}$$

The magnetic field energy contained in the source volume V is given by:

$$U_B = \frac{B^2}{8\pi} \Phi V \tag{2.9}$$

where Φ is the fraction of the source volume occupied by the magnetic field (filling factor). The electron total energy in the range ϵ_1 to ϵ_2 is:

$$U_{\text{el}} = V \int_{\epsilon_1}^{\epsilon_2} N(\epsilon)\, \epsilon\, d\epsilon = V N_0 \int_{\epsilon_1}^{\epsilon_2} \epsilon^{-\delta+1}\, d\epsilon \quad . \tag{2.10}$$

The synchrotron luminosity L_{syn} can be expressed as:

$$L_{\text{syn}} = V \int_{\epsilon_1}^{\epsilon_2} \left(-\frac{d\epsilon}{dt} \right) N(\epsilon)\, d\epsilon = c_2 (B \sin\theta)^2 V N_0 \int_{\epsilon_1}^{\epsilon_2} \epsilon^{-\delta+2}\, d\epsilon \quad . \tag{2.11}$$

By eliminating $V N_0$ and by writing ϵ_1 and ϵ_2 in terms of ν_1 and ν_2 as per eq. 2.1, we obtain:

$$U_{\text{el}} = c_2^{-1} c_1 \, \widetilde{C}(\alpha, \nu_1, \nu_2)\, L_{\text{syn}}\, B^{-3/2} = c_{12}(\alpha, \nu_1, \nu_2)\, L_{\text{syn}}\, B^{-3/2}, \tag{2.12}$$

where $\sin\theta$ has been taken equal to 1, and

$$\widetilde{C}(\alpha, \nu_1, \nu_2) = \left[\frac{(2\alpha - 2)}{(2\alpha - 1)} \cdot \frac{\nu_1^{\frac{1-2\alpha}{2}} - \nu_2^{\frac{1-2\alpha}{2}}}{\nu_1^{1-\alpha} - \nu_2^{1-\alpha}} \right]. \tag{2.13}$$

The energy contained in the heavy particles (e.g., protons) can be related to the electron energy by assuming:

$$U_{\text{pr}} = k U_{\text{el}} \quad . \tag{2.14}$$

Thus, the total energy as a function of the magnetic field is:

$$U_{\text{tot}} = (1 + k) c_{12} L_{\text{syn}} B^{-3/2} + \frac{B^2}{8\pi} \Phi V \quad . \tag{2.15}$$

The condition of minimum energy occurs when the contributions from magnetic field and relativistic particles are approximately equal:

$$U_B = \frac{3}{4}(1+k)U_{\text{el}} \quad . \tag{2.16}$$

The corresponding total minimum energy is:

$$U_{\text{tot}}^{(\text{min})} = \frac{7}{4}(1+k)U_{\text{el}} = \frac{7}{3}U_B \tag{2.17}$$

The magnetic field for which the total energy content is minimum is:

$$B_{\text{eq}} = \left(6\pi(1+k)c_{12}L_{\text{syn}}\Phi^{-1}V^{-1}\right)^{2/7} \tag{2.18}$$

This value is also referred to as the *equipartition value*. The total minimum energy is then:

$$U_{\text{tot}}^{(\text{min})} = c_{13}\left(\frac{3}{4\pi}\right)^{3/7}(1+k)^{4/7}\Phi^{3/7}V^{3/7}L_{\text{syn}}^{4/7} \tag{2.19}$$

and the corresponding total minimum energy density is:

$$u_{\text{min}} = \frac{U_{\text{tot}}^{(\text{min})}}{V\Phi} = c_{13}\left(\frac{3}{4\pi}\right)^{3/7}(1+k)^{4/7}\Phi^{-4/7}V^{-4/7}L_{\text{syn}}^{4/7} \tag{2.20}$$

where

$$c_{13} = 0.921\,c_{12}^{4/7} \tag{2.21}$$

The constants c_{12} and c_{13}, which depend on the spectral index and the frequency range, are tabulated for CGS units.

Including the K-correction, and assuming $\Phi = 1$, these expressions can be rewritten in terms of observable quantities, more useful for the aim of this thesis.

The minimum energy density of a radio source, expressed in terms of observable quantities, is:

$$u_{\text{min}}\left[\frac{\text{erg}}{\text{cm}^3}\right] = \xi(\alpha,\nu_1,\nu_2)(1+k)^{4/7}\left(\nu_0\,[\text{MHz}]\right)^{4\alpha/7}(1+z)^{(12+4\alpha)/7}\left(I_0\left[\frac{\text{mJy}}{\text{arcsec}^2}\right]\right)^{4/7}(d\,[\text{kpc}])^{-4/7} \tag{2.22}$$

where z is the source redshift, I_0 is the source brightness at frequency ν_0, d is the source depth along the line of sight, $\xi(\alpha,\nu_1,\nu_2)$ is a constant that depends on the spectral index and frequency range (tabulated in [56]). The quantity I_0 can be measured directly from the contour levels of a radio image (for significantly extended sources), or estimated by dividing the total flux by the solid angle of the source. The corresponding equipartition magnetic field is:

$$B_{\text{eq}} = \left(\frac{24\pi}{7}u_{\text{min}}\right)^{1/2} \tag{2.23}$$

While this offers an estimate of the average magnetic field in a cluster, one must be aware of the uncertainties inherent in this determination of the magnetic field strength. The value of k, the ratio of the energy in relativistic protons to that in electrons, depends on the generation mechanism of the relativistic particles, which is not yet well understood and is one of the questions this thesis aims to contribute an answer to. Additional uncertainties arise from the volume filling factor Φ, which is often assumed to be $\Phi = 1$ in the literature. A further challenge is the estimation of the source depth d, which is generally difficult to infer observationally.

2.1.2 Inverse Compton radiation

Relativistic electrons in a radiation field can scatter and transfer energy to photons through the inverse-Compton effect. This process, in which the photon gains energy from the electron, is the inverse of the standard Compton scattering. The frequency of the scattered photon ν_{out} is related to the frequency of the incident photon ν_{in} by:

$$\nu_{\text{out}} = \frac{4}{3}\gamma^2 \nu_{\text{in}} \tag{2.24}$$

In astrophysical applications, the IC effect plays a crucial role because the population of relativistic electrons responsible for synchrotron emission also scatters the ubiquitous 2.7 K CMB photons. Given that synchrotron and inverse-Compton emission originate from the same relativistic electron population, which is assumed to follow a power-law energy distribution (see eq. 2.4), both emissions share the same spectral index α, that relates to the photon index Γ_X of the IC X-ray emission as:

$$\Gamma_X = \alpha + 1 \tag{2.25}$$

When the synchrotron radio and inverse-Compton X-ray emission are produced by the same population of relativistic electrons, the total synchrotron and IC powers are related. The IC emissivity is proportional to the energy density in the photon field, u_{ph}, which for the cosmological blackbody radiation is approximately:

$$u_{\text{ph}} \sim 5 \times 10^{-13}(1+z)^4 \, \text{erg cm}^{-3},$$

whereas the synchrotron emissivity is proportional to the energy density in the magnetic field, $u_B = \frac{B^2}{8\pi}$. This leads to a simple proportionality between synchrotron and IC luminosities:

$$\frac{L_{\text{syn}}}{L_{\text{IC}}} \propto \frac{u_B}{u_{\text{ph}}}. \tag{2.26}$$

Combining the standard formulae of synchrotron and Compton emission mechanisms, the radio and hard X-ray (HXR) detections directly yield an estimate of the average value of the magnetic field in a cluster. Following Blumenthal and Gould [10], and to obtain a more practical formula (as done by Govoni et al. [56]) we relate the monochromatic X-ray flux $S_{\text{IC}}(\nu_x)$ to the integrated X-ray flux $S_{\text{IC}}(E_1 - E_2)$ over the energy interval $E_1 - E_2$, since this is typically the quantity measured from observations:

$$S_{\text{IC}}(E_1 - E_2) \propto S_{\text{IC}}(\nu_x)\frac{E_2^{1-\alpha} - E_1^{1-\alpha}}{1-\alpha}\nu_x^\alpha. \tag{2.27}$$

Assuming a radiation temperature $T = 2.7\,\text{K}$ at $z = 0$, and using commonly used units, the magnetic field can be expressed as:

$$(B[\mu\text{G}])^{1+\alpha} = h(\alpha)\frac{S_{\text{syn}}(\nu_r)\,[\text{Jy}]}{S_{\text{IC}}(E_1 - E_2)\,[\text{erg s}^{-1}\text{cm}^{-2}]}(1+z)^{3+\alpha}\,(0.0545\,\nu_r\,[\text{MHz}])^\alpha\,\left(E_2^{1-\alpha} - E_1^{1-\alpha}\right), \tag{2.28}$$

where the function $h(\alpha)$ is tabulated in Table 2 of [56].

The primary challenges with this method stem from the limitations of current X-ray observations in the hard X-ray regime and from the difficulty in distinguishing thermal and

non-thermal components of the X-ray emission. When the IC X-ray emission is not detected from a radio emitting region, only lower limits to the magnetic fields can be derived.

2.1.3 Faraday Rotation effect

An alternative and complementary instrument to study magnetic fields in the cosmic web is given by the Faraday effect on embedded or background radio galaxies.

The Faraday rotation effect occurs during the propagation of electromagnetic waves through a magnetized plasma. A linearly polarized wave can be decomposed into oppositely-handed circularly polarized components. Magnetic field and free electrons (magneto-ionic medium) behave like a bi-refrangent medium, meaning the refraction index is different for the two components of the linearly polarised wave. These components will have a different phase velocity through the medium, and at the end the phase of the linearly polarised wave will be rotated.

According to the dispersion relation, for a wave of angular frequency ω ($\omega = 2\pi\nu$), the refractive index $n_{L,R}$ of a magnetized dielectric medium has two possible values:

$$n_{L,R} = \left[1 - \frac{\omega_p^2}{\omega^2 \pm \omega\Omega_e}\right]^{1/2}, \tag{2.29}$$

where $\omega_p = \left(\frac{4\pi n_e e^2}{m_e}\right)^{1/2}$ is the plasma frequency, and $\Omega_e = \frac{eB}{m_e c}$ is the electron cyclotron frequency. In the context of studying magnetic fields in galaxy clusters, we are particularly interested in the Faraday rotation of radio sources either located behind the cluster or embedded within it. Radio frequencies dominate the values of ω_p and Ω_e obtained for typical magnetic field strengths ($B \simeq 1\,\mu$G) and gas densities ($n_e \simeq 10^{-3}\,\text{cm}^{-3}$) in the intracluster medium (ICM). In the limit $\omega \gg \Omega_e$, eq. 2.29 can be approximated as:

$$n_{L,R} \approx 1 - \frac{1}{2}\frac{\omega_p^2}{\omega^2 \pm \omega\Omega_e}, \tag{2.30}$$

so that the difference in travel time Δt for the two opposite-handed waves over a path length dl is:

$$\Delta t \approx \frac{\omega_p^2 \Omega_e dl}{c\omega^3} = \frac{4\pi e^3}{\omega^3 m_e^2 c^2} n_e B\, dl. \tag{2.31}$$

The corresponding phase difference is $\Delta\psi = \omega\Delta t$, and the rotation of the polarization plane $\Delta\chi$ over a total path length L is given by $\frac{1}{2}\Delta\psi$, and can be expressed as:

$$\chi_{\text{obs}}(\lambda) = \chi_{\text{int}} + \Delta\chi = \chi_{\text{int}} + \frac{e^3\lambda^2}{2\pi m_e^2 c^4}\int_0^L n_e(l)B_k(l)\, dl, \tag{2.32}$$

where B_k is the component of the magnetic field along the line of sight, and Ψ_{Obs} is the observed polarization angle.

To understand how the term $\Delta\chi$ can be obtained, one quantity to introduce at this point is the *Faraday depth* ϕ [19] :

$$\phi = 0.81\int_0^L n_e(r)\mathbf{B}\cdot d\mathbf{r} \quad \text{rad}\,/\text{m}^2. \tag{2.33}$$

The rotation measure is instead commonly defined as the slope of a polarization angle χ versus λ^2 plot

$$\text{RM} = \frac{d\chi(\lambda^2)}{d\lambda^2} \tag{2.34}$$

where

$$\chi = \frac{1}{2}\tan^{-1}\left(\frac{U}{Q}\right) \tag{2.35}$$

If there is only one source along the line of sight, which in addition has no internal Faraday rotation, and does not suffer from beam depolarization, then the Faraday depth of that source is equal to its rotation measure at all wavelengths, and equation 2.32 becomes:

$$\chi_{\text{Obs}}(\lambda) = \chi_{\text{Int}} + \lambda^2\,\phi = \chi_{\text{Int}} + \lambda^2\,RM, \tag{2.36}$$

The position angle χ_{obs} is an observable quantity, allowing the RM of radio sources to be determined via a linear fit at three or more different wavelengths to eq. 2.36.
The rotation measure can in this case be expressed as:

$$RM = \frac{e^3}{2\pi m_e^2 c^4}\int_0^L n_e(r)\mathbf{B}\cdot d\mathbf{r}\,rad/m^2. \tag{2.37}$$

in practical units (cgs) becomes:

$$\text{RM}\left[\frac{\text{rad}}{\text{m}^2}\right] = 812\int_0^L n_e\left[\text{cm}^{-3}\right]B_k\left[\mu\text{G}\right]\,dl\,[\text{kpc}]. \tag{2.38}$$

A positive Faraday depth implies a magnetic field pointing towards the observer. There may exist many different sources of radiation at different Faraday depths along the same line of sight. A source is Faraday thin if $\lambda^2\,\Delta\phi \ll 1$. $\Delta\phi$ denotes the extent of the source in ϕ. Faraday thin sources are well approximated by Dirac δ-functions of ϕ. A source is Faraday thick if $\lambda^2\,\Delta\phi \gg 1$. Faraday thick sources are extended in ϕ. They are substantially depolarized at λ^2.

Faraday rotation can also cause depolarization: beam depolarization arises when unresolved fluctuations in electron density or magnetic field strength produce RM variations within the observing beam, averaging out the signal; bandwidth depolarization occurs when significant rotation of the polarization angle takes place across the observing bandwidth, or in the channel representing the spectral resolution, reducing the net polarization after averaging; internal depolarization, in contrast, is intrinsic to extended sources, since radiation emitted at different depths experiences different amounts of Faraday rotation, leading to partial cancellation in the summed emission.

A rotation measure image can be obtained by fitting the polarization angle pixel by pixel at multiple frequencies, obtaining an RM map. If the radio source is embedded or in the background of a galaxy cluster and the cluster is the only or the predominant contribution to the Faraday rotation, this image represents a two-dimensional projection of the intracluster magnetic field: the mean value of the rotation measure image probes the magnetic field fluctuations on large spatial scale, while its dispersion reflects the turbulent behavior of the field on small scales.
Moreover, unresolved rotation measure structures in the foreground screen cause a depolarization of the signal of the radio galaxies. Therefore, depolarization of the radio galaxy

signal can be used in conjunction with the analysis of the rotation measure images to constrain the intracluster magnetic field [125].

It is then clear that the importance of the RM resides in the possibility to estimate the component of the magnetic field parallel to the line of sight. Following equation 2.38, the only other element that is needed to accomplish this estimate is a measurement of the intracluster medium density. Such element can be obtained through X-ray measurements, or, as an alternative, from the observation of the Sunyaev-Zel'dovich effect (see Section 2.2).

Measuring Magnetic Fields in Galaxy Clusters

Synchrotron emission $\rightarrow$ Information on $B_\perp$ from the polarization images of the source.

Equipartition theorem $\rightarrow$ Information on the average value of $|\mathbf{B}|$ in the cluster.

Synchrotron/Inverse Compton ratio $\rightarrow$ Average value of $|\mathbf{B}|$ or limit.

Rotation Measure $\rightarrow$ Values of $B_\parallel$ of different sources along the line of sight.

2.2 The Sunyaev-Zel'dovich effect

Observations at high frequency (i.e. >10GHz) can be affected by the Sunyaev-Zel'dovich effect, which consists of a inverse-Compton interaction between CMB photons and thermal ICM particles.
As a result, the synchrotron emission associated with cluster-embedded sources is reduced from true values because the background CMB emission is shifted towards higher frequencies [8], adding a "negative" contamination to the flux density of these sources (Figure 3).
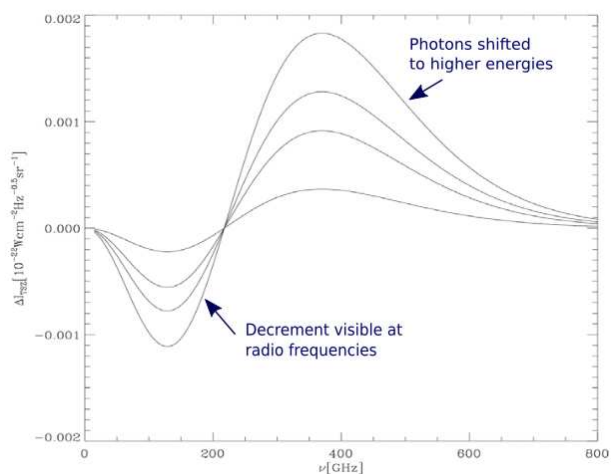
Figure 3. Thermal SZ effect for $y = 10^{-4}$, 7×10^{-5}, 5×10^{-5}, 2×10^{-5}, from Battistelli et al. [7].

The basic physics of the Sunyaev-Zel'dovich effect is straightforward (see Birkinshaw [8] for a detailed discussion). Clusters of galaxies often possess masses exceeding $3 \times 10^{14} \, M_\odot$, with effective gravitational radii, $R_{\rm eff}$, on the order of megaparsecs. Gas in hydrostatic equilibrium within a cluster's gravitational potential well must attain an electron temperature T_e given by:

$$k_{\rm B} T_e \approx \frac{GMm_p}{2R_{\rm eff}} \approx 7 \left(\frac{M}{3 \times 10^{14} \, M_\odot} \right) \left(\frac{R_{\rm eff}}{\rm Mpc} \right)^{-1} {\rm keV}, \qquad (2.39)$$

where $k_{\rm B}$ is the Boltzmann constant, G is the gravitational constant, M is the cluster mass, and m_p is the proton mass.

At such temperatures, thermal emission from the gas appears in the X-ray part of the spectrum, primarily composed of thermal bremsstrahlung and line radiation [114]. Approximately a quarter of the mass in galaxy clusters is in the form of distributed gas, and the gas density is sufficiently high that clusters are luminous X-ray sources, with the bulk of the X-rays produced via bremsstrahlung rather than line emission.

For the low-energy scatterings involving ions and photons from the CMB, the cross-section is the Thomson scattering cross-section, σ_T, leading to a scattering optical depth:

$$\tau_e \approx n_e \sigma_T R_{\text{eff}} \sim 10^{-2}, \tag{2.40}$$

where n_e is the electron number density. In each scattering event, the photon's frequency is slightly shifted, with up-scattering being more probable. On average, a scattering induces a mean fractional change in photon energy:

$$\left(\frac{\Delta\nu}{\nu}\right) \approx \frac{k_{\text{B}} T_e}{m_e c^2} \sim 10^{-2}, \tag{2.41}$$

where m_e is the electron mass and c is the speed of light. Consequently, the overall change in the brightness of the CMB due to inverse Compton (Thomson) scattering is about one part in 10^4.

Considering thermal electrons scattering with CMB, three are primary sites for such distortions:

- the atmospheres of galaxy clusters, where the amplitude of the SZ signal correlates with other observable properties of the clusters.

- the ionized content of the Universe as a whole,

- ionized gas in the vicinity of the observer.

If a cluster atmosphere contains gas with an electron concentration $n_e(r)$, then along a particular line of sight, the scattering optical depth, Comptonization parameter, and X-ray spectral surface brightness are given by:

$$\tau_e = \int n_e(r)\sigma_T \, dl, \tag{2.42}$$

$$y = \int n_e(r)\sigma_T \frac{k_{\text{B}} T_e(r)}{m_e c^2} \, dl, \tag{2.43}$$

$$b_X(E) = \frac{1}{4\pi(1+z)^3} \int n_e^2(r)\Lambda(E, T_e) \, dl, \tag{2.44}$$

where z is the redshift of the cluster, $\Lambda(E, T_e)$ is the spectral emissivity of the gas at observed X-ray energy E, encompassing both line and continuum processes. The factor of 4π arises from the assumption of isotropic emissivity, while the $(1+z)^3$ factor accounts for cosmological transformations of spectral surface brightness and energy.

In many cases, it is convenient to introduce a parameterized model for the properties of the scattering gas in the cluster, and to fit the values of these parameters to the X-ray data. This allows analytical evaluation of integrals such as equation 2.43, thereby enabling predictions of the Sunyaev-Zel'dovich effect profile across the cluster.

One particularly simple and popular model is the *isothermal β-model*, in which the electron temperature T_e is assumed to be constant throughout the cluster, and the electron number density follows a spherical distribution given by:

$$n_e(r) = n_0 \left(1 + \frac{r^2}{r_c^2}\right)^{-3\beta/2}, \tag{2.45}$$

where n_0 is the central electron density, r_c is the core radius, and β is a dimensionless parameter that describes the slope of the profile at large radii [24, 25].

Using this model, both the X-ray brightness profile and the Compton y-parameter can be evaluated along lines of sight through the cluster, allowing joint fits to X-ray and SZ observations to constrain the thermal structure of the intracluster medium.

At cm wavelengths, in the Rayleigh-Jeans approximation, the SZ-effect manifests as a decrement in the CMB temperature of $\Delta T_{RJ} = -2 \cdot y \cdot T_{CMB}$. The intensity decrement at radio frequencies according to Birkinshaw [8] and Basu et al. [6], is:

$$\left(\frac{\Delta I_{SZ}}{\text{mJy/beam}}\right) = \frac{1}{340}\left(\frac{\nu}{\text{GHz}}\right)^2\left(\frac{\Delta T_{\text{RJ}}}{\text{mK}}\right)\left(\frac{\Omega_{\text{beam}}}{\text{arcmin}^2}\right) \tag{2.46}$$

where ν is the observing frequency in GHz and Ω_{beam} is beam solid angle in square arcminutes.

2.3 Diffuse radio emission in galaxy clusters

A number of galaxy clusters are known to host extended, diffuse synchrotron sources classified as radio halos, relics, and mini-halos (see van Weeren et al. [132] for the most recent review). These sources show no direct connection to individual cluster galaxies but are instead associated with an intracluster medium (ICM) that contains GeV cosmic-ray (CR) electrons (i.e., with Lorentz factors $\gamma > 10^3$) that emit synchrotron radiation in the presence of $\sim \mu$G magnetic fields.

Galaxy clusters provide a unique environment to study the physics of particle acceleration in collisionless, turbulent plasmas, and low Mach number shocks. Furthermore, diffuse radio emission from clusters can serve as a signpost of ICM shocks and turbulence, which are often difficult to detect and characterize at other wavelengths.

Since shocks and turbulence trace the dynamical state of the ICM, radio observations also provide a probe of the cluster's evolutionary stage, which is important for our understanding of structure formation in the Universe. Finally, diffuse radio emission can act as a complementary method to discover clusters that may be missed by X-ray, Sunyaev–Zel'dovich, or optical surveys.

Over the past decade, significant progress has been made in understanding the non-thermal component in galaxy clusters through observations, theoretical models, and numerical simulations. There is now compelling evidence that ICM shock waves and turbulence can re-accelerate particles to relativistic energies, thereby sustaining the non-thermal cosmic ray population in the ICM.

The presence of extended synchrotron emission also implies the existence of large-scale ICM magnetic fields with strengths on the order of 0.1–10 μG . These magnetic fields play a crucial role in particle acceleration processes. Furthermore, they inhibit transport phenomena such as heat conduction, the spatial mixing of gas, and the propagation of cosmic rays. Despite their importance, the detailed properties of these magnetic fields remain poorly

constrained due to the difficulties involved in measuring them [e.g. 56].

Diffuse cluster radio sources have historically been divided into three main classes: relics, halos, and mini-halos.

Radio halos are centrally located diffuse sources in merging clusters. They do not have any optical counterparts. Mini-halos are smaller in size and are typically located in relaxed, cool-core clusters that also host a powerful radio galaxy associated with the brightest cluster galaxy (BCG). Radio relics have been defined as extended sources that show high levels of polarization ($\gtrsim 10\%$ at GHz frequencies) and are located in the cluster periphery. Similar to radio halos, relics lack optical counterparts. Relics were further subdivided by [71] into Radio Gischt — large, Mpc-size sources that trace particles accelerated at shocks via Fermi-I processes, Radio Phoenices — AGN fossil plasma that is compressed and revived by merger shocks, and AGN Relics — fossil radio plasma that is passively evolving from an AGN that has ceased activity. For radio relics, the boundaries between these categories are not always clear, and the term *relics* itself is somewhat misleading, as large relics may actually be "young" sources undergoing ongoing re-acceleration.

The most recent review from van Weeren et al. [132] proposes to classify cluster emission into three broad categories:

1. **Radio halos** are extended sources that roughly follow the ICM baryonic mass distribution. This class includes both giant radio halos and mini-halos. It also encompasses potential "intermediate" or "hybrid" radio halos with properties that fall between those of classical giant halos and mini-halos. A key characteristic of radio halos is their non-localized nature; that is, particle re-acceleration or production occurs throughout a significant volume of the cluster and is not tied to a specific, localized shock. In terms of physical interpretation, these "global" sources likely trace Fermi-II processes and/or secondary electron production. They trace widespread turbulent re-acceleration in the ICM after mergers.
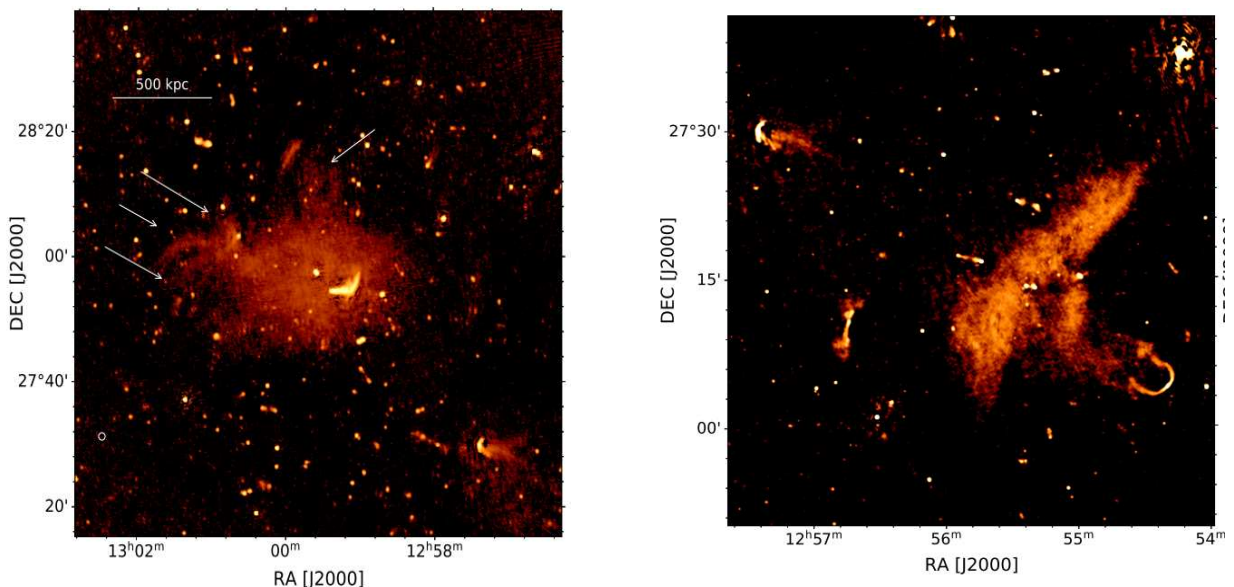
Figure 4. *Left:* Example of radio halo, from the Coma cluster. The halo core and the radio galaxies, both, of Coma and of the field are visible. White arrows mark the filaments (3 arrows on the left) and the radio-loop (arrow on top-right). *Right:* Radio relic region of the Coma cluster. Both images are from Bonafede et al. [15].

2. **Cluster radio shocks / radio relics** are extended diffuse sources that trace particles that are re-accelerated at ICM shock waves (see Figure 5 for examples). This classification does not necessarily require diffusive shock acceleration or Fermi-I mechanisms, that are the main candidates for acceleration mechanisms in radio relics. Thus, cluster radio shocks are defined observationally and are not strictly tied to the specific acceleration process. More on these sources is reported in Section 3.

3. **Revived AGN fossil plasma sources: phoenices and GReETs.** This class includes sources that trace AGN radio plasma that has been re-energized by processes in the ICM, unrelated to the activity of the original radio galaxy. The defining observational features of these sources are their AGN origin and ultra-steep radio spectra, indicative of significant radiative losses. These sources often display irregular, filamentary morphologies and relatively small physical sizes (typically no more than a few hundred kpc), with very steep spectra. *Gently re-energized tails* (GReETs; [29]) are tails of radio galaxies that appear revived, exhibiting unexpected spectral flattening contrary to the usual steepening due to electron energy losses. With the advent of new and upgraded low-frequency radio telescopes, the nature of these revived fossil plasma sources is expected to become clearer in the coming years.

An up-to-date list of known diffuse cluster radio sources is provided by the radio astronomical database maintained by the Observatory of Hamburg [1].

---

[1] http://galaxyclusters.com, [132]

3

Radio relics

Mergers between galaxy clusters produce shocks in the ICM which are associated with diffuse synchrotron sources that are called radio relics (see van Weeren et al. [132] and Feretti et al. [43] for the most recent reviews). These sources are found mostly in the periphery of galaxy clusters, characterized by low surface brightness, sizes of the order of Mpc, steep spectra ($\alpha \gtrsim 1$), and high degrees of polarization ($\gtrsim$ 20–30%) at 1.4 GHz.

3.1   The physics behind radio relics

Observations of relics provide the best indications for the presence of μG level magnetic fields and relativistic particles in cluster outskirts, providing evidence for the (re-)acceleration of relativistic particles at shock fronts at large distance (Mpc scale) from the cluster centers.

Radio relics are widely believed to originate from merger-induced shock waves propagating through the ICM. Shocks of the large-scale gas motion are expected at the typical peripheral locations of relics, either resulting from cluster mergers, or from steady state accretion shocks by gas falling into the cluster potential. Also, the electrons responsible for the observed synchrotron emission must be accelerated in regions where magnetic fields are present. Therefore the magnetized plasma, accumulated behind the shock or left behind as a remnant of a radio galaxy, could furnish this acceleration region and should also increase the efficiency of the acceleration mechanism [41].
While the connection between shocks and radio relics is widely accepted, many details of the acceleration mechanism itself are yet unclear. One major issue is the lack of understanding of the acceleration efficiencies at work. The acceleration efficiency measures how much kinetic energy dissipated at the shock goes into the acceleration of the particles, i.e. electrons in case of radio relics.
The link between mergers and radio relics supports the diffusive shock acceleration (DSA) as a mechanism of (re-)acceleration of cosmic-ray particles up to the $\sim$GeV energies required to explain the observed emission. This process is based on the original idea of Fermi [44], according to which particles are scattered upstream and downstream of the shock by plasma irregularities, gaining energy at each reflection. In other words, according to DSA, particles scatter from magnetic field inhomogeneities and they cross the shock wave back and forth gaining energy at each crossing. The DSA mechanism predicts a power-law energy distribution and, if the cooling of the particles is balanced by the injection of relativistic particles, a power-law behavior of the flux density as a function of frequency.
Following the calculations by Blandford and Eichler [9], the slope δ_{inj} of the accelerated electrons (i.e., the injection spectrum) in a power-law momentum distribution of CRe in the form

$$N_{\mathrm{inj}}(p) = K_e p^{-\delta_{\mathrm{inj}}}, \tag{3.1}$$

which is motivated by the single power laws generally used to describe the integrated radio

spectra of radio relics (e.g.[132]), is

$$\delta_{\text{inj}} = \frac{2M^2 + 1}{M^2 - 1},$$

(3.2)

and it depends only on the shock's Mach number.

Under stationary conditions and assuming that the physical conditions in the downstream regions do not change with distance from the shock, the electron spectrum integrated in the downstream region follows a power law with a slope of $\delta = \delta_{\text{inj}} + 1$. Thus, the integrated synchrotron spectrum is connected with the shock Mach number via

$$\alpha = \frac{M^2 + 1}{M^2 - 1} \equiv \alpha_{\text{inj}} + \frac{1}{2}.$$

(3.3)

Relativistic electrons just behind the shock immediately (within $\sim 10^7$ yr) lose their energy via radiative cooling and energy loss via inverse-Compton scattering. Since the cooling timescale of electrons is shorter than the lifetime of the shock, spectral curvature develops, which is called the "ageing effect". As a result, the index of the integrated spectrum decreases at the high-energy end by about 0.5 from α_{inj} for a simple DSA model [1].

This implies that such a spectral steepening should be observable. This is consistent with the idea that some relics are detected before the steepening occurs, while others are observed afterward. Ensslin et al. [41] present a list of relics and indicate, based on previous observations and a simple DSA model, where the steepening is expected (this point in the spectrum is indicated as break frequency).

As a consequence of the above relations, DSA predicts that for strong shocks ($M \to \infty$) the asymptotic behavior of the spectral index is $\alpha \to 1$ (and $\alpha_{\text{inj}} \to 0.5$), while for weak shocks ($M \sim 3 - 5$) it is $\alpha > 1$ (and $\alpha_{\text{inj}} > 0.5$). This trend has been observed in a large number of radio relics suggesting that these sources are produced by the DSA mechanism.

However, it is currently debated if the acceleration starts from the thermal pool, following the one accepted as the standard scenario(e.g. [41]) or from a population of mildly relativistic electrons (re-acceleration scenario, e.g. [68]). The standard scenario has successfully reproduced many of the observed properties of relics, but some major difficulties remain, due to multiple observations, as reported in the following.

1. Mach numbers form X-ray observations

If relics are in fact generated by merger activity or accretion flows from surrounding large-scale structures (e.g., [41]), shock waves should coexist at the location of radio shocks.

From X-ray observations, the intensity of shock structure can be estimated from the Rankine-Hugoniot jump condition [74]. Assuming a ratio of specific heats $\gamma = 5/3$, we have:

$$\frac{T_2}{T_1} = \frac{5M^4 + 14M^2 - 3}{16M^2},$$

(3.4)

$$\frac{\rho_2}{\rho_1} = \frac{4M^2}{M^2 + 3},$$

(3.5)

where the subscripts 1 and 2 refer to the pre- and post-shock intracluster medium (ICM) density ρ or temperature T, respectively.

On the other hand, based on the assumption of simple diffusive shock acceleration (DSA)

theory, the Mach number can also be estimated from the radio injection spectral index (α_{inj}) via:

$$M_{\text{radio}} = \sqrt{\frac{2\alpha_{\text{inj}} + 3}{2\alpha_{\text{inj}} - 1}}. \tag{3.6}$$

In principle, both X-ray and radio approaches are independent methods to characterize the shock strength, meaning shock strengths inferred from these different wavelength regimes should match each other if the underlying assumptions are correct. Therefore, the comparison of the shock properties inferred from X-ray and radio data is an important tool to investigate shock-related ICM physics. However, the Mach numbers derived from X-ray observations are often signficantly lower than those derived from the overall radio spectrum (e.g. [20, 17]). For such weak shocks, the DSA mechanism is not efficient enough to accelerate particles up to GeV energies from the thermal pool.

2. Breaks at high frequencies

High-frequency observations pose particular challenges: radio shocks have steep-spectra making them very faint at high-frequencies, and radio interferometers are typically able to sample up to a certain scale due to their minimum baseline at high frequency, and thus have difficulty in detecting extended diffuse sources. The spectra of some relics are reported to show a spectral break above 10 GHz [124, 122], which is incompatible with the power-law spectrum predicted by DSA theory. However, the latest studies on high-frequency single-dish observations from Loi et al. [78] and Rajpurohit et al. [107] do not corroborate this finding, showing instead a perfect power-law behavior of the "toothbrush" and "sausage" relics.

3. Acceleration efficiency

A power-law energy distribution from the thermal pool CRe energies relevant for the synchrotron emission may require an unphysical acceleration efficiency. Botteon et al. [17] demonstrate that DSA of thermal electrons becomes problematic for weak shocks, that is, those of typically M $\sim$ 2 - 2.5, and shocks of this strength are relatively common in the ICM and in radio relics.

Following [131], the kinetic energy flux that becomes available at the shock (ΔF_{KE}) is:

$$\Delta F_{\text{KE}} = \frac{1}{2}\rho_1 v_s^3 \left(1 - \frac{1}{C^2}\right), \tag{3.7}$$

where v_s is the shock speed , C the compression factor for the shock and ρ_1 is the upstream density. Part of this energy can be converted into electron acceleration and then into synchrotron and inverse Compton (IC) emission.

The efficiency of electron acceleration η_e that is necessary at the shock to explain the observed synchrotron luminosity, is defined as the fraction of the kinetic energy flux at the shock that is channelled into the supra-thermal and relativistic electron component, i.e.,

$$\frac{1}{2}\eta_e \rho_1 v_s^3 \left(1 - \frac{1}{C^2}\right) = \epsilon_e v_2^2, \tag{3.8}$$

where ϵ_e and v_2 are the energy density of accelerated electrons and the downstream velocity of the flow, respectively.

The required efficiency η_e decreases as the strength of the magnetic field in the relic region (downstream) increases, as a progressively larger fraction of the shock energy flux is

radiated into the radio band via synchrotron emission. Large values of the magnetic field $(B \gtrsim 10 \, \mu\text{G})$ are, however, excluded under the assumption that the thermal pressure is larger than the magnetic field pressure downstream.

More than several percent of the kinetic energy flux crossing the shock must be converted into acceleration of relativistic electrons. This argues against standard diffusive shock acceleration and provides support for alternative mechanisms.

Something that is particularly well supported is the idea of re-acceleration: the shock wave might boost a pre-existing population of mildly relativistic "seed" electrons (perhaps injected by previous AGN activity or past structure-formation shocks) rather than being accelerated directly from the thermal electron population.

Specifically, some alternative scenarios to the DSA [132] are briefly reported in the following:

1. By contrast to acceleration at time invariant shocks, which results in power-law integrated spectra, curved spectra could be a natural result of spherically-expanding ICM shocks [69].

2. The simple radio shock formation model assumes that the associated shock wave injects thermal electrons. A scenario where the shock predominantly injects non-thermal fossil electrons, pre-accelerated by previous AGN activity, could also reproduce the observed curved radio spectra. Re-acceleration can dramatically raise the efficiency of producing radio-bright electrons. Recent simulations and observations support this: the low Mach ($\mathcal{M} \sim 2$) shocks inferred in many relics would struggle to accelerate thermal particles to the needed energies, but if fossil cosmic rays are present, the shock can re-energize them into the radio-emitting regime [40].

3. The downstream steepening, as well as the steepening of the integrated spectrum, can be recovered if there is non-uniform magnetic field in the downstream area of the shock or if the electrons, after shock acceleration, are further re-accelerated by turbulence, as reported by Donnert et al. [34].

4. Multishock scenarios have been proposed by Smolinski et al. [120]. Particles that pass through multiple shocks contribute significantly to the overall luminosity of a radio relic and greatly boost the effective acceleration efficiency.

5. Enßlin and Gopal-Krishna [39] argue that fossil radio plasma with an age of even up to 2 Gyr can be revived by compression in a shock wave of large-scale structure formation, caused during the merging events of galaxy clusters, or by the accretion onto galaxy clusters. They considered this a highly plausible explanation for the observed cluster radio relics.

To explain the observational results without resorting to these alternative scenarios, several solutions have been proposed. For example, it is possible that the X-ray derived Mach numbers are somewhat underestimated due to unfavorable viewing angles and the complexity of the shock surface. The surfaces of merger shocks are not smooth but are highly intermittent, with regions of high Mach numbers forming filamentary structures. This inhomogeneity means that different observation methods might be sampling different parts of the shock surface. Specifically, X-ray observations tend to pick up parts of the shock with higher energy flux but lower Mach numbers, while radio emissions, given the fact that the shock acceleration efficiency is thought to be a strong function of shock Mach number,

are more likely to originate from regions with higher Mach numbers [57]. Therefore, the cosmic-ray-energy-weighted Mach number is expected to be higher than the kinetic-energy-weighted Mach number.

Difficulties and possible biases with radio based measurements are discussed in Stroe et al. [121], van Weeren et al. [131]. These include:

- spectral aging distorting the injection index;

- resolution limits and beam smearing effects.

Akamatsu et al. [1] investigated possible systematic errors associated with X-ray observations:

- projection effects that can lead to the underestimation of the Mach numbers from X-ray observations;

- an underestimation of the post-shock temperature with electrons not reaching thermal equilibrium is possible;

- clumpiness and inhomogeneities in the ICM will lead to nonlinearity of the shock-acceleration efficiency and a nonuniform Mach number.

3.2 Morphology
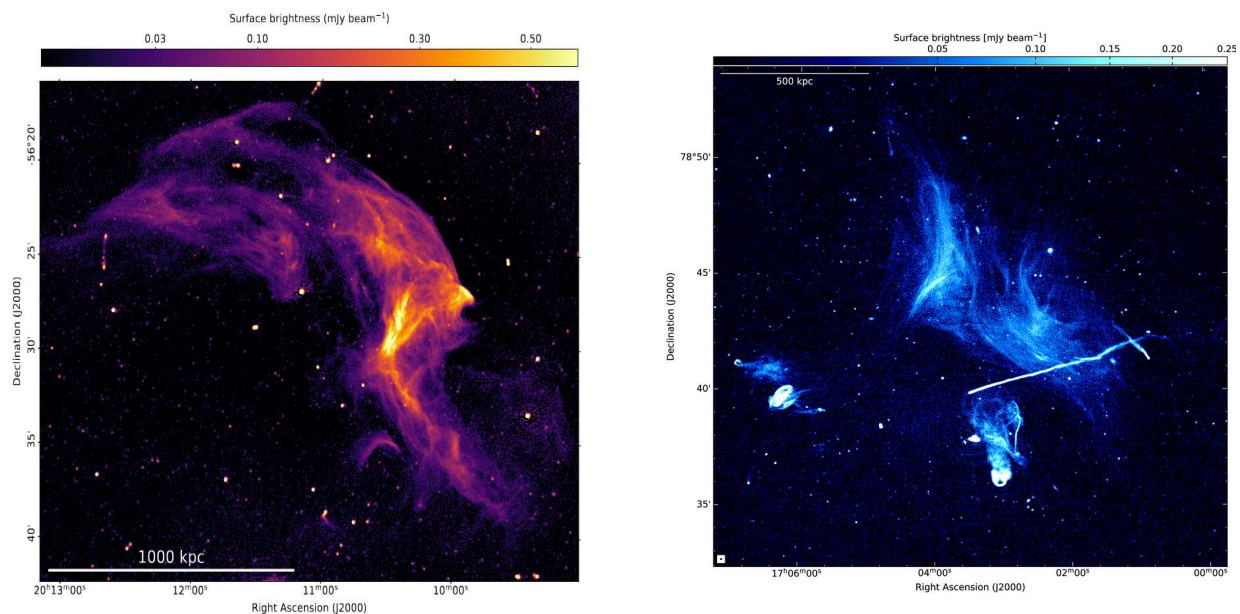
Figure 5. *Left:* Abell 3667 northern relic image from MererKAT data [30], an example of textbook radio relic system. *Right:* Abell 2256 and its filamentary structure, high resolution uGMRT image from [108].

Cluster radio shocks typically have elongated shapes: examples are the sources found in the Coma cluster [50], CIZA J2242.8+5301 [129], Abell 3667 [113, 64], Abell 115 [55], and Abell 168 [36]. These elongated shapes are expected for sources that trace shock waves in the cluster outskirts and are seen close to edge-on. Examples of radio shocks that are less

elongated are found in Abell 2256 [27] and ZwCl 2341.1+0000 [5, 135].
Sizes roughly range between 0.5 to 2 Mpc.

Most large radio shocks that are found in the cluster outskirts show asymmetric transverse brightness profiles, with a sharp edge on the side away from the cluster center. On the side of the cluster center, the emission fades more gradually.
Deep high-resolution observations of large elongated radio shocks have also revealed a significant amount of filamentary substructures, as in Abell 2256 ([124],[108]), CIZA J2242.8+5301 [129], the Toothbrush relic (e.g. [107]) and MACS J0717.5+3745 [42, 128]. The nature of the filamentary structures is not fully understood. One possibility is that they trace changes in the magnetic field. Alternatively, they could reflect the complex shape of the shock surfaces. The filamentary morphology of cluster radio shocks seems to be ubiquitous because all radio shocks that have been studied with good signal-to-noise and at high resolution display them. Vazza [137] investigated why cluster radio shocks are mostly found in the periphery of clusters using simulations. They showed that the radial distribution of observed radio shocks can be explained by the radial trend of dissipated kinetic energy in shocks, which increases with cluster-centric distance up to half of the virial radius. Simulations [118, 137, 13, 119, 136, 89, 141] also produce large-scale radio shock morphologies that reasonably match observations.

3.3   Radio spectra

The integrated radio spectra of cluster radio shocks display power-law shapes (see Section 3.5) of the form

$$S_\nu \propto \nu^{-\alpha} \tag{3.9}$$

where S_ν is the flux density (usually measured in Jansky), ν the frequency of the observations, and α the spectral index.
Spectral indices usually range from about 1.0 to 1.5 [13, 43, 32]. One notable exception of a flatter integrated spectrum, with good observational coverage, is Abell 2256, where the spectral index is about 0.8 [124]. This seems to indicate this relic has been observed at frequencies below the break frequency, that the relic is young (as discussed below) or that additional mechanism are at play here.

Cluster radio shocks often show a clear spectral index gradient across their width. The region with the flattest spectral index is located on the side away from the cluster center. Towards the cluster center, the spectral index steepens. This is well in accord with the standard scenario that explains the physics of radio relics, the Diffusive Shock Acceleration theory [35]. The theory predicts the outer edge to be sharper due to the better confined plasma at the shock side, and it should have a lower than average spectral index, since the electrons at this location are re-accelerated recently [41]. The inner edge is instead expected to be smoother and to have a higher than average spectral index. The reason for the latter is that the re-accelerated electrons within the radio plasma seen there, at a position more distant to the shock, had more time for cooling. Observationally, this appears as a spectral index gradient across relics: the outer edge (just behind the shock) shows a flatter spectrum (freshly accelerated electrons), whereas toward the cluster interior the spectrum becomes progressively steeper due to radiative cooling.
The majority of well-studied cluster radio shocks, including both single shocks and double

relics, exhibit this behavior. The maximum extent of relic emission is likewise limited by electron cooling – eventually the oldest electrons no longer radiate at observable frequencies, defining the relic's thickness. The age of electrons determines the break frequency of the radio spectrum. The break occurs due to cooling after acceleration and is related to the distance from the shock.

As introduced in Section 3.1, the combination of continuous acceleration at the shock and downstream cooling leads to a curved overall spectrum for relics. At low frequencies, the emission typically follows a power-law governed by freshly accelerated electrons, while at higher frequencies, a spectral steepening or cutoff arises due to radiative losses. This behavior can be modeled using synchrotron aging models such as the CI (Continuous Injection), JP (Jaffe–Perola) [61] or KP (Kardashev–Pacholczyk) models [70, 97].
If no spectral steepening is observed, the relic might be young, so electrons have not had enough time to cool significantly, or the break frequency is out of the observed range of frequency, causing the spectrum to appear unbroken within the available data.

3.4 Polarization

Cluster radio shocks are among the most polarized sources in the extragalactic sky. Very elongated radio shocks usually show the highest polarization fractions, which is expected if they trace edge-on shock waves [41]. For example, CIZA J2242.8+5301 exhibits polarization fractions of approximately 50% or more at GHz frequencies in some parts of the radio shock [129].
In a shock, the turbulent dynamo and compression of field lines can increase the field strength by factors of a few, especially for the field components tangential to the shock front. For a typical cluster peripheral field of $B \sim 0.5$ μG, a compression by a factor of ~ 3 (for $\mathcal{M} \sim 2$–3) could locally boost it to a few μG in the shock downstream region. This amplification is supported by the high polarization of relics: the post-shock field is not only stronger but also coherently aligned along the shock plane [12, 129, 13, 99]. Such ordered fields produce the strong polarized radio emission observed (20–60% fractional polarization), and are a natural outcome of shock compression (which flattens and aligns field lines) plus shock-generated turbulence. For large cluster radio shocks, the intrinsic polarization angles, corrected for the effect of Faraday Rotation, are actually found to be well aligned. Only a few Faraday rotation studies have been conducted so far on radio shocks. They indicate that for radio shocks projected at large cluster-centric radii, the Faraday Rotation is mostly due to the Galactic foreground. In contrast, Faraday Rotation induced by the intracluster medium can be observed in parts of shocks at smaller cluster-centric radii [42, 101, 127, 95]. From the limited number of studies available, it seems that large cluster radio shocks experience strong depolarization at frequencies $\lesssim$1 GHz [18, 101, 96]. Therefore, high-frequency observations (above $\sim$2 GHz) are best suited to probe the intrinsic polarization properties of radio shocks. For example, the fractional linear polarization of the main "Sausage" and "Toothbrush" radio shocks averages around 40% at 5-10 GHz, reaching up to 70% in localized regions [77, 73], a result confirmed up to 19 GHz by [78, 107].

3.5 Observations of radio relics

Over the past 10 years, new and upgraded radio facilities have revolutionized our understanding of radio relics. Instruments like LOFAR (Low Frequency Array) [126], MWA (Murchison Widefield Array) [123], ASKAP (Australian SKA Pathfinder) [60], MeerKAT [65], and the upgraded VLA (Very Large Array) have collectively enabled discoveries of many relics and detailed characterization of known ones.
A list of known cluster radio relics is reported in Table 1, as provided by Lee et al. [75].

The Low Frequency Array has been central to recent relic discoveries, operating in the 20–200 MHz band with high sensitivity to steep-spectrum sources. The LoTSS-DR2 survey [117] identified relics in 26 Planck-selected [102] clusters (many previously unknown), suggesting that roughly 10% of massive clusters host detectable relics. LOFAR is especially effective at revealing relics missed at GHz frequencies due to their ultra-steep spectra. It has enabled detailed spectral mapping of well-known systems like the Sausage and Toothbrush relics, revealing spectral curvature and gradients consistent with aging electrons behind merger shocks. One of the most remarkable findings is a 3.5 Mpc relic in ClG 0217+70 [58], the largest known to date, with complex morphology and a spectral steepening indicative of fossil electron re-acceleration. Beyond individual cases, LOFAR is enabling population studies and has uncovered diffuse features like radio bridges (e.g., between Abell 399–401), hinting at cosmic web shocks.

The Murchison Widefield Array has provided important southern hemisphere coverage and spectral confirmation. Its wideband (70–300 MHz) observations show that relics follow consistent power-law spectra down to low frequencies (with mean $\alpha \approx 1.2$), reinforcing aging synchrotron models. It has also reclassified suspected relics as AGN remnants and revealed new examples like a steep-spectrum source in Abell 1127 and early signs of relics in SPT-CL J2032–5627. The MWA's synergy with higher-frequency data (e.g., VLA) enables reconstruction of full spectral energy distributions (SEDs) that tightly constrain electron aging.

SKA precursors ASKAP and MeerKAT have uncovered several new relics in underexplored southern clusters. ASKAP's EMU (Evolutionary Map of the Universe) survey revealed prominent relics in SPT-CL J2023–5535 and a double relic in SPT-CL J2032–5627, both consistent with major mergers. Though X-ray confirmation is lacking in some cases, the radio morphology and spectral indices ($\alpha \sim 1.2$ to 1.3) align with known relic properties. MeerKAT has contributed with high-sensitivity follow-ups, including detection of a double relic in PSZ2 G277+12. These instruments are helping to fill gaps in the relic census and will enable statistical studies of relic-cluster correlations.

The VLA remains essential for high-resolution, high-frequency studies. It has been used to image the Sausage, Toothbrush, and other relics at 1–10 GHz, revealing filamentary substructures, spectral index gradients, and sharp edges tracing shock fronts. Polarization studies show relics are among the most polarized extragalactic sources, with fractional polarization reaching up to 70% at high frequencies (up to a few GHz). These measurements confirm the presence of coherent magnetic fields aligned along the shock, consistent with compression. The VLA has also revealed direct connections between relics and AGN tails (e.g., in Abell 3411–3412), supporting the re-acceleration of fossil plasma as a seed population. Overall, VLA observations have refined spectral modeling, validated shock-relic

associations, and helped shape hybrid acceleration models.

Cluster radio shocks appear to be less common than radio halos or mini-halos, with an occurrence rate of about $5\% \pm 3\%$ [67]. The detectability of these sources is likely influenced by the orientation of the merger axis. Some giant cluster radio shocks—such as those in the Sausage and Toothbrush clusters—are believed to originate from major mergers with subcluster mass ratios $\lesssim 3$ [91, 62, 63]. However, systems with larger mass ratios (e.g., $\gtrsim 5$), such as ZwCl 0008.8+5215 and PLCK G287.0+32.9, also host double or multiple radio shocks [51, 45].

The most powerful known cluster radio shock is found in MACS J0717.5+3745 [42, 128]. The most distant radio shocks have been observed in the "El Gordo" cluster at $z = 0.87$ [83, 76, 16].

A particular class of relics is represented by double radio shocks. In idealized binary merger scenarios, "equatorial" shocks initially form and propagate outward in the plane perpendicular to the merger axis (see Figure 6). After the dark matter cores pass each other, two "merger" shocks are launched in opposite directions along the merger axis. This mechanism can explain the formation of double radio shocks observed in merging clusters [133, 134, 84]. Currently, about a dozen well-defined double radio shock systems are known (see Table 1). The first such system was discovered in Abell 3667 [113], with subsequent confirmation through X-ray shock detection [47]. Other notable examples include Abell 3376 [4], CIZA J2242.8+5301 [129], ZwCl 0008.8+5215 [134], MACS J1752.0+4440 [130, 13], PSZ1 G108.18–11.53 [31], and Abell 1240 [72, 12].
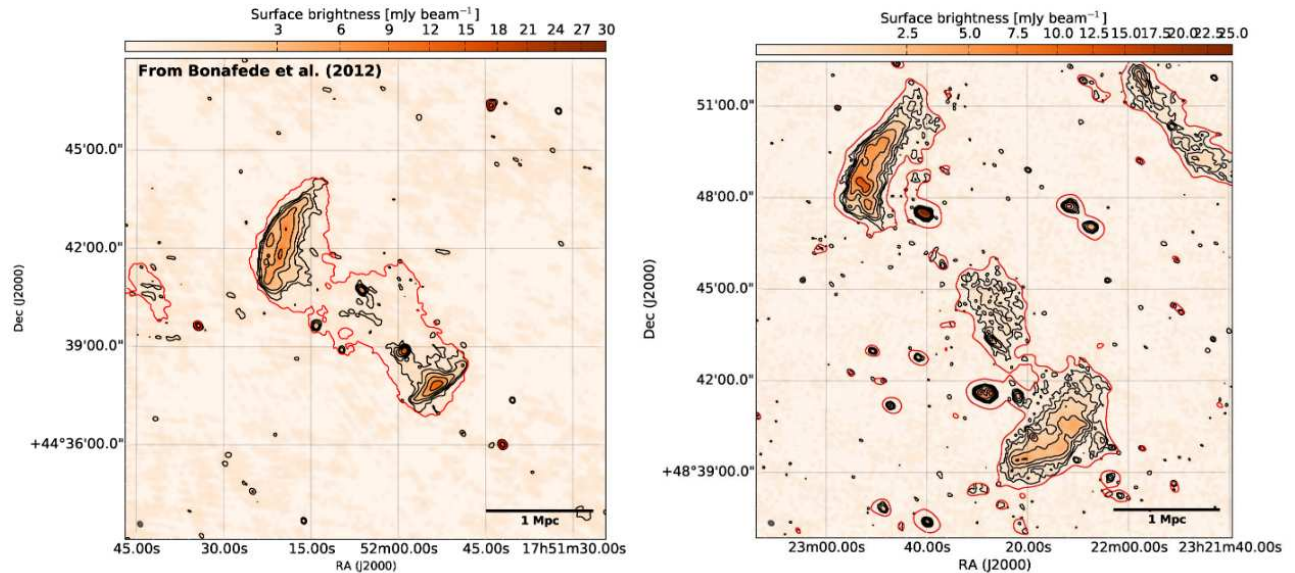
Figure 6. Example of double radio relic systems. Comparison between the image at 323 MHz of MACSJ1752.0+4440 and of PSZ1 G108.18-11.53 (right), from Bonafede et al. [13] and de Gasperin et al. [31] respectively.

Name	z	M_{500c} $[10^{14}M_\odot]$	Pos.	$P_{1.4\,\mathrm{GHz}}$ $[10^{24}\,\mathrm{W\,Hz^{-1}}]$	LLS [Mpc]	Ref.
Abell 1656[I]	0.023	7.17		0.31	0.85	1
PSZ2 G146*[I]	0.03	1.8		0.02	0.37	2
Abell 168	0.045	1.24		0.14	0.80	3
Abell 3376	0.046	3.64	E	0.54	1.60	4
			W	0.40	0.96	4
Abell 3667	0.056	5.77	NW	15.1	2.30	5
			SE	2.6	1.6	5
Abell 3266[I]	0.059	6.64		0.24	0.58	6
CIZA J0649	0.064	3.3		1.2	0.80	7,8
CIG 0217+70	0.066	10.6	SE	0.99	3.5	9
			SE	1.27	5.10	9
			W	1.85	2.3	9
RXC J1053	0.070	1.1		0.2	0.6	7,8
Abell 1904*	0.070	1.83	N	0.32	0.23	10
			S	0.005	0.17	10
			NE	0.01	0.90	10
Abell 2061	0.078	3.59		0.45	0.68	7
Abell 2255	0.081	5.38		0.18	0.70	7
Abell 2249	0.084	3.73		0.41	1.3	11
Abell 2018*	0.088	2.51		0.04	1.1	10
Abell 2108*	0.092	1.80		0.01	0.20	12
Abell 3365	0.093	1.70	E	0.74	0.55	13,14
			W	0.09	0.29	13,14
Abell 523	0.100	1.70		1.70	1.35	7,8
ZwCl0008	0.103	3.30	E	1.54	1.41	13
			W	0.30	0.30	13
Abell 1925*	0.105	2.81	N	0.12	1.71	15
			S	0.08	1.09	15
Abell 2034	0.113	5.85		0.89	0.22	7
Abell 3186	0.127	6.44		2.50	2.00	16
WHL J1013*	0.146	2.49		0.01	0.31	17
PSZ2 G278	0.158	3.6	N	1	0.66	18
			S	0.70	1.64	18
Abell 1240	0.159	3.71	S	0.73	1.28	13
			N	0.43	0.87	13
Abell 3411	0.169	6.59		5.00	1.90	19
PSZ2 G109*	0.173	3.26		0.50	1.17	15
PSZRX G182*	0.175	2.40		0.30	1.00	17
Abell 2345	0.177	5.92	W	2.85	0.83	13
			E	2.66	1.57	13
Abell 1612	0.179	4.42		7.90	0.78	7
Abell 1697*,I	0.183	4.34		0.38	0.70	10
WHL J1721*	0.184	2.29		0.08	0.60	17
Abell 1889*	0.185	2.58	NW	0.50	1.65	17
			SE	0.40	1.65	17
PSZ2 G145*	0.190	4.25		0.04	0.77	15
CIZAJ2243	0.192	16.2	N	15.0	2.00	13,20
			S	1.95	1.65	13,20
Abell 115	0.197	7.65		2.70	2.50	21
Abell 2163	0.203	16.1		2.09	0.48	1
1RXS J0603	0.220	10.76	N	65.0	1.90	22
			E	2.50	1.10	22
			S	1.40	0.25	22
PLCK G201	0.220	2.70	E	3.90	1.19	16
PSZ G087*	0.222	3.83		0.03	1.00	15
SPT2023-5535I	0.230	6.49		3.40	0.50	23,24
Abell 746	0.232	5.34	W	4.25	1.80	25
			N	0.18	0.38	25
			E	0.19	0.95	25
PSZ2 G181*	0.240	4.23	S	0.48	1.66	15
			N	0.20	1.39	15
RXCJ1314	0.244	6.15	W	3.90	0.91	13
			E	1.68	1.13	13
MCXC J0929*	0.247	3.90	SW	0.30	0.30	17
			SE	0.2	0.35	17
Abell 521	0.247	7.26	SE	3.09	0.93	26
ZwCl2341	0.270	5.15	S	4.09	1.23	13
			S	0.005	0.17	10
Abell 1758S*	0.280	8.22		0.22	0.54	15
SPT2023-5627	0.284	5.74	SE	1.40	0.73	27
			NW	0.91	0.86	27
Abell 959*	0.289	5.08		0.22	0.81	15
1E 0657-55.8	0.296	11.4	E	43.5	0.99	28
			NNW	0.60	0.90	28
Abell 781	0.295	6.13		4.47	0.44	1
PPSZ G198*	0.299	5.50		0.51	1.49	15
PSZ1G097	0.300	4.70	S	3.12	1.42	13
			N	1.52	0.88	13
Abell 1300	0.3072	8.97		5.75	0.70	1
Abell 2744	0.308	9.84	NE	4.37	1.50	29
			SE	0.96	1.15	29
MACS J0258	0.322			0.39		16
Abell 1943*	0.336	8.14	0.03	0.37		17
PSZ2 G121*	0.344	5.69		0.21	0.54	15
PSZ2 G096*	0.350	5.39		0.60	1.48	15
PSZRX G095*	0.362	3.34		0.80	1.30	17
PSZ2 G092*	0.362	6.31		0.32	1.53	15
MACS J1752	0.366	6.96	NE	33.1	1.19	13
			SW	15.0	0.69	13
PSZ2 G114*	0.371	7.58	N	3.40	1.17	15
			S	0.83	1.48	15
ZwCl1447	0.376	3.40	SW	1.11	1.20	30
			NE	0.51	0.30	30
PSZ2 G187*	0.378	6.84		0.27	0.72	15
PSZ1 G287	0.390	13.89	NW	23.3	2.48	13
		9.71	SE		1.58	13
WHL J1305*	0.396	3.29		0.06	1.40	17
PSZ2 G117*	0.396	7.61		0.32	0.56	15
MCXC J0943*	0.406	4.75		0.40	0.53	17
PSZ2 G206*	0.447	7.39	S	0.25	0.66	15
			N	0.18	0.66	15
PSZ2 G191*	0.488	5.55		2.49	0.57	15
MACS J1149	0.544	8.55	W	6.03	0.70	13
			E	5.33	0.78	13
PSZ2 G069	0.762	5.69		3.75	1.49	15
PSZ2 G092	0.822	7.40		5.25	0.90	31
ACT J0102	0.870	8.80	NW	29.6	0.93	13
			SE	4.48	0.46	13

Table 1. Properties of the observed radio relics from Lee et al. [75].

Column 1: cluster name. Column 2: cluster redshift. Column 3: core mass. Column 4: position in the cluster. Column 5: radio luminosity at 1.4 GHz. Column 6: projected size. Column 7: papers of reference. Radio relics only detected at a low frequency are annotated with *. The inverted radio relics are marked with [I]. References. (1) Feretti et al. (2012); (2) Botteon et al. (2021); (3) Dwarakanath et al. (2018); (4) Chibueze et al. (2023); (5) de Gasperin et al. (2022); (6) Riseley et al. (2022); (7) van Weeren et al. (2011b); (8) Pratt et al. (2009); (9) Hoang et al. (2021); (10) van Weeren et al. (2021); (11) Locatelli et al. (2020); (12) Schellenberger et al. (2022); (13) de Gasperin et al. (2014); (14) Lovisari & Reiprich (2019); (15) Botteon et al. (2022); (16) Knowles et al. (2022); (17) Hoang et al. (2022); (18) Koribalski et al. (2023); (19) van Weeren et al. (2013); (20) Jee et al. (2015); (21) Govoni et al. (2001a); (22) van Weeren et al. (2016); (23) HyeongHan et al. (2020); (24) Bulbul et al. (2019); (25) Rajpurohit et al. (2024); (26) Giacintucci et al. (2006); (27) Duchesne et al. (2021); (28) Sikhosana et al. (2023); (29) Pearce et al. (2017); (30) Lee et al. (2022); (31) Di Gennaro et al. (2023).

3.6   MACS J1752+4440

The object of this thesis, MACS J1752.0+4440 (z=0.366), has been the subject of a series of multi-wavelength observations spanning over two decades, revealing it to be a textbook example of a double radio relic galaxy cluster undergoing a major merger. Double shocks are a particularly interesting class of radio relics, since they offer good constraints on the merger scenario (as discussed in Section 3.5). Situated at right ascension RA = $17^\mathrm{h}52^\mathrm{m}44^\mathrm{s}$ and declination DEC = $+44°40'00''$ in the J2000 coordinate system, the relic system is composed of two large elongated convex radio shocks that are found diametrically opposite each other with respect to the cluster center (see Figure 6), oriented perpendicular to the merger axis.

This cluster was discovered in the Massive Cluster Survey (Ebeling et al. [37]). A candidate for a z > 0.3 double relic system in MACS J1752.0+4440 (hereafter MACS1752) was reported by Edge et al. [38] in 2003, with two radio sources found on opposite sides of the cluster center in NRAO VLA Sky Survey (NVSS,Condon et al. [28]) and Westerbork Northern Sky Survey (WENSS, [111]) images. First X-ray measurements are from the ROSAT All-Sky Survey Bright Source Catalog Voges et al. [138].
In 2011, observations of MACS J1752+4440 were conducted with the Westerbork Synthesis Radio Telescope (WSRT) at multiple frequencies: 25 cm, 21 cm, 18 cm, and 13 cm, in S and L bands. These observations, published by van Weeren et al. [130] (2012), confirmed the presence of two large, arc-shaped radio relics located symmetrically with respect to the cluster center, as well as a centrally located radio halo spanning 1.65 Mpc. Integrated flux density measurements for the northeast (NE) and southwest (SW) relics at 1.714 GHz were reported as follows:

- NE relic: 55.1 ± 2.9 mJy

- SW relic: 25.7 ± 1.4 mJy

The radio study measured the largest linear size (LLS) of the NE relic to be 1.35 Mpc and that of the SW relic to be 0.86 Mpc. Integrated spectral indices of the relics were reported as 1.16 ± 0.03 in the NE and 1.10 ± 0.05 in the SW.
Bonafede et al. [13] (2012) confirmed the presence of the two radio relics and radio halo with the Giant Metrewave Radio Telescope (GMRT) observations. Setting the midpoint between the X-ray brightness peaks as the cluster center, they estimated the projected distance to the relics to be 1.13 and 0.91 Mpc to the NE and SW, respectively. By combining the GMRT and WSRT observations, Bonafede et al. [13] measured integrated spectral indices of 1.21 ± 0.06 and 1.12 ± 0.07 for the NE and SW relics, respectively. The integrated flux densities at 323 MHz were:

- NE relic: 410 ± 33 mJy

- SW relic: 163 ± 13 mJy

Spectral index mapping across the relics suggested diffusive shock acceleration as the primary mechanism, with spectral steepening observed toward the cluster center.
The NE relic displayed a clear spectral steepening toward the cluster center—a hallmark of outgoing merger shocks. Additionally, high levels of polarization ($\sim 40\%$) were detected at the edges of both relics. From the injection spectral indices ($\alpha_\mathrm{inj} \sim 0.6$ for the NE relic and ~ 0.8 for the SW relic), Mach numbers were inferred to be $\mathcal{M}_\mathrm{NE} \sim 4.6$ and $\mathcal{M}_\mathrm{SW} \sim 2.8$,

respectively.

The Sunyaev–Zel'dovich effect mass of the cluster is estimated to be $M_{500} = (6.7^{+0.4}_{-0.5}) \times 10^{14}$ $M_\odot$ from the Planck Collaboration [102]. MACS1752 has also been the subject of numerical simulations aimed at investigating the efficiency of electron and proton acceleration in merger shocks, as well as to constrain the efficiency of cosmic-ray acceleration [136].

In 2010, MACS1752 was observed with the *XMM-Newton* X-ray observatory (PI: S. Allen; ObsID: 0650383401) for a total of 13 ks. The X-ray data revealed a disturbed intracluster medium, characterized by an inverted-S morphology indicative of past merging activity and a nearly head-on collision. Subsequent analysis by Finner et al. [46] in 2021 identified potential cold fronts in the ICM, located near—but not coincident with—the radio relics. The X-ray tail that lags behind the NE subcluster is a good indicator of the path that the NE subcluster followed and suggests a collision with a nonzero impact parameter. Given the equality of the subcluster masses, they expect the SW subcluster to have followed a similarly shaped path in the opposite direction. Evidence for the SW subcluster path may be present in the X-ray tail that extends from the SW subcluster, but it blends in with the central substructure.

Specifically, an ICM tail appears to have been stripped from the northeast subcluster core, extending about 0.5 Mpc toward the barycenter of the system. This tail suggests a powerful ram pressure force and a low impact parameter for the collision. An extension of the gas from the southwest (SW) subcluster toward the center of the cluster may also be caused by ram pressure, although it coincides with a central weak-lensing mass detection and X-ray peak.

MACS1752 was targeted by deep optical imaging campaigns to enable weak-lensing mass reconstructions. Subaru Suprime-Cam observations were performed on three occasions (July 2013, February 2014, and September 2015) in the g, r, and i bands. These were complemented by *Hubble Space Telescope* (HST) Advanced Camera for Surveys (ACS) observations between 2011 and 2014, covering both NE and SW subcluster regions with F435W, F606W, and F814W filters, with results displayed by Finner et al. [46].

These datasets enabled a high-precision weak-lensing analysis, resulting in the identification of a near 1:1 mass merger with subcluster masses:

- NE component: $5.6^{+1.6}_{-1.8} \times 10^{14}$ $M_\odot$

- SW component: $5.6^{+2.1}_{-1.4} \times 10^{14}$ $M_\odot$

The total system mass was estimated at $1.47^{+0.33}_{-0.38} \times 10^{15}$ $M_\odot$, consistent with Planck SZ-derived masses [102].

Finner et al. [46] concluded that MACS J1752 is in the outgoing phase, with time-since-collision estimates of 0.9 ± 0.2 Gyr, 0.2–0.5 Gyr, and 0.21–0.35 Gyr from the different methods implemented. These methods yield collision velocity estimates of 2233^{+143}_{-130} km s^{-1}, 2444–3034 km s^{-1}, and 3360–5520 km s^{-1}, respectively.

Defining the merger axis from the X-ray distribution, they have postulated that the SW radio relic is rotated from its expected position and may be a signature of particle reacceleration in action. Further radio and X-ray observations are required to make stronger conclusions.

The spectroscopic redshift study of Golovich et al. [52] found that a two-halo model is preferred and that the two subclusters have similar redshifts—evidence that supports MACS1752

as a plane-of-the-sky merger.

Figure 7 presents the binary merger between the NE and SW subclusters in a multi-frequency representation from past observations and publications.
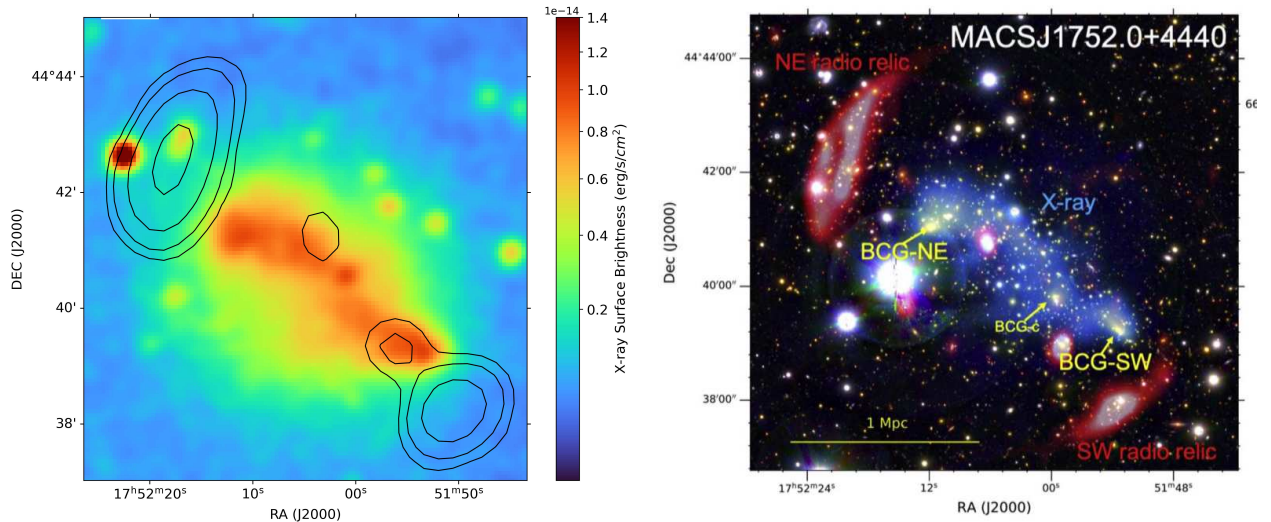
Figure 7. *Left:* XMM image of MACS J1752+4440, with NVSS contours at 3,5,10,20 σ, with σ=0.6 mJy. *Right:* Subaru gri color image of MACS1752 with 18 cm WSRT radio emission (red) from [130] and 0.5–7 keV XMM-Newton X-ray emission (blue), from Finner et al. [46].

Throughout this work we assume a flat ΛCDM cosmology with $H_0 = 70$ km s^{-1} Mpc^{-1}, $\Omega_\mathrm{m} = 0.3$, and $\Omega_\Lambda = 0.7$.

At the redshift of 0.366, 1 arcminute corresponds then to 305 kpc.

4

The principles of Radio Astronomy

This chapter outlines radio astronomy basic concepts: Section 4.1 reports common quantities used in this field, Section 4.2 delineates the functioning principles of single dish radio telescopes, as it is done for interferometers in Section 4.3. In sections 4.2.1 and 4.3.1, the instruments from which data used in this thesis were obtained are briefly described.

4.1 Radiation Fundamentals

Electromagnetic radiation in the radio window is a wave phenomenon, but when the scale of the system involved is much larger than the wavelength, we can consider the radiation to travel in straight lines as rays [139]. The infinitesimal power dP intercepted by an infinitesimal surface $d\sigma$ is then

$$dP = I_\nu \cos\theta \, d\Omega \, d\sigma \, d\nu, \qquad (4.1)$$

where

- dP = infinitesimal power, in Watts,

- $d\sigma$ = infinitesimal area of surface, in m^2,

- $d\nu$ = infinitesimal bandwidth, in Hz,

- θ = angle between the normal to $d\sigma$ and the direction to $d\Omega$,

- I_ν = brightness or specific intensity, in W m^{-2} Hz^{-1} sr^{-1}.

Equation (4.1) should be considered to be the definition of the brightness I_ν.
The total flux density of a source is obtained by integrating equation (4.1) over the total solid angle Ω_s subtended by the source:

$$S_\nu = \int_{\Omega_s} I_\nu \cos\theta \, d\Omega, \qquad (4.2)$$

and this is measured in units of W m^{-2} Hz^{-1}. Since the flux density of radio sources is usually very small, a radio astronomical flux density unit, the *Jansky* (Jy), has been introduced:

$$1 \text{ Jy} = 10^{-26} \text{ W m}^{-2} \text{ Hz}^{-1} = 10^{-23} \text{ erg s}^{-1} \text{ cm}^{-2} \text{ Hz}^{-1}. \qquad (4.3)$$

The brightness of an extended source is a quantity similar to the surface brightness in optical astronomy: it is independent of the distance to the source, as long as the effects of diffraction and extinction can be neglected (see [139] for more details).
Let's consider a sphere with uniform brightness I_ν and radius R. The total flux density received by an observer at the distance r then is

$$S_\nu = \int_{\Omega_s} I_\nu \cos\theta \, d\Omega = I_\nu \int_0^{2\pi} \int_0^{\theta_c} \sin\theta \cos\theta \, d\theta \, d\phi,$$

where

$$\sin \theta_c = \frac{R}{r}$$

defines the angle θ_c that the radius of the sphere subtends at r. We obtain

$$S_\nu = \pi I_\nu \sin^2 \theta_c = I_\nu \frac{\pi R^2}{r^2} = I_\nu \, \Delta\Omega, \tag{4.4}$$

where $\Delta\Omega$ is defined as the solid angle subtended by the object at a distance r.

Another useful quantity related to the brightness is the radiation energy density u_ν in units of erg cm^{-3}. From dimensional analysis, u_ν is intensity divided by speed. Since radiation propagates at the speed of light c, we have for the spectral energy density per solid angle

$$u_\nu(\Omega) = \frac{1}{c} I_\nu. \tag{4.5}$$

If integrated over the whole sphere (4π steradians), equation (4.5) yields the total spectral energy density:

$$u_\nu = \int u_\nu(\Omega) \, d\Omega = \frac{1}{c} \int I_\nu \, d\Omega.$$

The specific intensity I_ν will change only if radiation is absorbed or emitted, and this change in I_ν is described by the *equation of transfer*. For a change in I_ν along the line of sight, a loss term dI_ν^- and a gain term dI_ν^+ are introduced:

$$dI_\nu^- = -\kappa_\nu I_\nu \, ds, \tag{4.6}$$

$$dI_\nu^+ = \epsilon_\nu \, ds, \tag{4.7}$$

so that the change of intensity in a slab of material of thickness ds will be:

$$[I_\nu(s + ds) - I_\nu(s)] \, d\sigma \, d\Omega \, d\nu = [-\kappa_\nu I_\nu + \epsilon_\nu] \, d\sigma \, d\Omega \, d\nu \, ds.$$

This results in the *equation of radiative transfer*:

$$\frac{dI_\nu}{ds} = -\kappa_\nu I_\nu + \epsilon_\nu. \tag{4.8}$$

Fundamental to define is the brightness temperature, that is used in radio astronomy to measure the brightness of an extended source. To define this temperature, one should start from the spectral distribution of the radiation of a black body in thermodynamic equilibrium, given by the *Planck law*:

$$B_\nu(T) = \frac{2h\nu^3}{c^2} \cdot \frac{1}{e^{h\nu/kT} - 1}, \tag{4.9}$$

where $B_\nu(T)$ is the spectral radiance (specific intensity per unit frequency) in W m^{-2} Hz^{-1} sr^{-1}, h is Planck's constant, ν is the frequency, k is Boltzmann's constant, T is the absolute temperature, c is the speed of light.

Specifically, when $h\nu \ll kT$, we enter the *Rayleigh-Jeans regime*. Expanding the exponential in the Planck law using a first-order Taylor approximation,

$$e^{h\nu/kT} \approx 1 + \frac{h\nu}{kT} + \dots, \tag{4.10}$$

we obtain the *Rayleigh-Jeans law*:

$$B_{\mathrm{RJ}}(\nu, T) = \frac{2\nu^2 kT}{c^2}. \tag{4.11}$$

The brightness temperature is defined as the temperature that would result in the given brightness if inserted into the Rayleigh-Jeans law. It is called the *brightness temperature*, defined by:

$$T_b = \frac{c^2}{2k\nu^2} I_\nu, \tag{4.12}$$

or equivalently,

$$I_\nu = \frac{2k\nu^2}{c^2} T_b. \tag{4.13}$$

Combining equation (4.13) with the flux density expression in equation 4.4, we find:

$$S_\nu = \frac{2k\nu^2}{c^2} T_b \, \Delta\Omega, \tag{4.14}$$

where $\Delta\Omega$ is the solid angle subtended by the source.

That is, with a measurement of the flux density S_ν in Janskys, and the source size (i.e., the solid angle $\Delta\Omega$), the brightness temperature T_b of the source can be determined using equation (4.14).

4.2   Single Dish Radio Telescopes

A single-dish radio telescope consists of a parabolic reflector that collects incoming radio waves and focuses them onto a receiver at the focal point.

A radio telescope with effective area A_e receives power P_{rec} per unit frequency from an unpolarized source:

$$P_{\mathrm{rec}} = \frac{1}{2} I_\nu A_e \delta\Omega. \tag{4.15}$$

The coefficient $\frac{1}{2}$ in equation 4.15 arises because a receiver is generally sensitive to only one mode of polarization [110].

Antennas bring incident electromagnetic (EM) power to a focus after reflecting it off a primary surface. The antenna response (i.e., its relative sensitivity) is a summation of all EM power brought to the focus. This response depends on the angle from the on-axis pointing direction due to diffraction (i.e., self-interference).

Since sources are very distant, the EM power arrives as plane-parallel wavefronts. For EM radiation arriving on-axis, the parabolic shape ensures that the path length to the focus is the same for all rays, allowing constructive summation of power on-axis.

However, for EM power arriving from an off-axis direction, the power does not add as constructively. The projected aperture is also smaller than the true diameter, reducing the collected power. At an off-axis angle of $\theta = \lambda/D$, the path difference across the aperture equals one wavelength, resulting in destructive interference at that angle.

Figure 8 illustrates a one-dimensional antenna power response for a 12-m diameter parabolic antenna illuminated uniformly by emission at $\lambda \approx 0.85\,\mathrm{mm}$ (350 GHz). The central Gaussian-like feature, called the *primary beam* or *antenna beam*, has a Half Power Beam Width

(HPBW) given by:

$$\text{HPBW}_{\text{Primary Beam}} = 1.02 \times \frac{\lambda}{D}. \tag{4.16}$$

HPBW is also referred to as Full Width at Half Power (FWHP) and corresponds to the Full Width at Half Maximum (FWHM) in one dimension for a Gaussian. For a 12-m antenna at $\lambda = 0.85\,\text{mm}$, equation 4.16 yields a FWHM of $14.9''$.

The antenna power response shows sidelobes and nulls at larger angles due to interference. The first sidelobes have a relative power response of only 1.74% of the main beam. However, bright off-axis sources can still contribute significantly. The angular distance between the first nulls is called the Full Width Between Nulls (FWBN), given by:

$$\text{FWBN}_{\text{Primary Beam}} = 2.44 \times \frac{\lambda}{D}. \tag{4.17}$$
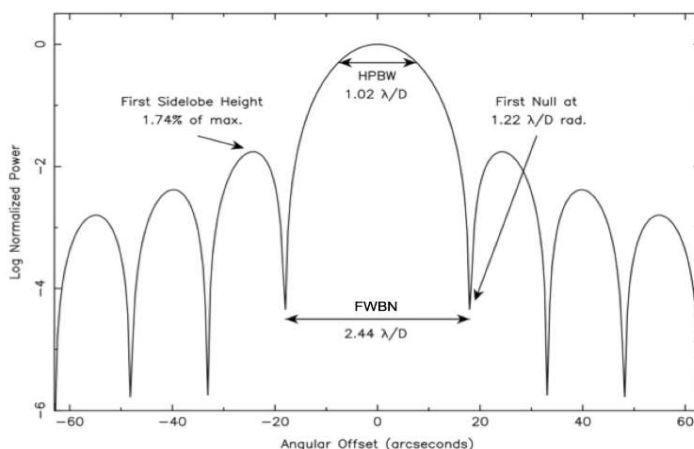
Figure 8. From [110]. Normalized one-dimensional (1D) antenna power response for a 12-meter antenna uniformly illuminated at 350 GHz. The power is plotted in logarithmic units to emphasize the sidelobes. The HPBW of the primary beam is approximately $1.02\,\lambda/D$, and the FWBN is approximately $2.44\,\lambda/D$. The angle of the first null, i.e., the resolution, is $0.5 \times \text{FWBN} \approx 1.22\,\lambda/D$.

Half the FWBN, approximately $1.22\lambda/D$, is referred to as the Rayleigh resolution of the antenna.

Real antennas are affected by secondary illumination, diffraction from support structures, and surface errors.

An alternative description of antenna response uses the voltage pattern $V(\theta)$, where:

$$P(\theta) \propto V^2(\theta).$$

In the far field (Fraunhofer regime), the voltage pattern is the Fourier transform of the field at the aperture. For an unobstructed circular aperture, the voltage response is:

$$V(\theta) = \frac{J_1(\theta)}{\theta},$$

where $J_1(\theta)$ is the Bessel function of the first kind. The power pattern is then:

$$P(\theta) \propto \left(\frac{J_1(\theta)}{\theta} \right)^2,$$

which defines the normalized antenna power response $P_N(\theta)$, also known as the Airy function.

Defining θ and ϕ as orthogonal directional sky coordinates, the directional brightness and antenna power response are represented as $I_\nu(\theta, \phi)$ and $P_N(\theta, \phi)$, respectively. The total received power at a given pointing is:

$$P_{\text{rec}} = \frac{A_e}{2} \int_{4\pi} I_\nu(\theta, \phi) P_N(\theta, \phi) \, d\Omega. \tag{4.18}$$

The solid angle of the antenna power pattern is defined by:

$$\Omega_A = \int_{4\pi} P_N(\theta, \phi) \, d\Omega. \tag{4.19}$$

4.2.1 The Sardinia Radio Telescope

The SRT [11, 103] is a 64-meter single-dish radio telescope. It is located in the Pranu Sanguni area of San Basilio, Sardinia, Italy, about 40 km north of Cagliari.

The SRT has a shaped Gregorian optical configuration with a 7.9 m diameter secondary mirror and supplementary beam- wave-guide (BWG) mirrors. Its state-of-the-art technology includes an active surface with 1008 panels, which allows observations at high frequencies (from 0.3 up to 115 GHz). There are three main focal points where receivers can be placed: primary focus, Gregorian focus, and Beam Wave Guide focus. In total, the telescope can accomodate up to 20 receivers. A number of additional receivers are currently being planned and built.

The telescope can be operated in single-dish or Very Long Baseline Interferometry (VLBI) mode for radio astronomy, geodynamical studies or space science. Its geographical location allows it to observe at declinations above -33 degrees.
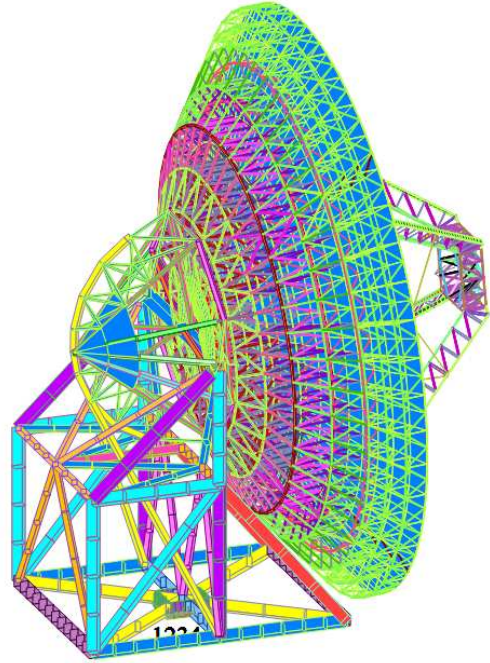
Figure 9. Model of the SRT antenna

The FWHM beam size, as a function of the frequency f, can be approximated by the following rule: FWHM(arcmin)=19.7/ f(GHz).

SRT receiver changes are quick, allowing for an efficient frequency agility. The selected receiver is set in its focal position within at most a few minutes.

The following cryogenically-cooled receivers are available at the Sardinia Radio Telescope (SRT) for both single-dish and VLBI observations:

- L/P Band (1.3–1.8 GHz + 305–410 MHz): A dual-frequency single-feed receiver at the primary focus, with the primary mirror configured parabolically. This allows simultaneous observations in both bands. The native polarization is linear but is converted

to circular using a hybrid converter.

The L-band (1.3–1.8 GHz) channel has system temperature $T_{\mathrm{sys}} \approx 20\,\mathrm{K}$, gain $\sim$ $0.52\,\mathrm{K/Jy}$, and beam size of ~ 12.5 arcminutes.

The P-band (305–410 MHz) channel features $T_{\mathrm{sys}} \approx 52\,\mathrm{K}$, gain $\sim 0.53\,\mathrm{K/Jy}$, beam size of ~ 55 arcminutes.

- C-low Band (4.2–5.6 GHz): A single-feed receiver installed at the Beam Wave Guide focus. It operates with a system temperature (T_{sys}) of approximately 25 K at 90° elevation, provides a beam size of about 4.2 arcminutes, and a maximum gain of 0.75 K/Jy. The polarization is circular.

- C-high Band (5.7–7.7 GHz): This is another single-feed, cryogenically-cooled receiver also located at the BWG focus. It offers a T_{sys} between 32–37 K, a beam size of 2.7 arcminutes, and a gain of 0.66 K/Jy. It supports circular polarization.

- K Band (18–26.5 GHz): A 7-feed, multi-beam receiver installed at the Gregorian focus. It operates with a T_{sys} of about 70 K, a beam size of 0.8 arcminutes, and a gain of 0.66 K/Jy. The polarization is circular. The receiver supports multi-beam observations (indicated by MB).

For the observations reported in this work, we employed the SArdinia Roach2-based Digital Architecture for Radio Astronomy (SARDARA [82]), one among the currently available digital backends.

4.3   Radio Interferometers

Observing at millimeter/radio wavelengths is essentially diffraction-limited, as the angular diameter of the Airy disk, the FWHM for a circular aperture of diameter D, is approximately $1.22\lambda/D$ [110]. Millimeter/radio wavelength (single-dish) observations have lower resolutions than optical wavelength observations because λ is much larger. Although the diameter D of millimeter/radio telescopes can be significantly larger than that of optical telescopes, the increase is generally insufficient to achieve comparable angular resolutions (e.g., $1''$ or better).

To achieve higher angular resolution, signals from separated antennas can be combined using interferometry. This technique, known as aperture synthesis, emulates the resolution of a much larger telescope. However, only certain angular scales corresponding to the projected separations of antenna pairs are sampled.

For a plane-parallel wavefront arriving on-axis, EM power across the antenna is summed in phase at the focus. Dividing the parabolic surface into N smaller contiguous elements, the received voltage $V(t)$ becomes:

$$V(t) = \sum_i \Delta V_i(t). \tag{4.20}$$

The power received by the antenna is proportional to the running time average of the square of the contributions from each element. Assuming illumination is the same for each element, the expression for received power in terms of the sum of time averages of the products of voltages from element pairs can be rewritten as:

$$\langle P \rangle \propto \left\langle \left(\sum_i \Delta V_i \right)^2 \right\rangle = \sum_i \sum_k \langle \Delta V_i \Delta V_k \rangle. \tag{3.9}$$

Next, this expression can further be rewritten in terms of the sums over element pairs that are the same and those that are not:

$$\langle P \rangle \propto \sum_i \langle \Delta V_i^2 \rangle + \sum_{i \neq k} \langle \Delta V_i \Delta V_k \rangle. \tag{3.10}$$

The first and second sets of terms in Equation (3.10) are called the auto-correlation and cross-correlation terms, respectively, since the voltages multiplied in each term are from either the same or different elements.

From Equation (3.10), any measurement with a large filled-aperture telescope can be understood as being a sum in which each term depends on contributions from only two of the N elements. As long as the contributions from each element arrive at the focus in phase, there is no need for the elements to be physically contiguous.

Generalizing, each cross-correlation term $\langle \Delta V_i \Delta V_k \rangle$ can be measured with two smaller, physically separated antennas (at locations i and k) by measuring the average product of their output voltages with a correlating, or multiplying, receiver. Moreover, if the source properties do not change, there is no need to measure all pairs at the same time. A given parabolic surface with N elements has $N(N-1)/2$ unique pairs, and these could be observed sequentially to "synthesize" a measurement by a large filled-aperture telescope.

Alternatively, numerous pairs of antennas (each considered an element) can be distributed across distances much larger than the size of any single telescope. The signals received by these antennas can be combined in phase to approximate the resolving power of a filled-aperture telescope.

This description only applies to the emission received on-axis from antenna pairs. Emission also arrives from other directions, leading to phase differences. To understand the power response from a pair of antennas, consider the ideal 1D situation of a two-antenna interferometer.

Figure 10 shows a schematic of a two-antenna interferometer separated by a distance b, called the *baseline*. This distance can be measured in units of the observing wavelength λ. In physical terms, $b = L/\lambda$, where L is the physical distance between antennas.

Both antennas observe a source at an angle θ from the meridian. The projected baseline toward the source is $u = b\cos\theta$. An on-axis wavefront reaches antenna 2 before antenna 1, with a path difference $b\sin\theta$, corresponding to a geometric delay:

$$\tau_g = \frac{b\sin\theta}{c}.$$

This delay can be compensated by introducing an artificial delay in the signal path of antenna 2 so the signals arrive in phase at the correlator.
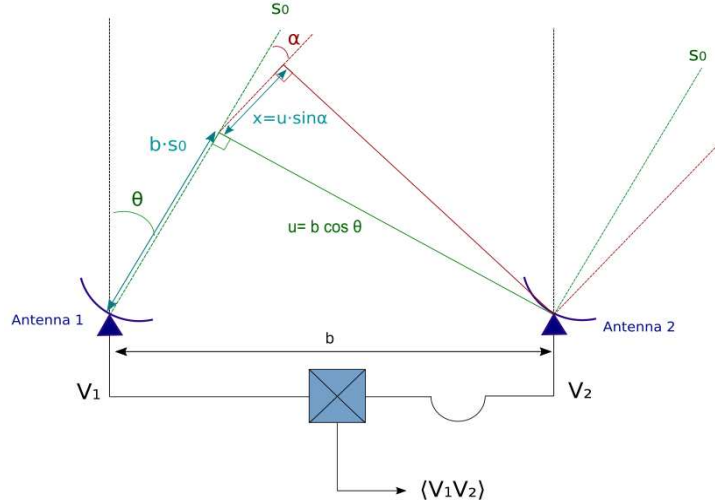
Figure 10. An ideal 1-D interferometer consisting of two antennas, 1 and 2, separated by a baseline b. Both antennas point towards the same direction in the sky, defined by an angle θ from the meridian. The projected distance between the two antennas in that direction is thus u = b cos θ. The two antennas are connected to a correlator where the voltages detected from each antenna are combined.

Now consider a small angle α from the axis. Define the direction cosine as $l = \sin \alpha$. At angle α, the signal reaching antenna 1 travels a longer path than the signal reaching antenna 2. The extra path length is:

$$x = u \sin \alpha = ul.$$

All distances are now considered in units of the wavelength. The resulting phase difference causes the voltage response at antenna 2 to be:

$$V_2 = V_1 e^{2\pi i(ul)}. \tag{3.11}$$

Extending to two dimensions, define an orthogonal direction β with $m = \sin \beta$. Let the baseline have components b_1 and b_2 in two dimensions, so:

$$u = b_1 \cos \theta, \quad v = b_2 \cos \phi,$$

where ϕ is the azimuthal angle of the source. The additional path length in the m direction is $y = vm$. Then, the 2D voltage response is:

$$V_2 = V_1 e^{2\pi i(ul+vm)}, \tag{3.12}$$

where u and v are the spatial frequencies, and l and m are the direction cosines relative to the phase center (usually defined at $l = m = 0$).

The correlator acts as a multiplying and time-averaging device for the incoming signals. Its output is:

$$\langle V_1 V_2 \rangle = \left\langle \left(\iint V_1(l,m) \, dl \, dm \right) \left(\iint V_2(l,m) \, dl \, dm \right) \right\rangle. \tag{3.13}$$

Under the assumption that signals emanating from different parts of the sky are incoherent (i.e., they have no similarities in phase), the time averages of the correlation of those signals will be zero. Thus, the product of the integrals in Equation (3.13) can be simplified to:

$$\langle V_1 V_2 \rangle = \iint \langle V_1(l,m)^2 \rangle e^{2\pi i(ul+vm)} \, dl \, dm. \tag{3.16}$$

As $V^2 \propto P$ (see Equation 3.9) and $P \propto I_\nu$ (see Equation 3.3), we have:

$$\langle V_1 V_2 \rangle \propto \iint I(l,m) e^{2\pi i(ul+vm)} \, dl \, dm, \tag{3.17}$$

where $I(l,m)$ is the intensity distribution on the sky. The correlator therefore measures a quantity known as the *complex visibility* $V(u,v)$, which is formally the Fourier transform of the intensity distribution on the sky:

$$V(u,v) = \iint I(l,m) e^{2\pi i(ul+vm)} \, dl \, dm = A e^{i\phi}. \tag{3.18}$$

Note that V is a complex number and can be described by an amplitude A and a phase ϕ. The amplitude and phase contain information about the source brightness and its location relative to the phase center, respectively, at spatial frequencies u and v.

The relationship between the sky brightness distribution and the complex visibility distribution is governed by the *van Cittert-Zernike theorem*, which forms the basis of aperture synthesis. Given that the complex visibility is the Fourier transform of the sky brightness distribution in the image plane, it follows that the sky brightness distribution is the inverse Fourier transform of the visibility distribution:

$$I(l,m) = \iint V(u,v) e^{-2\pi i(ul+vm)} \, du \, dv. \tag{3.20}$$

Here, the functions $A(l,m)$ and $1/\sqrt{1-l^2-m^2}$ are omitted, as they are typically close to unity.

By measuring the distribution of complex visibilities in the (u,v) plane, the sky brightness distribution can be recovered. In essence, an image is the inverse Fourier transform of the visibilities, where each visibility contains amplitude and phase information corresponding to brightness and spatial structure on a specific angular scale. The image and its Fourier transform are conjugate representations of the same data.

Two antennas separated by a distance b can interfere signals to sample the sky brightness distribution at an angular scale inversely proportional to the projection of that distance onto the sky. The response of the interferometer is sinusoidal and referred to as a *fringe*, with spacing on the sky (in the 1D case):

$$\text{Fringe Spacing} = \frac{1}{u} = \frac{1}{b\cos\theta} = \frac{\lambda}{L\cos\theta}. \tag{3.21}$$

This interference pattern modifies the angular response of the antennas. Antennas closer together sample larger angular scales, while more distant antennas sample smaller scales. Since baseline length b is measured in wavelengths, changing the wavelength of observation also changes the spatial scale being sampled.

These ideas extend naturally to two dimensions. Each antenna pair samples a single point in the (u,v) plane. Because visibilities are samples of a Hermitian function, each measurement gives data at (u,v) and $(-u,-v)$. To reconstruct the true brightness distribution, full coverage of the (u,v) plane is desired.

Coverage can be improved in three main ways:

1. Use multiple antennas in an array, with different pairwise separations to avoid redundancy. An array of N antennas yields $N(N-1)/2$ independent baselines.

2. Use Earth's rotation to change the projected baseline orientations over time as the source moves across the sky (known as *Earth rotation synthesis*).

3. Reconfigure the array layout to sample different regions of the (u, v) plane.

Assuming the source is stable, combining these methods allows us to recover of the brightness distribution by filling in the (u, v) plane adequately. This yields an image that closely approximates the true sky.

It is, however, impossible in practice to sample completely the (u, v) plane and obtain all visibilities. The incomplete (u, v) plane sampling effectively provides a fundamental limit to the level of detail discernible in the sky brightness distribution; i.e., down to a minimum scale defined as the resolution. In addition, incomplete sampling results in spatial filtering of the true sky brightness distribution; i.e., the resulting images do not contain information on angular scales unobserved by the interferometer. In particular, the lack of coverage at the shortest baselines (i.e., lower than those sampled by the smallest baselines) results in an intrinsic lack of sensitivity to large-scale emission.

The resolution of any interferometric image depends on the distribution of visibilities sampled. Assuming a finite number of M visibilities has been obtained, the (u, v) plane has been sampled at $2M$ discrete points. The sampling distribution can then be characterized as an ensemble of $2M$ (Dirac) delta functions:

$$B(u, v) = \sum_{k=1}^{2M} \delta(u - u_k, v - v_k). \tag{3.23}$$

Given the sampling function $B(u, v)$, we can calculate the dirty image $I^D(l, m)$:

$$I^D(l, m) = \iint V(u, v) B(u, v) e^{-2\pi i(ul + vm)} \, du \, dv. \tag{3.24}$$

The inverse Fourier transform of this ensemble of visibilities can be written as:

$$I^D(l, m) = \mathcal{F}^{-1} \{ B(u, v) V(u, v) \}. \tag{3.25}$$

Following the convolution theorem, the Fourier transform of a convolution of two functions is the product of the Fourier transforms of those functions. Hence, Equation 3.24 can be rewritten as:

$$I^D(l, m) = b(l, m) * I(l, m) A(l, m), \tag{3.26}$$

where $b(l, m) = \mathcal{F}^{-1} \{ B(u, v) \}$ is the point spread function, usually referred to as the dirty beam.

The image obtained is the convolution of the true sky brightness distribution (modified by the antenna power response $A(l, m)$) with the point spread function $b(l, m)$. It is important to distinguish this synthesized beam from the single-dish response function $A(l, m)$, which in the interferometric context is referred to as the primary beam.

Figure 11 shows a scheme of the relations between the different quantities to take into account when imaging interferometric data.

The image resulting from the Fourier transform of a finite number of visibilities, $I^D(l, m)$, is called the dirty image. The measure of how similar an image is to the true sky distribution

is referred to as image fidelity. Image fidelity depends on the specifics of the (u, v) coverage sampled by the interferometer. Since the number of samples is necessarily finite and discrete, there are invariably gaps in any practical sampling of the (u, v) plane. These gaps mean that no information is obtained about the true sky brightness distribution at those specific angular scales. Visibilities at unobserved locations can theoretically take any value, but in practice, it is typically assumed that $V(u, v) = 0$ at unsampled locations.
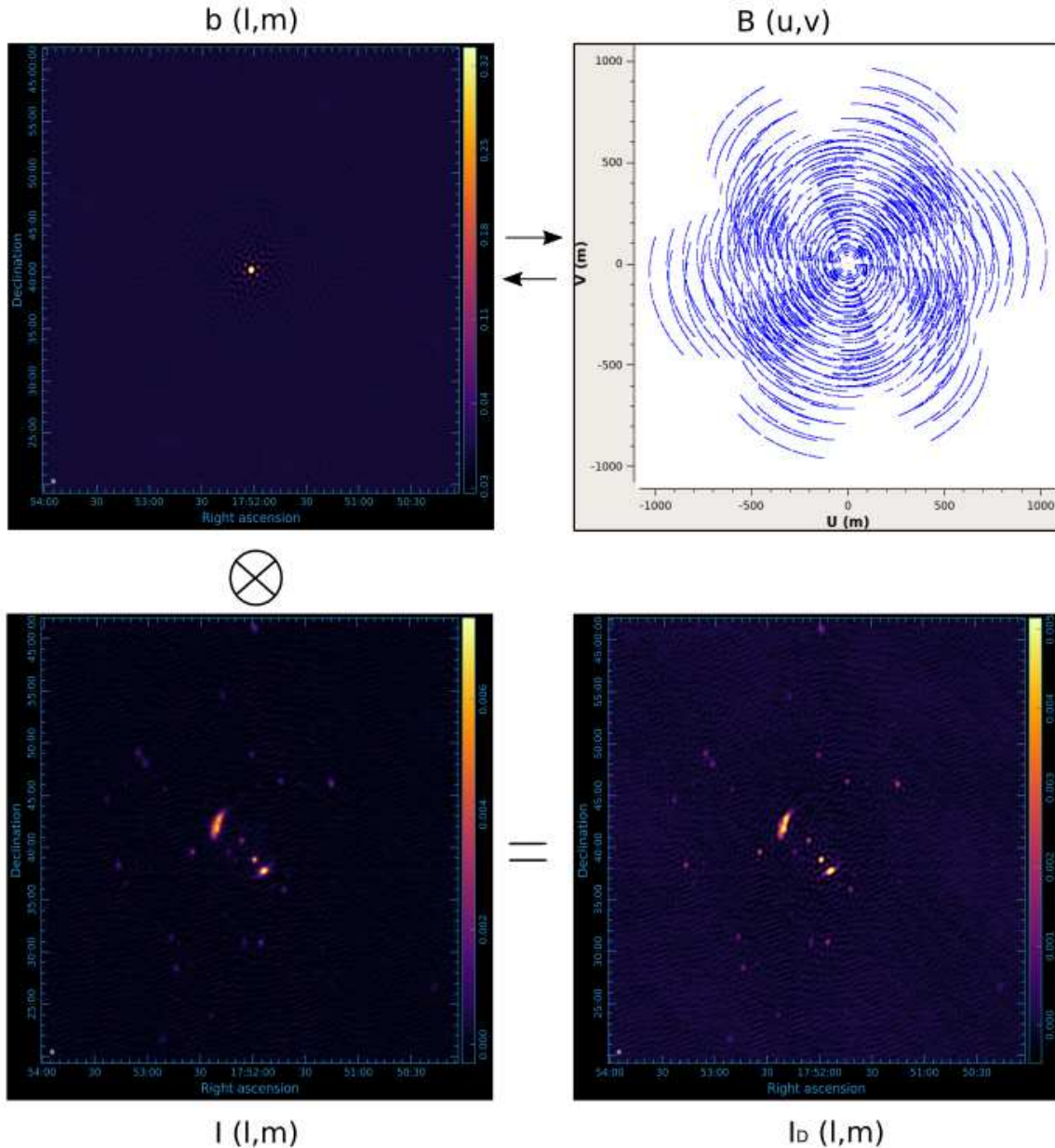
Figure 11. Example of quantities involved in the imaging process, using data from the JVLA analyzed in this thesis. The top left panel reports the psf or dirty beam, that is the Fourier transform of the uv plane coverage, in the top right panel. The psf, convolved with the 'true' sky brightness, bottom left panel, gives the dirty image in the bottom right panel, where some arrifacts are clearly visible. Colorbars are in Jy/beam.

Including these visibility domain gaps through the Fourier transform produces aliased features in the resulting image, the magnitude of which depends on the extent and locations of

gaps in the (u, v) plane and the brightness of emission on sampled scales. If the (u, v) plane has been reasonably well sampled, the synthesized beam will consist of a compact central positive feature surrounded by lower-amplitude positive and negative sidelobes. These sidelobes distribute the brightness via the point spread function throughout the image and can cause significant artifacts depending on the brightness distribution and sampling. However, a dirty image can be improved through deconvolution techniques to minimize the effects of incomplete spatial frequency sampling.

The resolution of the dirty image ultimately depends on how the interferometer antennas are arranged. In general, distributions connected via a Fourier transform scale inversely to each other: narrow distributions in one domain correspond to wide distributions in the other, and vice versa. For example, if the set of discrete points $B(u, v)$ is clustered around the origin of the (u, v) plane (a compact configuration), the central beam feature $b(l, m)$ will be wide, yielding a low-resolution image. Conversely, a more widely distributed set of points in the (u, v) plane yields a narrower beam and higher-resolution image. Resolution is fundamentally limited by the extent of the longest baselines in a given configuration. The minimum scale discernible in the image is limited by these maximum baselines. A useful approximation for interferometric resolution is:

$$\theta_{\mathrm{res}} = k \frac{\lambda}{L_{\mathrm{max}}}, \tag{3.27}$$

where k is a weighting-dependent constant (typically ~ 1), λ is the observing wavelength, and L_{max} is the longest baseline in the array.

Another important limitation of interferometric arrays is their insensitivity to large angular scales. Theoretically, his insensitivity arises because arrays cannot sample spatial frequencies lower than those provided by a baseline equal to an antenna diameter. In practice, no spaces inferior to the minimum baseline are sampled: visibilities near the origin of the (u, v) plane are not sampled, leading to the so-called zero-spacing problem. This biases the resulting image toward compact, small-scale features. The maximum recoverable scale (MRS) of an interferometer is approximately:

$$\theta_{\mathrm{MRS}} \approx 0.6 \frac{\lambda}{L_{\mathrm{min}}}, \tag{3.28}$$

where L_{min} is the shortest baseline in the array configuration.

4.3.1 The JVLA

The Karl G. Jansky Very Large Array (VLA) is a 27–element interferometric array, arranged along the arms of an upside-down Y (as in Figure 12), which produces images of the radio sky at a wide range of frequencies and resolutions [2]. The VLA is located at an elevation of 2100 meters on the Plains of San Agustin in southwestern New Mexico, and is managed from the Pete V. Domenici Science Operations Center (DSOC) in Socorro, New Mexico.

The basic data produced by the VLA are the visibilities, or measures of the spatial coherence function, formed by correlation of signals from the array's elements. The most common mode of operation will use these data, suitably calibrated, to form images of the radio sky as a function of sky position and frequency. Another mode of observing, commonly called phased array, allows operation of the array as a single element through coherent summation of the individual antenna signals. This mode is most commonly used for VLBI observing and for

---

[2] See https://science.nrao.edu/facilities/vla/docs/manuals/oss for more details

observations of rapidly varying objects, such as pulsars.

The VLA can vary its resolution over a range exceeding a factor of ∼50 through movement of its component antennas. There are four basic antenna arrangements, called configurations, whose scales vary by the ratios 1 : 3.28 : 10.8 : 35.5 from smallest to largest. These configurations are denoted D, C, B, and A, respectively.

The VLA completes one cycle through all four configurations in an approximately 16 month period. Observing projects on the VLA will vary in duration from as short as 1/2 hour to as long as several weeks. Most observing runs have durations of a few to 24 hours with only one or, perhaps, a few target sources. However, since the VLA is a two-dimensional array, images can be made with data durations of less than one minute. This mode, commonly called snapshot mode, is well suited to surveys of relatively strong, isolated objects.

All VLA antennas are outfitted with eight receivers providing continuous frequency coverage from 1 to 50 GHz. These receivers cover the frequency ranges of 1–2 GHz (L-band), 2–4 GHz (S-band), 4–8 GHz (C-band), 8–12 GHz (X-band), 12–18 GHz (Ku-band), 18–26.5 GHz (K-band), 26.5–40 GHz (Ka-band), and 40–50 GHz (Q-band). Additionally, all antennas of the VLA have receivers for lower frequencies, enabling observations at P-band (200–500 MHz). These low frequency receivers also work at 4-band (54–86 MHz), and new feeds have been deployed on all VLA antennas to observe at this frequency range.

The VLA correlator is both powerful and flexible. It is important to realize that the VLA correlator is fundamentally a spectral line correlator and that even continuum observations are done in a wide-band mode with many channels.
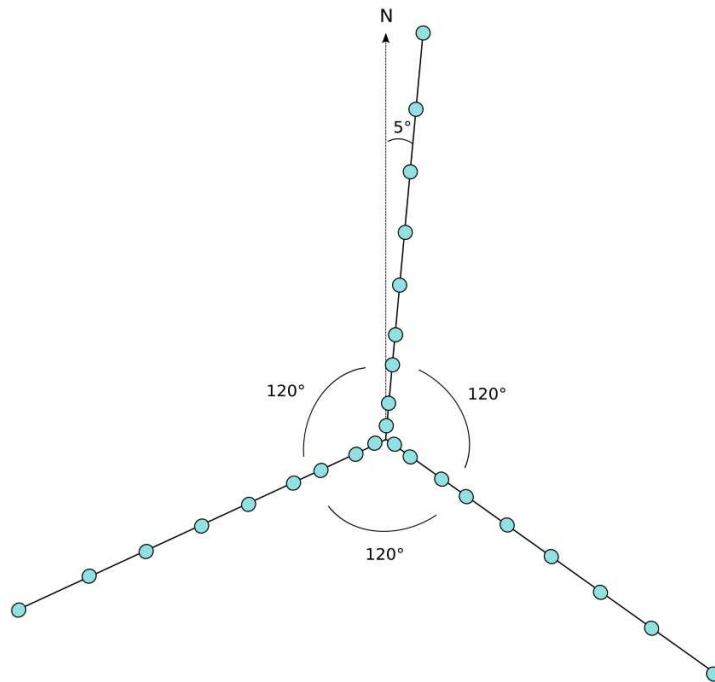
Figure 12. JVLA antenna configuration.

5

Observations and data reduction

This section reports the observations and data analysis carried out for SRT and JVLA data. While the focus of this thesis lies in the analysis of SRT data at high frequencies, the analysis of interferometric JVLA data at 1.6 GHz is an interesting step that validates the results obtained for the spectral index estimation obtained in Section 6.2 and allows to obtain more information regarding the polarization of the source.

5.1 SRT data

This section outlines the data reduction steps carried on with SRT data at 18.6 GHz (project code 18-23, P.I. Francesca Loi). In section 5.1.1, the dataset is described, while section 5.1.2 outlines the calibration steps.

5.1.1 The dataset

Data were taken with the Sardinia Radio Telescope K-band receiver, at frequency centered around 18.6 GHz, between November 2024 and January 2025. The choice of the lower end of the bandwidth is due to the spectral properties of the sources. Wanting to detect also the source polarized emission, the SARDARA backend was used (SArdinia Roach2-based Digital Architecture for Radio Astronomy, [82]). The adopted configuration provides a bandwidth of 1500 MHz divided into 1024 spectral channels for both polarizations (right and left polarization, identified next as RR and LL).

Data were taken in 15 different days, with observations lasting 5.5 hours each, considering 4 hours on the target and around 1.5 hours on the calibrators, for a total of 82.5 hours. The calibrators chosen were 3C286 to calibrate the bandpass, the RL shift and the absolute polarization angle, 3C295 to calibrate the counts to Jansky, and 3C84 to calibrate the leakage. A skydip scan was also performed, to evaluate the atmosphere opacity. Due to the LSTs of the source, the observations took place between LSTs 17:40 and 23:10.

For each observation day the dataset is composed of:

- 3 scans of 16 subscans each for 3C286

- 1 scan of 20 subscans for the SKYDIP scans

- 2 scans of 2 subscans for the CAL_ONOFF calibration

- 2 scans of 16 subscans each for 3C295

- 2 scans of 58 subscans each in the RA direction for the target

- 2 scans of 58 subscans each in the DEC direction for the target

- 3 scans of 16 subscans each for 3C84

with exceptions made on a day-to-day basis in cases of corrupted data. More details on the purpose of the different scans are provided in section 5.1.2.

5.1.2 Data reduction

The data reduction was performed with the proprietary Single-dish Spectral-polarimetry Software (SCUBE; [87]). In the following, the steps of the calibration procedure are presented.

Firstly, data were flagged considering the channels known to cause problems at the backend level, the so named 'birdies'. An auto-flagging of the data was then performed, to eliminate evident outliers and trends due to Radio Frequency Interference (RFI) and instrumental problems.

The data were first calibrated using the CAL_ONOFF scans. These scans are taken by pointing the telescope at a patch of sky free from bright radio sources. Initially, a scan of the empty sky is recorded, followed by the injection of a known calibration signal. This procedure is used to calibrate the gain and delay differences between the right and left polarizations of the receivers.

A fit of the SKYDIP scans was performed to correct for the atmospheric contribution to the system temperature, as in the example in the left panel of Figure 13.
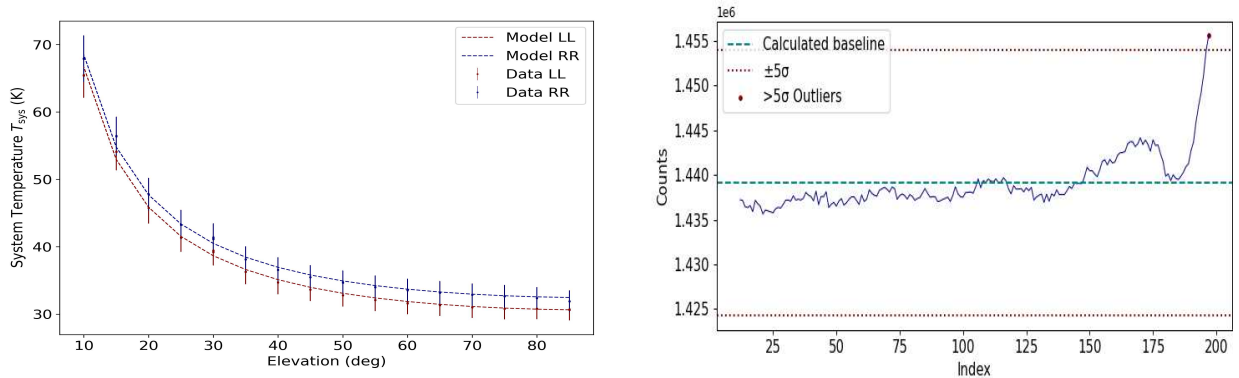
Figure 13. *Left*: Skydip fit for the system temperature on 27/11/2024. In this case the recovered τ is of 0.033 ± 0.005, and the system temperature, for LL and RR polarization respectively, is of 19.5624 ± 0.0004 K and 21.3934 ± 0.0006 K. *Right*: Baseline calculation and outlier identification. The example shows a subscan in polarization RR of 3C84. The baseline level before removing the outliers is clearly affected by a vertical offset.

The formula [21] used for the fitting is:

$$T_{sys} = T_0 + T_{sky} \tag{5.1}$$

where T_{sky} is given by:

$$T_{sky} = \eta_F \left[T_{atm} \left(1 - e^{-\tau/\sin(el)} \right) + T_{bgk}\, e^{-\tau/\sin(el)} \right] \tag{5.2}$$

where η_F is the telescope efficiency, τ is the zenith opacity, and $1/\sin(el)$ accounts for the variation of air mass with elevation. The background temperature T_{bgk} is given by $T_{bgk} = T_{CMB} + T_{gal}$, accounting for both the cosmic microwave background (CMB) and galactic contributions. The atmospheric temperature at the SRT can be estimated as:

$$T_{\mathrm{atm}} = 0.683 \cdot T_{\mathrm{ground}} + 78 \text{ K.} \qquad (5.3)$$

The next step involves baseline identification and subtraction for the calibrators. For this purpose, only the first 10% and last 10% of each scan (in time) are considered, as these regions are assumed to be flux-free and representative of the baseline level. This operation was performed on the scans for 3C286, 3C295, 3C84, and CAL_ONOFF. After this operation, an initial manual inspection was performed to flag data points that deviated by more than 5σ from the baseline, calculated within the selected intervals, as in the right panel of Figure 13. These deviations include residual RFI not identified during the flagging process, as well as cases in which the calibrators appear in the first or last part of the scan, causing a systematic error in the baseline calculations.

The bandpass was then calibrated to account for the different frequency responses of the seven feeds[3] of the K-band receiver [93], as shown in Figure 14. This calibration determines a scaling factor for each spectral channel, needed to match the observed calibrator peak brightness. A Gaussian model is used to represent the calibrator intensity, with the full width at half maximum (FWHM) scaled according to frequency. Only data points within the FWHM are selected for the solution to ensure accurate fitting.
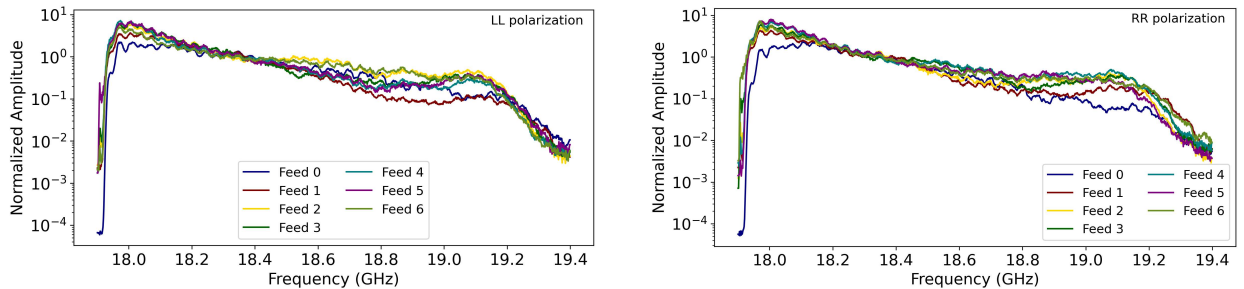
Figure 14. *Left:* Left polarization bandpass calibration solutions for the multi-feed system. *Right:* Right polarization bandpass calibration solutions for the multi-feed system.

The calibrators are then gridded: this operation grids the On-The-Fly map (OTF) into an image. OTF mapping is a technique used in single-dish radio astronomy to efficiently scan large areas of the sky. Instead of stopping the telescope at fixed grid positions (as in pointed or raster mapping), the telescope moves continuously while collecting data, along the RA or DEC direction, leading to faster and smoother sky coverage. One important aspect to consider is that the telescope must accelerate at the beginning and decelerate at the end of each subscan (i.e., each individual line of the map), which leads to non-uniform coverage near the edges of the image. Additionally, time is spent reversing the scan direction between subscans—a period during which the telescope is not observing the target. These effects must be taken into account when planning observations times.

The flux calibration was performed using the standard calibrator 3C286. A two-dimensional Gaussian model was fitted to the calibrator maps for each of the seven feeds of the K-band

---

[3]The outputs from each feed system are the left- and right-hand circular polarizations. One horn is at the center, while the remaining six are arranged according to a hexagonal patter around it. The movement of the feeds across the sky during on-the-fly scans causes the edges of the field to be only partially covered, generating artifacts that have to be excluded during data analysis.

receiver, separately for the LL and RR polarizations. The fitting was carried out using a combination of random search and gradient descent. The fitting parameters were adjusted to ensure both convergence and flexibility in the model. The fit was limited to a small region of the image in which the source was collocated, defined using an annular region centered at central pixel coordinates, excluding noisy regions. Once the model was fitted, the flux calibration was performed converting from counts to Jansky. This process allowed for accurate conversion of raw counts to physical flux densities (Jy) by fitting the calibrator and determining the appropriate scaling factors per channel and polarization [100].

An estimate of the flux density calibrator uncertainty was obtained by comparing the results with the calibrator 3C295. This source was calibrated using the scaling derived from 3C286, and the resulting peak flux densities were fitted for the LL and RR polarizations as well as for the total intensity I. The measured flux densities were then compared to the expected theoretical values for 3C295 at 17.975 GHz, assuming a bandwidth of 1250 MHz. The comparison was carried out by fitting a 2D Gaussian to each calibrated image and computing the relative error as the difference between the fitted peak and the expected flux, normalized by the latter. This procedure was repeated for each of the seven feeds and for multiple scan pairs. The overall calibration accuracy was evaluated by examining the distribution of these relative errors across all feeds and polarizations. This stage was necessary to find new outliers thatbecame evident after the flux density calibration due to peaks in the fluxes, probably due to residual RFIs (see Figure 15), and perform an additional manual flagging step.
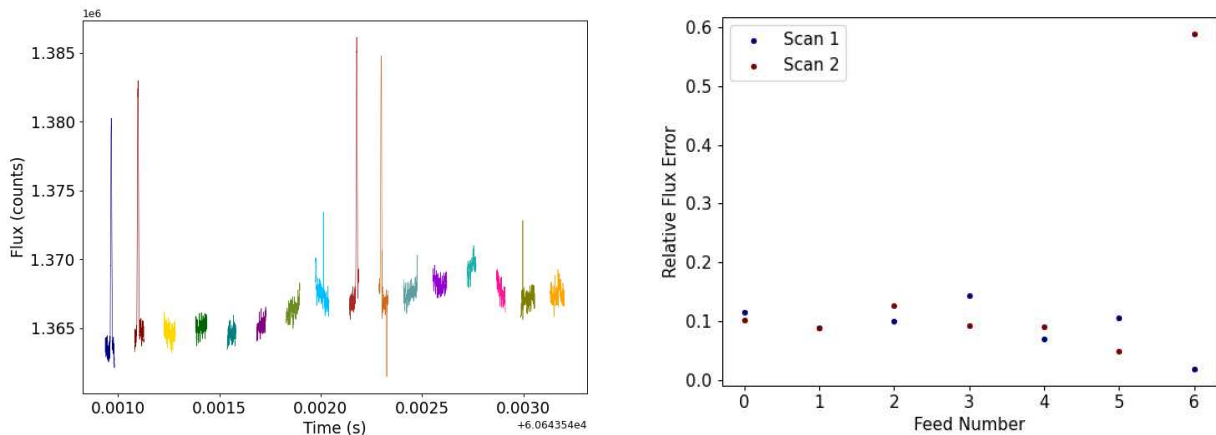
Figure 15. *Left*: For this scan of polarization RR of 3C295 taken in date 29/11/2024, multiple subscans need to be flagged, showing clear signs of errors. *Right*: Effect of the RFI in the subscans on the relative error in the flux calculation. 2 scans of observations are taken for every round of observations for 3C295.

The last calibration steps are dedicated to the polarization calibration. The phase offset between the RR and LL polarizations was first determined using the CAL_ONOFF scans. Subsequently, the instrumental leakage terms were derived using scans of the unpolarized calibrator 3C84, in order to quantify the amount of spurious polarized flux introduced by the system. The final polarization angle calibration was performed with 3C286, applying corrections for the RL phase offset, leakage, and absolute polarization position angle using the known polarization properties of the source at 18.6 GHz (see Figure 16).

At the end of the polarization calibration procedure, a final round of manual flagging was required to remove residual outliers in the fractional polarization and polarization angle maps.
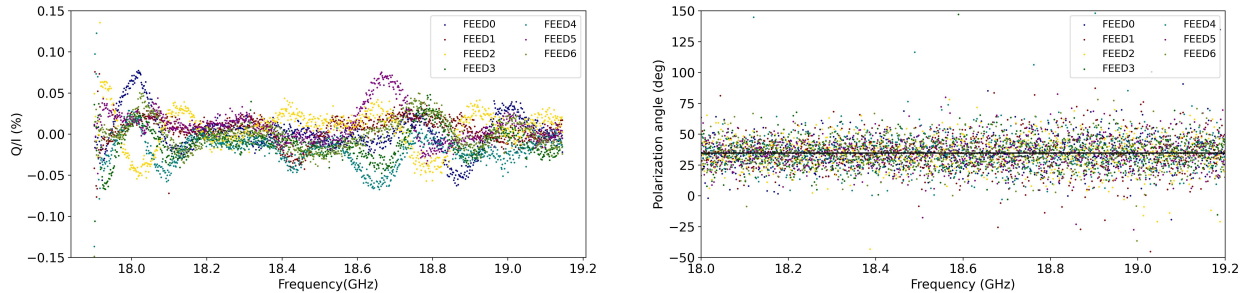
Figure 16. *Left*: Leakage calibration: the leakage is of the order of some %, as one would expect. *Right*: Polarization angle after calibration. The model value is of 34.6 degrees, shown with a black line.

The final calibrated data in the Stokes parameters LL, RR, Q, and U were produced through a final gridding process. As a first step, scan-based baseline subtraction was applied to the individual scans by fitting and removing a first- or second-order polynomial, excluding regions defined by a mask file to avoid contamination from bright sources. The mask was constructed based on the 3σ contours from NVSS data at 1.4 GHz. Baseline fitting was performed iteratively using a 5σ clipping threshold to reject outliers. Gridded maps were then created with a resolution of 128×128 pixels and a pixel scale of 15 arcseconds. This procedure was applied to all feeds and scan directions for both RR and LL polarizations. The same process was used for Stokes Q and U, following the application of polarization-specific calibration corrections, including RL phase offset, instrumental leakage, and absolute polarization angle, to then proceed to gridding.

The final images were produced by stacking the calibrated maps using a wavelet-based approach to improve the signal-to-noise ratio and suppress residual noise. The stacking was performed using the Haar wavelet transform with three decomposition levels [87]. A weighted average was applied during stacking, using a global plane weighting scheme, with noise estimated from an annular region around the center of the field. A spatial kernel of 4 pixels and patch size of 4 were used for smoothing, and a mask was applied to exclude low-quality or contaminated regions.
Stokes I was computed by summing the separately stacked LL and RR images. All Stokes parameters (LL, RR, I, Q, and U) were then mosaicked considering all the channels, producing 'splatted maps'.
To further enhance the quality of the final maps, wavelet-based denoising was applied on the splatted maps of I, Q, and U. Hard thresholding was performed with the Haar wavelet. Following denoising, polarization products were computed to have the polarization intensity, angle, and fractional polarization from the denoised I, Q, and U images. Noise levels were set manually, based on prior estimates on the noise from the images produced for each Stokes parameter.
An additional stacking and denoising process was also performed on masked and blanked Stokes I, Q and U data, to eliminate remaining RFIs (see Figure 17), using weighted averaging and the same wavelet denoising pipeline to produce the final intensity image consistent with the polarization analysis.
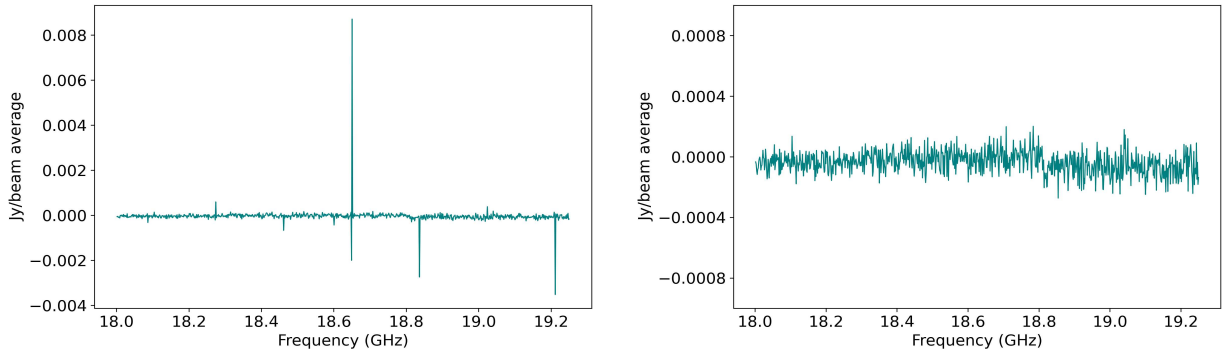
Figure 17. *Left:* Stokes *I* map before blanking and RFI removal. *Right:* Stokes *I* map after masking and wavelet denoising. Note the different scale of the 2 images.

The final total intensity image is reported in Figure 18. The SRT manages to recover the features for both the northern and the southern relics, catching more emission at the eastern edge of the northern relic with respect to the NVSS data, for which white contours are reported.
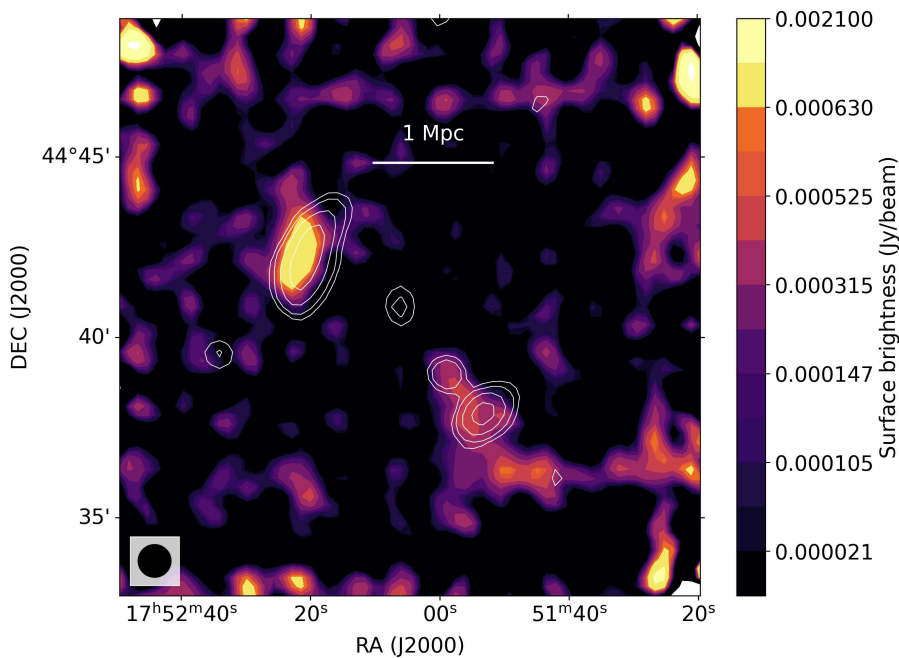
Figure 18. Stokes I image from SRT data at 18.6 GHz with beam of 0.9'. Contours at 2, 3, 5, 10,20 σ from the NVSS image at 1.4 GHz, with σ=0.4 mJy/beam.

The SRT detects emission from the northern relic centered in a different part with respect to the NVSS, likely because the single-dish is more sensitive to diffuse, large-scale emission that the interferometer resolves out, and its broader beam smooths and shifts the apparent peak of the signal.

5.2 JVLA data

This section comprehends the dataset description and data reduction of data in the L-band from the JVLA radio interferometer.

5.2.1 The dataset

The observations analyzed in this work were carried out with the Karl G. Jansky Very Large Array (JVLA) on December 18, 2011, as part of project `uid://evla/pdb/4982159` (PI: Dr. Annalisa Bonafede). The array was in the D configuration, consisting of 26 antennas, each 25 meters in diameter. Data were recorded in full polarization mode (RR, RL, LR, LL), with a total of approximately 3.84 million visibilities spanning an observing time of 3.5 hours (17:53 to 21:22 UTC).

The correlator setup included 16 spectral windows, each with 64 channels of 1 MHz width, resulting in a total bandwidth of 1024 MHz across the L-band frequency range (from ~1.19 to ~1.96 GHz). The integration time was 3 seconds.

The standard VLA calibration strategy was used. The primary flux and bandpass calibrator was 3C286 (1331+305), observed over several scans for reliable gain, bandpass and polarization calibration. The source 3C295 (1411+522) was used as a secondary amplitude calibrator. The phase calibrator J1734+3857 was observed regularly throughout the session to monitor and correct for time-variable atmospheric phase fluctuations.

A total of four fields were observed, with coverage optimized for calibration purposes. The array delivered good *uv* coverage suitable for high-fidelity imaging and accurate calibration transfer.

5.2.2 Data reduction

Data reduction was carried out with CASA [23], the NRAO Common Astronomy Software Applications, a comprehensive software package to calibrate, image, and analyze radio astronomical data from interferometers and single-dish radio telescopes. The steps for total intensity calibration included:

- Flagging high-amplitude outliers in time and frequency and flagging based on statistical deviations.

- Delay calibration, that solves for the per-antenna delay offset (in nanoseconds) that causes a linear phase slope with frequency. These delays can come from different cable lengths, clock offsets between antennas and instrumental phase shifts not accounted for by the initial setup.

- Bandpass calibration to determine and remove systematic, frequency-dependent effects that distort the spectrum.

- Gain calibration to determine complex gain solutions (amplitude and phase) for each antenna as a function of time. These solutions are applied to correct the observed visibilities so they reflect the true sky brightness.

- Self-calibration, an iterative refinement of the gain solutions using a sky model derived from the data itself.

The polarized image was produced using 3C286 as a polarized position-angle calibrator. The polarization calibration included the following steps:

- Cross-hand delays (RL, LR) were solved independently for each spectral window to correct for residual delay differences between the R and L polarizations on the reference antenna used during the initial delay calibration.

- Solutions were derived for instrumental polarization leakage (D-terms).

- Having calibrated for the instrumental polarization, the total polarization is now correct, but the R-L phase still needs to be calibrated in order to obtain an accurate polarization position angle.

- The calibration solutions were then applied to the target data.

The results are reported and discussed in Section 7.2.

The imaging for both total intensity and polarization was performed with WSCLEAN [90], a widefield interferometric imager that implements a version of CLEANing (see appendix B). We adopted a Briggs weighting with robust -1 and a mask obtained by the dirty image itself considering the source at 3σ from the rms of the image. The results of the total intensity imaging are reported in Figure 19. One pixel has 5" side, the beam size is 25.0" x 22.3".
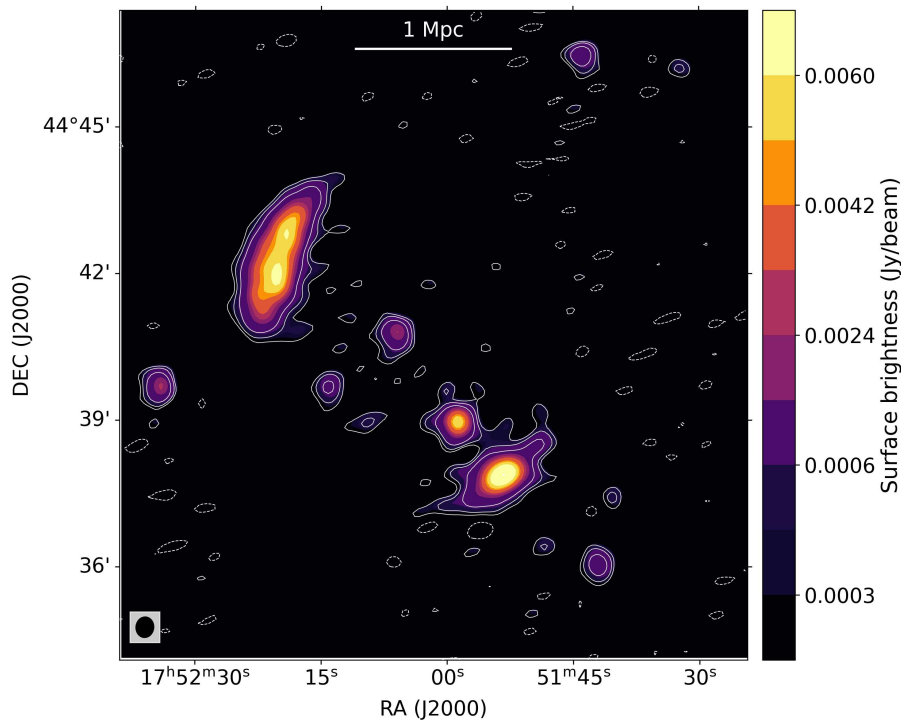
Figure 19. The figure shows the imaging of JVLA total intensity data at 1.6 GHz, with white contours at 3,5,10 σ, with $\sigma = 0.09$ mJy/beam, beam of 25.0" x 22.3". Dashed lines indicate negative contours at -2σ.

	SRT	JVLA
Project code	18-23, P.I. Loi Francesca	4982159, P.I. Bonafede Annalisa
Dates of observations	November 2024 - January 2025	December 18, 2011
Duration of observations	82.5 hrs	3.5 hrs
Central frequency	18.6 GHz	1.6 GHz
Frequency band	1500 MHz	770 MHz
Spectral resolution	1.5 MHz	1 MHz
Spatial resolution	$0.9' \times 0.9'$	$25.0'' \times 22.3''$

Table 2. Summary of the SRT and JVLA observations used in this work.

6

Total intensity results

This section presents the spatial characterization and flux density estimation of the radio relics in MACS J1752.0+4440 (Section 6.1). The spectral properties of the relics are presented in Section 6.2, with derivation of shock Mach numbers in Section 6.3. Finally, Section 6.4 reports the unexpected detection of the Sunyaev–Zel'dovich effect in the cluster.

6.1 Characterization and flux estimate

In this section the relics are characterized in morphology and flux density, considering SRT and JVLA data.

6.1.1 SRT data

Figure 20 shows the resulting 18.6 GHz SRT image obtained by averaging the data between 18 GHz and 19.2 GHz. The noise is 0.2 mJy/beam, the beam size is 0.9 arcmin. The norhern radio relic was clearly detected at 3σ, the southern radio relic at 2σ.
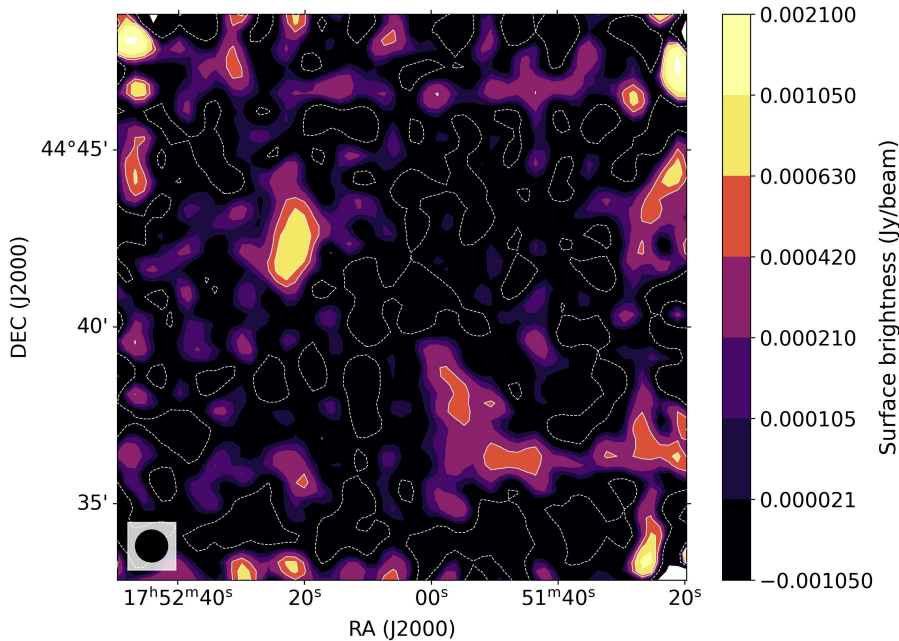
Figure 20. SRT total intensity image at 18.6 GHz with beam of 0.9'. Contours in white at 2 and 3 σ from the SRT image, with σ=0.2 mJy/beam. Dashed lines indicate negative contours at -3σ.

To identify precisely the NE and SW relics, the cumulative surface brightness within concentric ellipses was analyzed, as shown in Figure 21: the cumulative brightness curve reaches a plateau at the point where the source emission ceases to contribute significantly, and only background noise remains.

Considering this limits, the NW relic extends up to 0.85 and 0.50 Mpc along its axes, while

the SW relic reaches up to 0.48 and 0.37 Mpc. The relics are ∼1.2 Mpc apart from the center of the cluster. We also detected the faint radio source (probably a radio galaxy) at the center of the SW arc-like radio source, delineated by the NVSS contours at 1.4 GHz in Figure 18, also observed by van Weeren et al. [130].
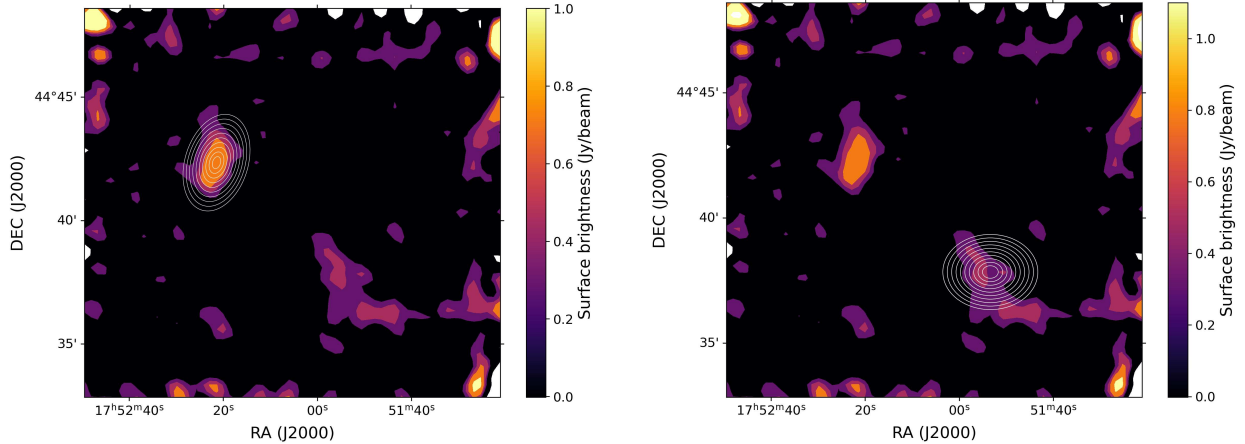
Figure 21. Aperture photometry performed to determine the flux of NE and SW relics from SRT data at 18.6 GHz, with beam of 0.9'.
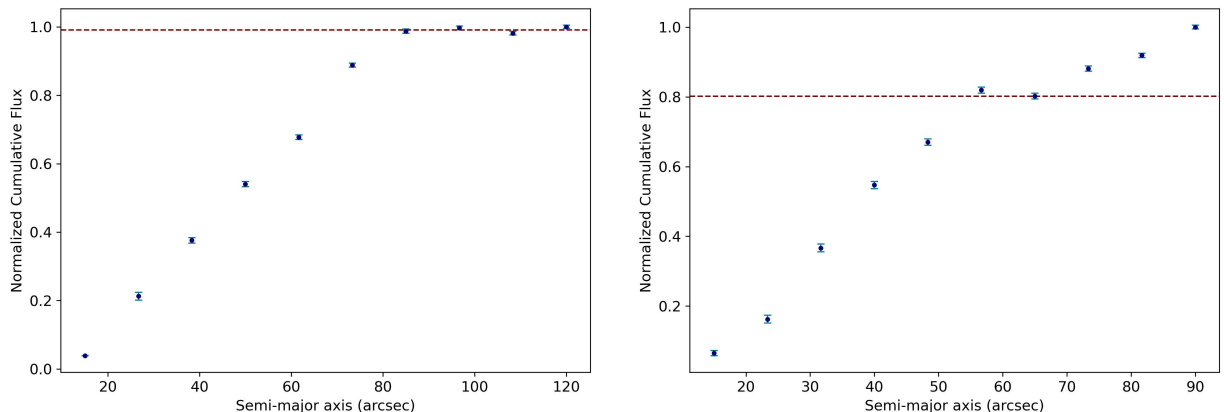
Figure 22. Cumulative surface brightness for the northern (left) and southern (right) relics. The red lines indicate the reference normalized flux levels used to define the extent of the relics. For the southern relic, a successive bump can be seen above 80 arcseconds, due to the proximity to a radio galaxy just north-east of the SW relic.

The flux density is obtained by multiplying the surface brightness within the selected region (in pixel units) by the ratio of pixel area to beam area in pixels, i.e., $S_\nu = S_{\mathrm{pix}} \times (\mathrm{area}_{\mathrm{px}}/\mathrm{area}_{\mathrm{beam}})$. An additional offset of $(4.0 \pm 0.9) \cdot 10^{-5}$ Jy/beam is added to account for the Sunyaev–Zel'dovich effect contribution (see Section 6.4).

The total uncertainty on the flux density is computed as:

$$\Delta S_\nu^{SRT} = \sqrt{(f \cdot S_\nu)^2 + \sigma^2 \cdot N_{\mathrm{beam}} + (\Delta_{\mathrm{BL}})^2},$$ (6.1)

where f is the systematic flux density uncertainty (assumed to be 10%), σ is the rms noise of the image, N_{beam} is the number of independent beams covering the relic region, and Δ_{BL}

is the uncertainty associated with the baseline subtraction (see e.g. [78]). The rms noise of the image was estimated by placing ellipses—identical in size to those used for the flux density measurement—at multiple positions in cold sky regions across the image, obtaining a uniform coverage of the background. These ellipses were positioned after masking the source region using the detected boundaries from our detection, combined with 3σ NVSS contours. The noise as rms was then computed within each ellipse, and the median value across all regions was adopted as the final estimate, as it is less sensitive to outliers than the mean.

The final estimates for the flux densities are:

$$S_{18.6,\ \mathrm{NE}} = 2.4 \pm 0.3 \ \mathrm{mJy}$$
$$S_{18.6,\ \mathrm{SW}} = 1.5 \pm 0.2 \ \mathrm{mJy}$$

6.1.2 JVLA data

Figure 23 shows the results from JVLA data reduction performed with CASA.
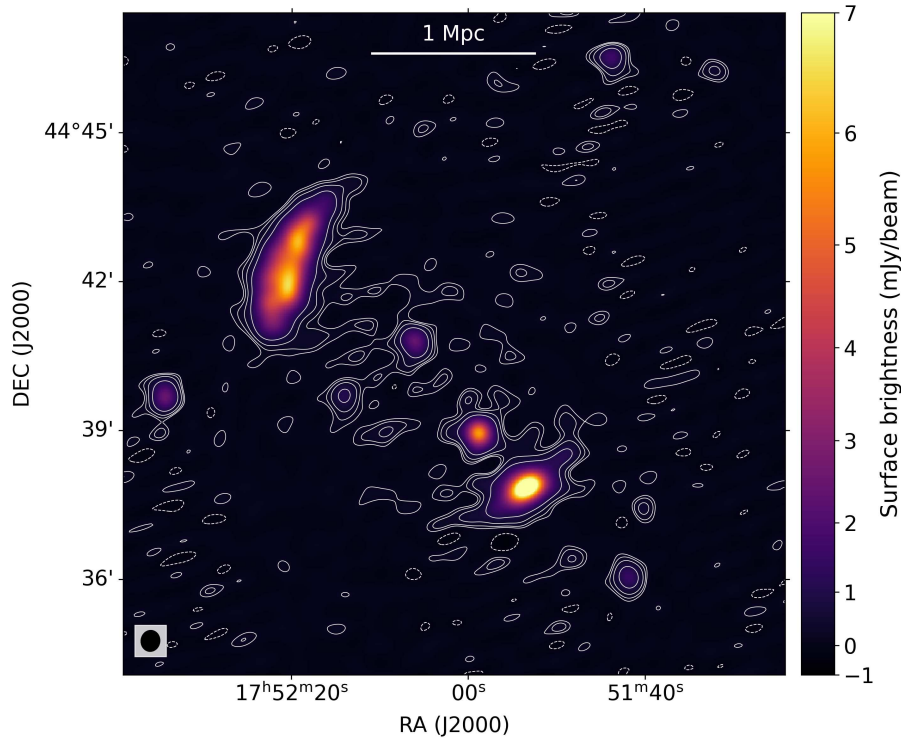
Figure 23. The Figure shows JVLA total intensity data at 1.6 GHz, with white contours at 2,3,5,10 σ, with $\sigma = 0.09$ mJy/beam, to highlight the presence of diffuse emission between the relics. The beam is 25.0" x 22.3". Dashed lines indicate negative contours at -2σ.

JVLA data reveal that the northern relic exhibits bright filamentary emission in its central region, with two prominent hotspots, and diffuse extensions toward the edges. The southern relic is clearly separated from the compact radio source located to its north-east; the two appear connected by a faint "radio bridge" detectable at the 3σ level, which is likely an instrumental artifact arising from their relative proximity in the projected plane.
The image shows diffuse emission between the 2 relics, and detects the presence of a radio halo in the cluster, classified as such because the radio emission follows the X-ray emission

from the ICM (as reported by van Weeren et al. [130]). The two brightest compact sources between the relics are probably AGNs in the cluster, based on the colors of their optical counterparts.

Because of the presence of this diffuse radio emission visible at 1.6 GHz between the relics, using concentric ellipses to estimate the flux density was inconclusive. The flux density has then been estimated considering the contours at 3σ for the NE relic and at 4σ for the SW relic, to better distinguish it from the radio galaxy located just NE of it, with σ=0.09 mJy/beam estimated from the rms of the image. The obtained regions are reported in Figure 24. From JVLA data, the relics have estimated sizes of 0.84 Mpc x 0.26 Mpc and 0.35 Mpc x 0.21 Mpc for the northern and southern relic respectively.

The estimates for the flux densities are:

$$S_{1.6,\ \text{NE}} = 59 \pm 6 \text{ mJy}$$
$$S_{1.6,\ \text{SW}} = 26 \pm 3 \text{ mJy}$$

The errors on the flux density have been computed from:

$$\Delta S_\nu^{JVLA} = \sqrt{(f \cdot S_\nu)^2 + \sigma^2 N_{\text{beam}}}, \tag{6.2}$$

not including the addition of a baseline due to the fact that the SZ effect is supposed to be negligible at these frequencies. In this case σ is given by the sum in quadrature of the errors associated with every pixel considered for the flux density computation, that is the general rms of the image. The factor f is again assumed to be 0.1 .
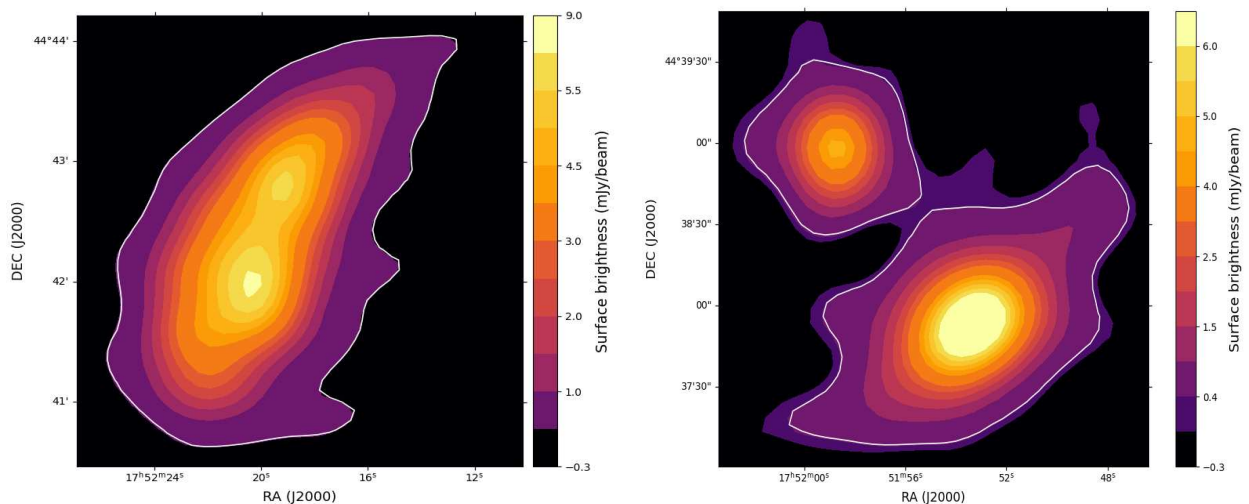

Figure 24. Regions considered to determine the flux of NE and SW relics from JVLA data at 1.6 GHz, beam of 25.0" x 22.3". Contours at 3σ for the northern relic (left) and at 4σ for the southern relic (right) are in white, with $\sigma = 0.09$ mJy/beam.

6.2   Spectral properties

The spectral image reported in Figure 25 shows the spectral index values across the relics, varying from 0.2 to 1.8, obtained considering the fluxes from SRT and JVLA data following the power-law:

$$S_\nu \propto \nu^{-\alpha}.$$

The NE relic shows a clear steepening of the spectral index going from the cluster periphery towards the center, as already noted by Bonafede et al. [13], as we would expect from a shock propagating from the center to the edge of the cluster. This steepening is thought to be caused by synchrotron and Inverse Compton losses in the shock downstream region, as discussed in Section 3.1. Instead, the southwest relic has a spectral index that is flatter within the radio emission, which may indicate a slight viewing angle to the radio emission [46].
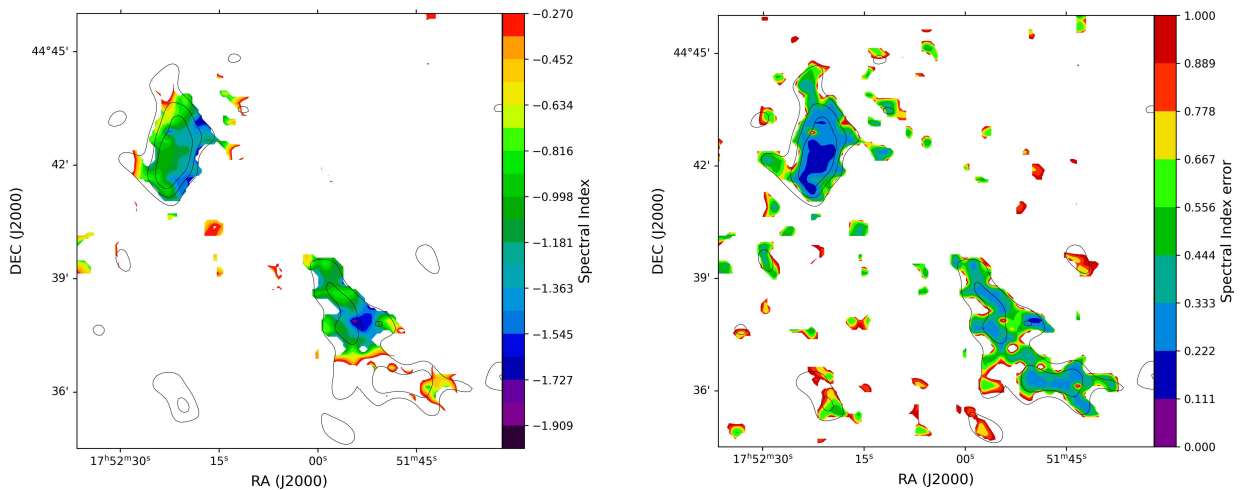
Figure 25. *Right:* Spectral map for MACSJ1752+4440 estimated from SRT and VLA images between 18.6 and 1.6 GHz. Contours from the SRT image at 1, 2, 3σ, with σ=0.2 mJy/beam. *Left:* Spectral map noise. The maps are masked to include only regions where the SRT signal-to-noise ratio is sufficient for reliable spectral index estimation. These maps should be interpreted qualitatively for visualization, as smoothing and contouring have been applied, which are not fully consistent with strict spectral index mapping procedures.

The flux densities obtained in the previous sections are reported together with measurements from other instruments in Table 3. Flux densities from the JVLA nd the SRT are the ones obtained as reported in the previous sections. Flux densities from the NVSS data [28], RACS [80] data and the LOTSS data release 2 [117] have been obtained by using 3σ contours, with σ obtained by evaluating the rms on the public images from the archives. The remaining measurements have been obtained from the literature on this source.

Figure 26 shows the integrated spectrum of the relics, i.e. the flux density of the relics as a function of frequency. These data are modeled with a power-law spectrum, with spectral indices reported in the figures.

	ν (MHz)	S_ν^{NE} (mJy)	S_ν^{SW} (mJy)	Reference
LOTSS	144	680 ± 70	280 ± 28	Shimwell et al. [117]
GMRT	323	410 ± 33	163 ± 13	Bonafede et al. [13]
RACS	887.5	115 ± 11	50 ± 5.3	McConnell et al. [80]
NVSS	1400	64 ± 6	28 ± 4	Condon et al. [28]
JVLA	1600	59 ± 6	26 ± 3	By this author
WSRT	1714	55.1 ± 2.9	25.7 ± 1.4	van Weeren et al. [130]
SRT	18600	2.4 ± 0.3	1.2 ± 0.2	By this author

Table 3. Flux density measurements at different frequencies, from literature and new estimates performed for this work. S_ν is the flux density, ν the relative frequency.

Figure 26 shows the spectral fit including the LOFAR data in red, while the light blue line represents a fit performed without the lowest-frequency point, which deviates from the trend defined by the other measurements.

The flux density for the southern relic from SRT data is expected to be under-estimated, since the relic is detected just at 2σ from the observations. This explains why the last point in the right panel of Figure 26 appears to be slightly out of the trend.
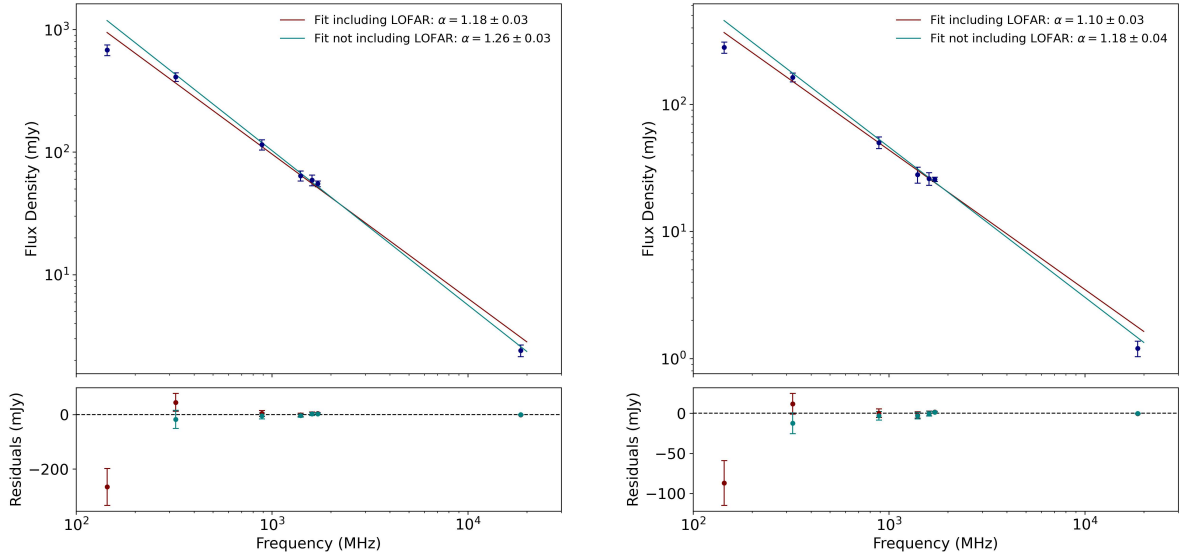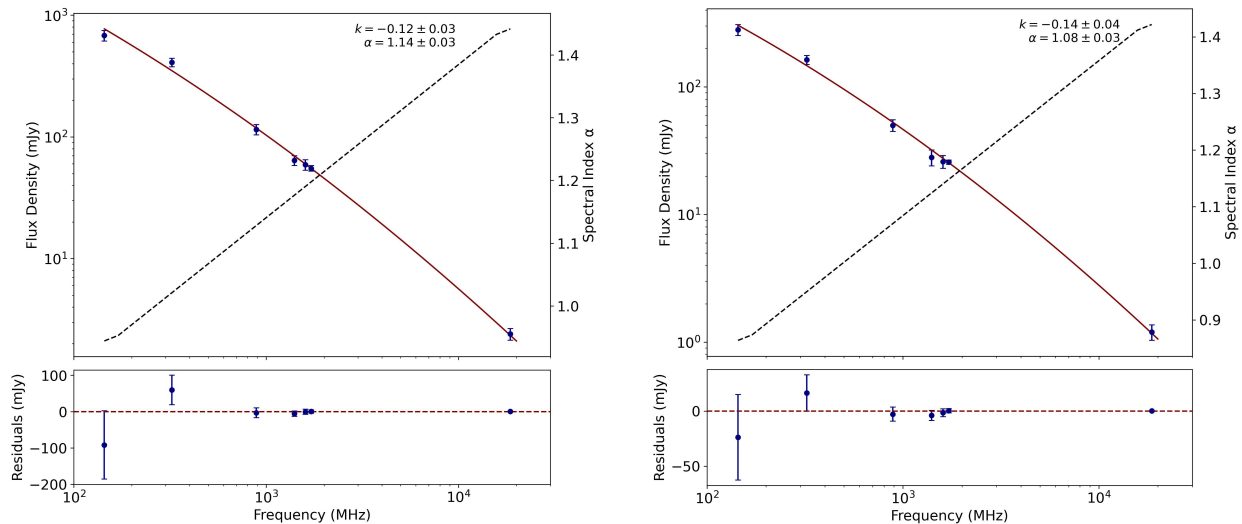

Figure 26. Spectral fit for northern (left) and southern relic (right). The maroon line represents the fit that includes all data, while the light blue line was obtained by excluding the LOFAR data at 144 MHz.

Since the spectral fit obtained including LOFAR data does not seem to be consistent with both LOFAR and SRT measurements, we discuss in the following some possible solutions.

To evaluate the deviation from a simple power-law model, we firstly propose to fit the data with a curved model, also implemented previously by Murgia et al. [88]. The radio spectrum is modeled with a simple modified power law of the form:

$$\log_{10}(S_\nu) = \log_{10}(S_0) - \alpha_0 \cdot \log_{10}\left(\frac{\nu}{\nu_0}\right) + k \cdot \left[\log_{10}\left(\frac{\nu}{\nu_0}\right)\right]^2 \qquad (6.3)$$

The model has three free parameters. The parameters S_0 and α_0 represent the relic flux density and spectral index at the reference frequency ν_0, respectively. The parameter k is the spectral curvature. The results are reported in Figure 27. This fit is adopted to discern if there is a significant curvature, identifiable at least at 3σ of the error of k itself. In our case, it is evident that a curved model seems better fitted to describe the data (see Figure 27).

Figure 27. Curved analytical spectral fit for northern (left) and southern relic (right), as per equation 6.3. The red line represents the curved analytical model fitted, while the black line refers to the spectral index variation along the curve, referring to the values on the right axes of the figures.

Since the curved model yields an acceptable representation of the data, a more physically grounded alternative is to adopt a Continuous Injection (CI) model for the spectral fit. This model predicts that sources are continuously replenished by a constant flow of fresh relativistic particles with a power law energy distribution. It presents as a synchrotron spectrum that is a power law with a spectral index $\alpha_{\mathrm{inj}} = (\delta - 1)/2$ below a critical frequency ν_{br}, and becomes progressively steeper beyond the break frequency ν_{break} due to radiative losses, with $\alpha_h = \alpha_{\mathrm{inj}} + 0.5$ above ν_{br}.

If there is no expansion and the magnetic field is constant, the break frequency ν_{br} (in GHz) depends on the elapsed time since the source formation τ_{syn} (in Myr), the magnetic field strength B (in μG), and the magnetic field equivalent to the Cosmic Microwave Background $B_{\mathrm{CMB}} = 3.25(1 + z)^2$ (in μG), according to:

$$\tau_{\mathrm{syn}} = 1590 \, \frac{B^{0.5}}{B^2 + B_{\mathrm{CMB}}^2} \, \frac{1}{[\nu_{\mathrm{br}}(1 + z)]^{\frac{1}{2}}} \tag{6.4}$$

The whole spectral shape cannot be described by an analytic equation, the two behaviours described being only the asymptotical ones, and has to be computed numerically.

In our analysis, the fit of the CI model to the data was performed using using synthetic spectra generated with the `synage++` package [85], and the best-fit parameters were obtained by minimizing the χ^2 between model and observed flux densities. Fitting the spectral data to the numerically computed CI spectrum, one obtains the break frequency ν_{break} and the injection spectral index α_{inj}, from which the source age is obtained if the magnetic field is

known [85]. Considering the magnetic field estimates presented in Section 7.3 between 0.5 and 8 μG, the value of $\tau_{\rm syn}$ varies roughly between 25 to 50 Myrs (with maximum radiative time reached for 3.5 μG).

Results are reported in Figure 28. When looking at CI models fitted, one must take into account that this model presents a relevant degeneration between α_{inj} and ν_{break}.

Considering for both the NE and SW relic a ν_{break} of 1 GHz, the spectral indices below the break result 1.00±0.08 and and 0.95±0.08 for the northern and southern relics respectively. Above the break the spectral indices are instead 1.30±0.05 (NE relic) and 1.27±0.06 (SW relic).
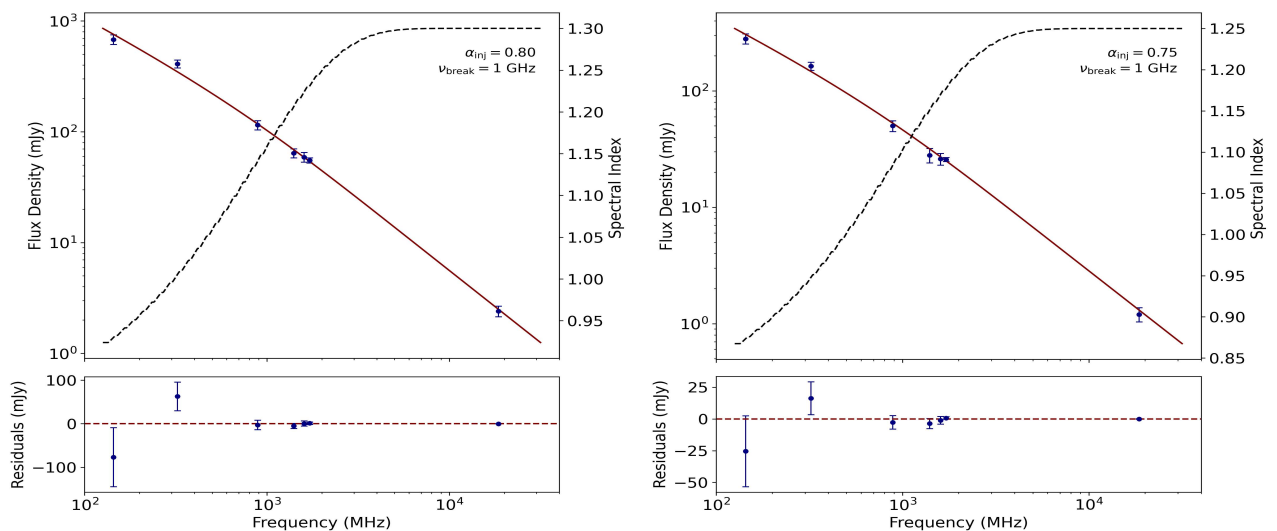

Figure 28. Continuous Injection spectral fit for northern (left) and southern relic (right). The red line represents the model fitted, while the black line refers to the spectral index variation along the curve, referring to the values on the right axes of the figures.

But adopting a curved spectrum when analyzing radio relics is not a common approach, since it is usually expected to find the ν_{break} at lower frequencies with respect to the ones at which the observations are taken.

This prompted a further analysis carried out aims to verify the reliability of the LOFAR measurements, which appear to deviate from the spectral trend well traced by data from the other instruments. We used as LOFAR data the high resolution mosaics of the LOTSS DR2 (Shimwell et al. [117]).
We performed a consistency check on these data: we extracted in-band spectra of point-like sources from JVLA data, complemented with RACS measurements, and compared them with the corresponding flux densities derived from LOFAR observations. The results of this comparison are shown in Figure 29.
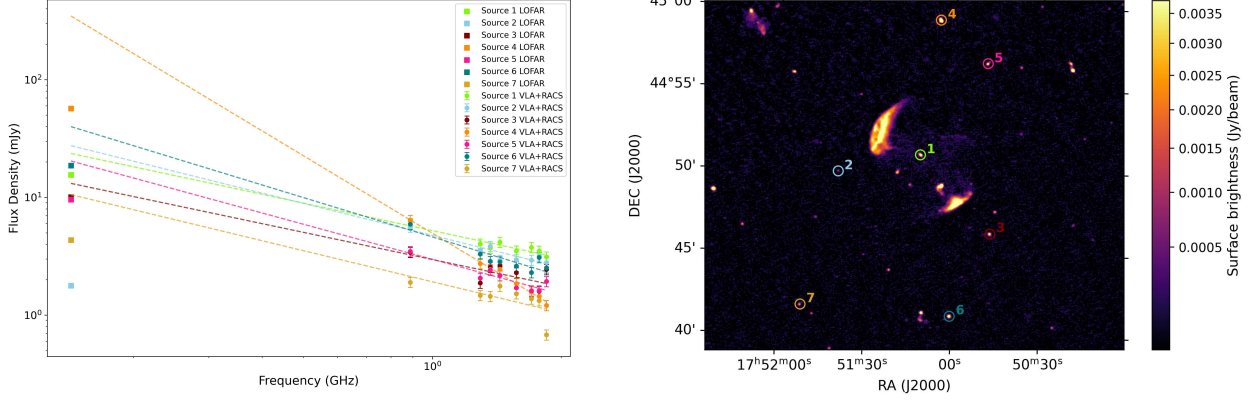
Figure 29. *Left :* Spectra of selected point-like sources in the LOFAR field. The linear fits have been computed considering JVLA and RACS data, with round markers. Square markers indicate LOFAR data, clearly under-estimated with respect to the fits for all the sources. This results do not change adding NVSS data to compute the fits. *Right :* LOFAR high resolution image of the field of view around MACS J1752+4440 at 144 MHz. The beam is of 6" x 6" (not shown to scale in the image due to its small size), one pixel has 1.5" sides.

From what reported in Figure 29, it can be inferred that the LOFAR flux densities are systematically underestimated, with the expected values being approximately 1.5 times higher than those actually measured.

If we take into account this factor of 1.5, the complete spectrum including the corrected LOFAR data results the one reported in Figure 30, fitted by power laws for both the northern and southern relic.
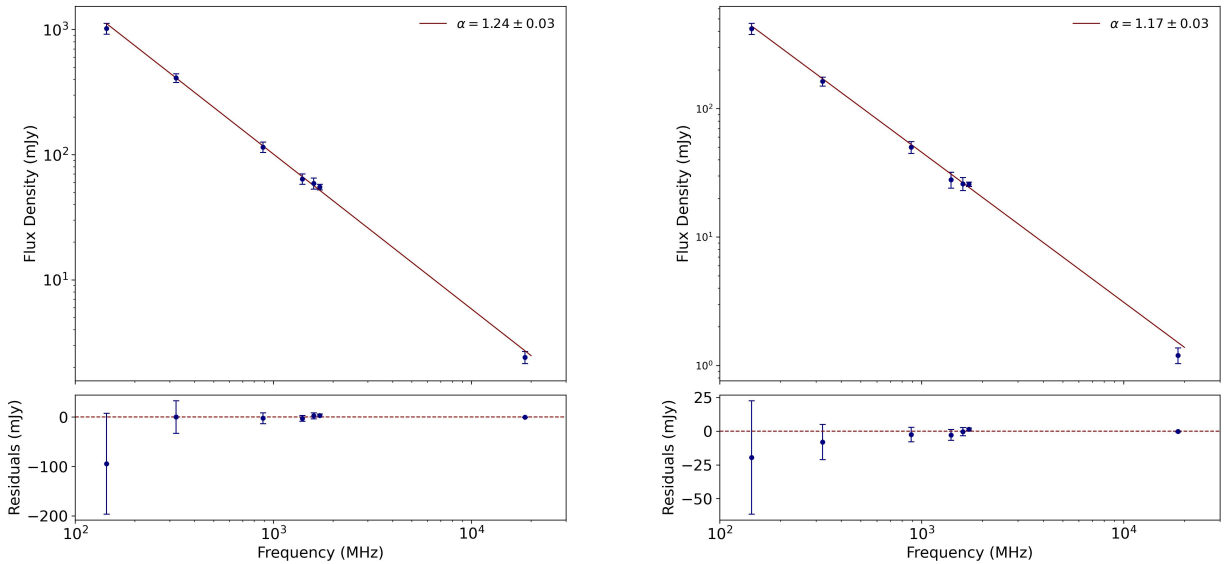
Figure 30. Integrated spectrum for the northern (left) and southern (right) relics, with the LOFAR integrated flux corrected for a factor of 1.5 to account for the behavior of the flux density of the point-like sources in the field.

Still, the flux estimate for the southern relic by the SRT appears consistent with being under-estimated, since it is detected just at 2σ, as already discussed.

In light of all these considerations, and considering that these last results are consistent with the spectral indices obtained not considering the LOFAR data, in Figure 26, we choose to

take as final estimates of the spectral indices the ones reported in Figure 30:

$$\alpha_{\mathrm{NE}} = 1.24 \pm 0.03$$
$$\alpha_{\mathrm{SW}} = 1.17 \pm 0.03$$

The power-law behavior of the two relics is consistent with what has been reported in the literature. Spectral indices are slightly steeper than those estimated by van Weeren et al. [130], but compatible with those found by Bonafede et al. [13], estimated to be 1.21±0.06 and 1.12±0.07 for the NE and SW relics respectively, with compatibility of 0.4 and 0.6 respectively [4]. This is compatible with predictions from diffusive shock acceleration theory [41] and aligns with the standard scenario for relic formation.

Conversely, within the framework of the re-acceleration scenario, the absence of a spectral break at high frequencies would imply that the finite-size cloud of fossil electrons is very large and distributed homogeneously. As a result, its effect is not visible in the integrated spectrum of the relic.

6.3 Mach numbers

According to the DSA theory in the test-particle regime, and assuming a constant shock strength and cosmic-ray electron cooling in a homogeneous medium, the integrated spectral index is related to the Mach number by:

$$\mathcal{M} = \sqrt{\frac{\alpha_{\mathrm{int}} + 1}{\alpha_{\mathrm{int}} - 1}}, \tag{6.5}$$

where α_{int} is the integrated spectral index and $\mathcal{M}$ is the Mach number of the shock. Following this reasoning (put more about why this is legit, literature), the resulting Mach number estimated is:[5]

$$\mathcal{M}_{\mathrm{NE}} = 2.9 \pm\ 0.8$$
$$\mathcal{M}_{\mathrm{SW}} = 3.4 \pm\ 2\ .$$

These numbers are in accord with the DSA theory, that predics that for strong shocks ($\mathcal{M} \to \infty$), the asymptotic behavior of the spectral index is $\alpha \to 1$ (and $\alpha_{\mathrm{inj}} \to 0.5$), while for weak shocks ($\mathcal{M} \lesssim 3-5$) it is $\alpha > 1$ (and $\alpha_{\mathrm{inj}} > 0.5$).

As highlighted by previous studies (e.g. van Weeren et al. [132]), deriving the Mach number from the integrated spectral index can lead to significant errors in some cases. Indeed, the formula in equation 6.5 has been derived under the assumption that the properties of the shock and the downstream gas remain constant during the electron cooling.

Recent cosmological simulations of radio relics by Wittor et al. [140] have shown that both the Mach number and the magnetic field are not uniform across the shock front. Furthermore, they showed that the downstream magnetic field is by far not constant. By comparing

---

[4]The compatibility between 2 measurements $x_1 \pm \sigma_1$ and $x_2 \pm \sigma_2$ is defined as $\lambda = \frac{|x_1 - x_2|}{\sigma_1^2 + \sigma_2^2}$. For $\lambda < 1$ the measurements are very compatible, for $1 < \lambda < 2$ tstill indicates an acceptable compatibility, $\lambda > 3$ shows significant discrepancy.

[5]The relatively large uncertainties on the Mach numbers arise from the propagation of the errors associated with the spectral index values.

spectral index measurements from observations and simulation, Rajpurohit et al. [106] argued that the spectral index derived from radio data is most-likely biased by the high value tail of the underlying Mach number distribution.

A better way to estimate the Mach number is to evaluate it from the injected spectral index, measuring this quantity in the injection region from images at very high-resolution or from the color-color diagram in case of projection effect.

6.4 Detection of the SZ effect

The Sunyaev-Zel'dovich Effect can be observed at frequencies as low as a few tenths of a GHz, capturing the beginning of the flux decrement caused by CMB photons being scattered to higher-energy parts of the spectrum by relativistic electrons in the intracluster medium (see Section 2.2 for more details).
In light of this, we carried on the following analysis, aimed to investigate the decrement that the SRT observations revealed to be sensitive enough to detect, leading to the first measurement of the SZ effect at these frequencies.

The detected intensity decrement on the SRT image due to the SZ effect is reported in Figure 31. Each point represents the average flux density measured within concentric annuli centered on the cluster[6], after blanking the detected sources.
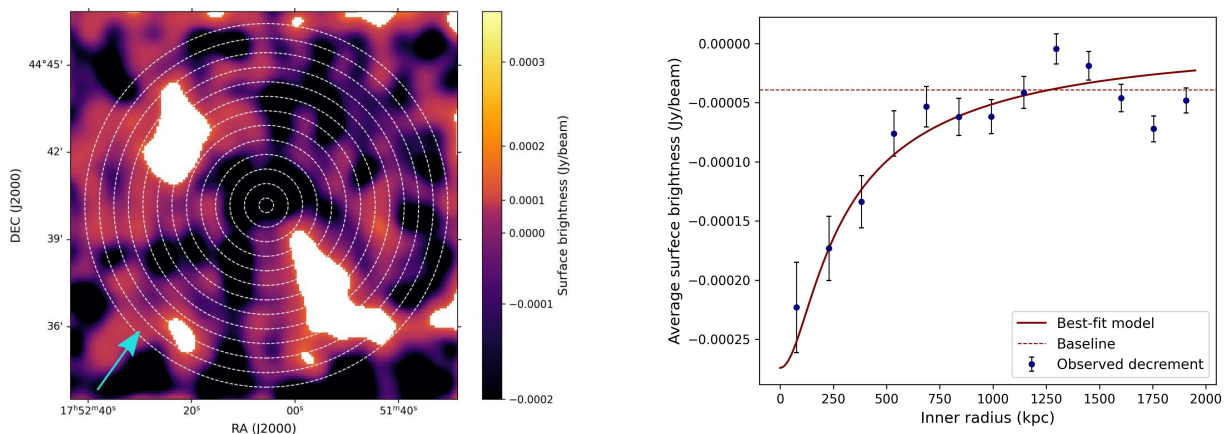
Figure 31. *Left:* Map of the observed flux decrement in the cluster center from SRT data at 18.6 GHz. To obtain the profile reported on the right, the sources were blanked, and annuli were traced around the center of the cluster. The blue arrow highlights a localized excess of flux density in the south-eastern region of the cluster. *Right:* In blue the observed average flux on annuli around the center of the cluster. The dashed line delineates the baseline to correct the surface brightness of the relics for, knowing the SZ effect is referred to a zero level of the flux. The continuous line shows the fit of the SZ decrement referred to the models from equation 2.46 and 2.45.

The observed decrement was compared with a model for the real decrement from equation 2.46:

---

[6]The cluster center was defined using the position of the most significant SZ decrement. It should be noted, however, that this position often differs from the center inferred from X-ray observations, particularly in merging galaxy clusters such as this one.

$$\left(\frac{\Delta I_{SZ}}{\text{mJy/beam}}\right) = \frac{1}{340}\left(\frac{\nu}{\text{GHz}}\right)^2\left(\frac{\Delta T_{\text{RJ}}}{\text{mK}}\right)\left(\frac{\Omega_{\text{beam}}}{\text{arcmin}^2}\right)$$

with ΔT_{RJ}=-2·y · T_{CMB} and y-parameter from equation 2.43:

$$y = \int n_e(r)\sigma_T \frac{k_B T_e(r)}{m_e c^2}\, dl.$$

The electron density has been assumed to follow a simple β-model, described by equation 2.45:

$$n_e(r) = n_0\left(1 + \frac{r^2}{r_c^2}\right)^{-3\beta/2},$$

A best-fit set of parameters was obtained using a Markov Chain Monte Carlo (MCMC) approach, using the emcce sampler [48], to retrieve the parameters n_0, r_c and β. The analysis assumes an isothermal model with fixed cluster temperature $k_B T_e$ of 5.9 keV, as estimated by Finner et al. [46]. The retrieved parameters are reported in Table 4, with posterior probability distribution showed in the corner plot in Figure 33.

No estimates of these parameters are currently available from X-ray data. This underscores the importance of using the SZ decrement as a complementary probe to derive physical properties of galaxy clusters.

Parameter	Median	$-\sigma$	σ
r_c [kpc]	160	-30	$+30$
log n_0 [cm^{-3}]	-2.6	-0.1	$+0.1$
β	0.6	-0.1	$+0.1$

Table 4. Retrieved β-model parameters from MCMC sampling. Quoted values are medians with 16th and 84th percentile uncertainties.

The modeled decrement is reported on the right of Figure 31.
An interesting feature of the plot in Figure 31 is the bump between $\sim$1200 and 1600 kpc. The bump is due to an increment of the flux density in the south east region of the cluster (pointed out by the blue arrow on the left panel of Figure 31), a feature to take into account and investigate in future SZ observations of MACS J1752+4440.

The average componization parameter estimated from the retrieval, obtained inverting equation 2.46, is, averaging inside a radius of 3':

$$y_{SRT}^{0.9'} = (2.6 \pm 0.3) \cdot 10^{-5} \tag{6.6}$$

Convolving SRT data with the Planck beam of 7', the value becomes $y_{SRT}^{7'}$=1.9($\pm$0.2)·10^{-5}, that is not consistent with the estimate from the Compton y map from [102] of y_{Plank}=4($\pm$1)·10^{-6}.
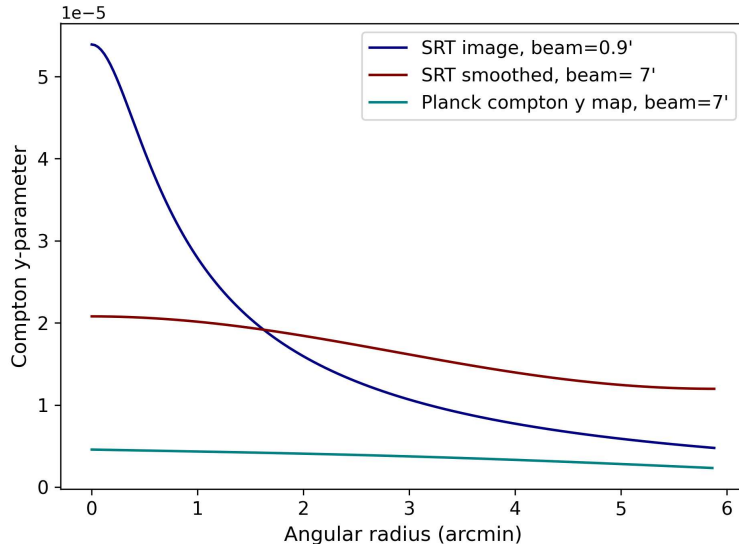
Figure 32. Different profiles of the y parameter: the blue line reports the profile detected from the SRT image. The red line represents the SRT profile convoluted with the Planck beam of 7'. The Planck profile is reported in teal.

Surely a factor to consider when looking at Planck data is the low resolution of the images, and the possible contamination from the field. A value of the Compton parameter of the order of 10^{-5} is more compatible with a cluster with the mass of MACS J1752+4440 than the 10^{-6} estimated by Planck (see Andreon and Radovich [3] for more details on Compton-y parameter-mass relations in galaxy clusters).

On the other hand, considering instead the derivation of the y-parameter from the modeling of the cluster, one must take into account the fragility of the assumption of a simplified β-model for the density of the cluster: MACS J1752+4440 is in fact a merging cluster, as confirmed by the images from XMM Newton reported on the left of Figure 34, and as such, a spherical model describing the density is a noticeable approximation. Puy et al. [105] claim that not considering the influence of the shape and the finite extension of a cluster, as well as of a polytropic thermal profile on the Compton parameter, can induce errors up to 30% in the various parameters calculated. Since the hot gas in a real cluster has a finite extension, each of the observed quantities of the Compton parameter and X-ray surface brightness will be smaller than that estimated based on the assumption that $l \to \infty$. The net effect when one considers infinite clusters is thus to overestimate the value of the temperature decrement and the X-ray surface brightness. Assuming an isothermal instead of a polytropic profile for the temperature has the same effect.
This is compatible with the fact that the obtained value of $y_{SRT}^{7'}$ from the modeling considered in this work is larger that y_{Planck} obtained from Planck observations.

Nevertheless, it is interesting to have an order of magnitude of the physical parameters involved, and to see that said parameters are consistent with expectations for a massive merging cluster like MACS J1752+4440.
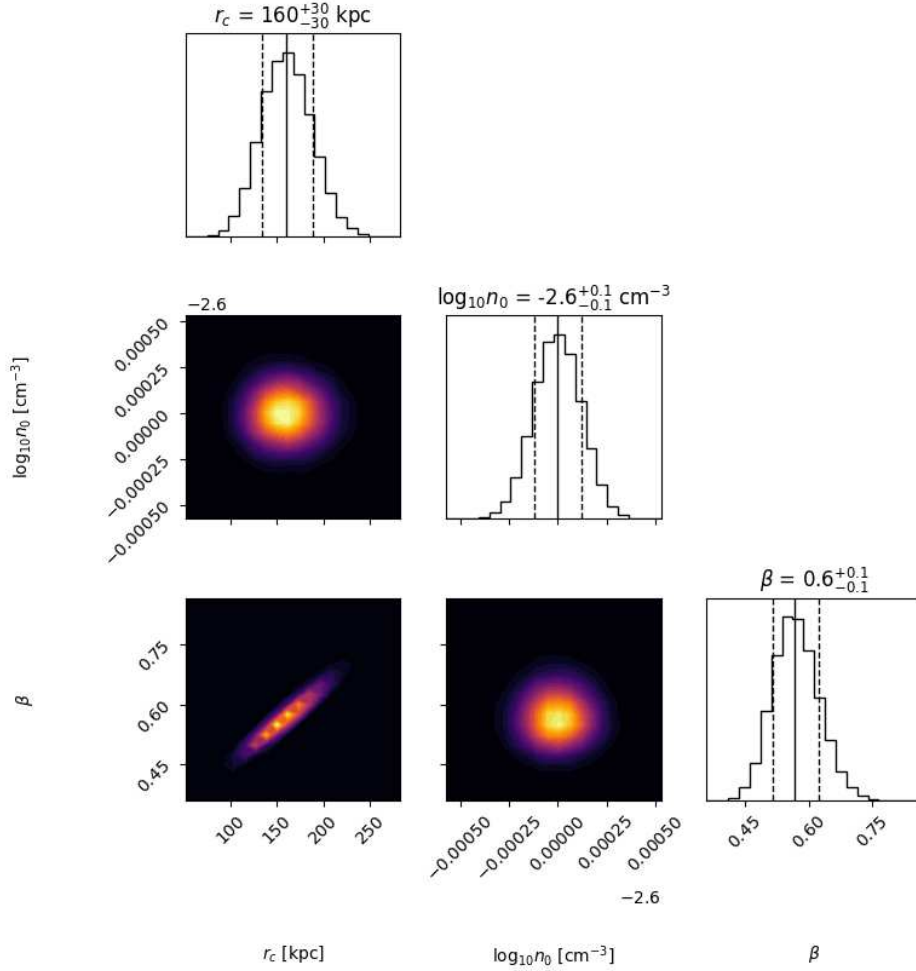
Figure 33. Retrieval of parameters for density profile using emcee. The continuous line represents the median of the distribution, the dashed lines the 16th and 84th percentile.

Considering the parameters obtained from the Bayesian retrieval, a simulated model of the X-ray surface brightness has been realized, adopting the model for the brightness:

$$b_X(\theta) = b_{X0} \left(1 + \frac{\theta^2}{\theta_c^2}\right)^{\frac{1}{2} - 3\beta} \tag{6.7}$$

with

$$b_{X0} = \frac{1}{4\pi(1+z)^3} \sqrt{\pi} \, n_{e0}^2 \, \Lambda(E, T_e) \, r_c \frac{\Gamma(3\beta - \frac{1}{2})}{\Gamma(3\beta)} \tag{6.8}$$

as derived by Birkinshaw [8]. Considering a simmetrically spherical model with multiple components indicating the 2 elements of a merging process, the nucleus and a diffuse emission around, the results are the ones reported in Figure 34. It should be noted that the simulation shown in the figure is strictly qualitative and is included to illustrate the plausibility of the parameters obtained through the Bayesian retrieval.
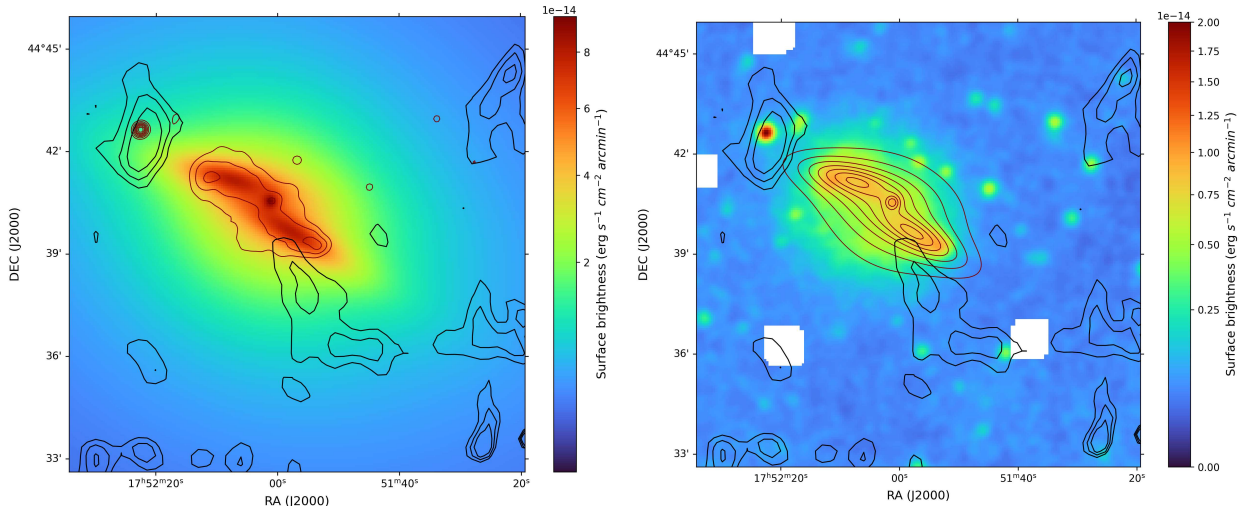
Figure 34. *Left:* Simulated model of surface brightness of MACS J1752+4440, with SRT radio contours at 1,2,3σ in black and X-ray XMM contours in maroon. *Right:* XMM X-ray image with SRT radio contours at 1,2,3σ in black and X-ray model contours in maroon.

It is immediately evident that the surface brightness predicted by the model differs significantly from the observed X-ray emission. Several factors could account for this discrepancy. First, the model does not account for the telescope's instrumental response, which could result in a significant underestimation of the simulated observed brightness. Additionally, as already stated, the assumption of spherical symmetry is an approximation; the merging system might be less extended along the line of sight than it appears in projection, leading to an overestimation of the emitting volume. Finally, the model does not consider the presence of diffuse emission components that may be spatially separated from the main X-ray–emitting region.

Considering all these factors, the parameters obtained from the retrieval fitting the SZ decrement appear reasonable, and the model provides a qualitatively good reference for interpreting the observations.

Follow-up observations extending to 90 GHz (e.g., with MISTRAL[7]) will be crucial for detecting the Sunyaev-Zel'dovich effect at frequencies where the decrement is strongest, enabling an improved fit to extract the physical properties of the cluster.

---

[7]MIllimetric Sardinia radio Telescope Receiver based on Array of Lumped elements KIDs, [98]

7

Polarization and magnetic field estimates

This chapter presents the results of the polarimetric analysis carried out using SRT and JVLA data. The JVLA analysis includes results from rotation measure synthesis to take into account the Faraday effect. The chapter concludes with magnetic field estimates that incorporate the various findings from this work.

The theory behind polarization and the mathematical framework assumed for calculations are reported in Appendix A.

7.1 SRT data

All of the information on the polarization properties of relics are usually mainly collected in the frequency range of 1-8.3 GHz. Since the Faraday rotation is expected to be almost negligible at 18.6 GHz, the intrinsic polarization of the relic can be directly mapped for the first time by these observations.

Through the procedure described in Section 5.1.2, images for the Stokes parameter U and Q are produced. Fractional polarization and polarization angle images are then obtained as described in Appendix A, with results reported in Figure 35.
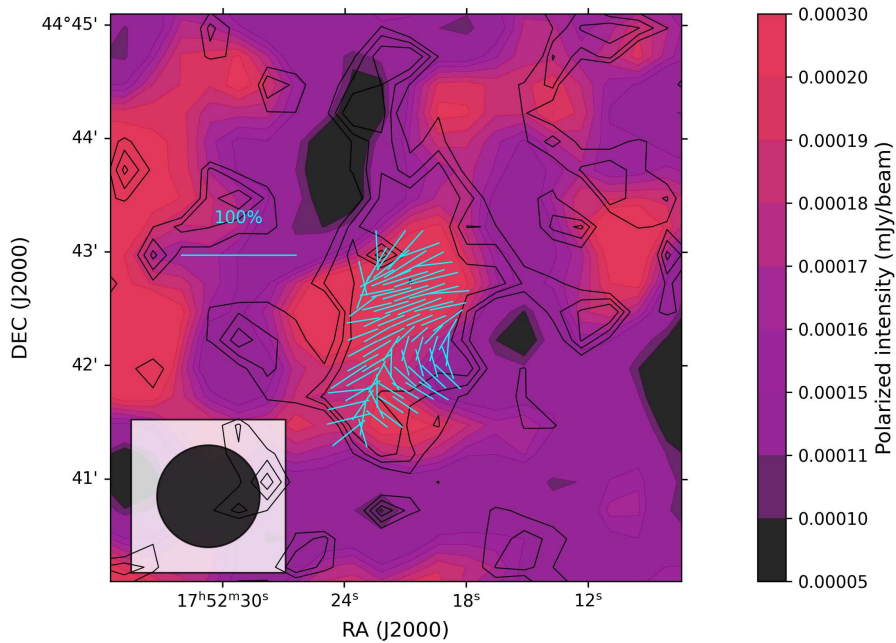
Figure 35. Polarization image from SRT data at 18.6 GHz, beam of 0.9', with polarization vectors overlaid. The vectors have length proportional to fractional polarization, and are oriented according to the polarization angle, along the **E** field of the detected emission. The cut on the vectors shown is a cut that takes into account the fact that the fractional polarization has to have physical values between 0 and 1, and the polarization has to be detected at least at a σ level with σ=0.2 mJy/beam. This assured that only the less noisy regions are considered. Black contours are at 1, 2, 3 σ of the total intensity image.
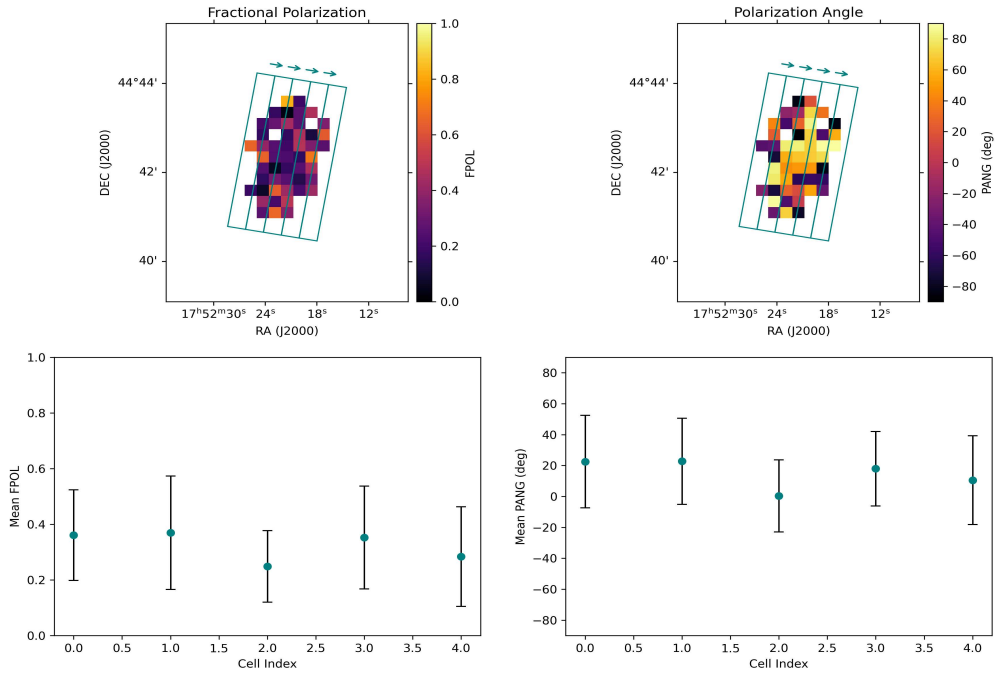
Figure 36. Statistics for fractional polarization and polarization angle moving across the relic. The mean fractional polarization is 32 ± 2 %, the polarization angle 14 ± 4 degrees.
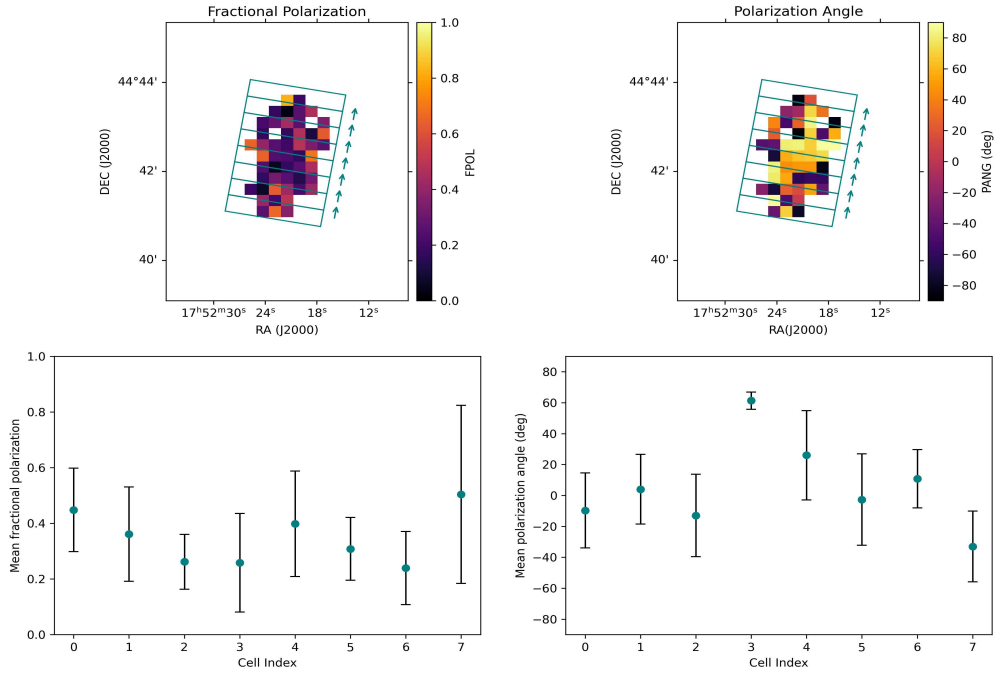
Figure 37. Statistics for fractional polarization and polarization angle moving along the relic. The mean fractional polarization is 35 ± 3 %, the polarization angle 8 ± 7 degrees.

Figure 35 shows the results for the polarization of just the northern relic, since the southern relic was not detected with sufficient sensitivity. The images display vectors whose lengths are proportional to the fractional polarization and whose orientations are determined by the polarization angle (PANG) [8]. The errors on the polarization angles range from 10 to 20 degrees.

The statistics for fractional polarization and polarization angles across and along the relic are reported in Figures 36 and 37. Only the pixels with physical values (from 0 to 1 for the fractional polarization) and signal to noise ratio on the polarized image at least 3 are considered for the statistical analysis. The high errors on the polarization angle are due to the high variability of this quantity, especially along the longer axis of the relic. More details on the polarization angle and its interpretation are discussed in Section 7.2.

The average fractional polarization for the NE relic is of 33 ± 4 %, with peaks of 60% in the external regions.
Visually, only the magnetic field lines at 90 degrees from the line-of-sight are observed, while we are blind to the other magnetic fields components, since the resulting E-vectors are not propagating towards us.

The E-field vectors in the central part of the relic are aligned perpendicular to the relic filaments, as it is expected in case of a shock wave, if compression of small-scale magnetic fields is responsible for the high degree of polarization typical of relics.
At the borders of the relic, vectors seem to follow a more chaotic structure. Indeed, state-of-the-art numerical simulations [140] have shown that the magnetic field topology across radio relics is more complex than traditionally assumed: its orientation varies significantly along the relic, with both parallel and perpendicular alignments to the shock present. The large correlation length ($\sim$250 kpc) found in simulations suggests the presence of coherent magnetic structures on cluster scales, while local variations dominate the observed emission morphology of radio relics. In these models, the polarized emission traces the underlying magnetic field structure, with the correlation length limited to regions of a few hundred kpc. Indeed, the magnetic field in the vicinity of the shock front is expected to be altered in both strength and direction by the shock itself, and therefore does not necessarily represent the properties of the field across the cluster. Similar complex patterns appear to emerge from our data, which resolve structures on scales up to $\sim$200 kpc.

7.2   JVLA data

Figure 38 shows the results of the polarimetric analysis performed on the JVLA data. The electric field vectors are shown where the polarized intensity exceeds 4σ. The vectors have length proportional to the fractional polarization and orientation of the polarization angle. The contours represent the 3σ level of the total intensity, with the aim to highlight which regions of the relic are more polarized.
The mean fractional polarization for the northern relic is of 31 ± 3 %, while for the southern relic is 35 ± 3 %. For both relics, peaks around $\sim$50% are reached in the peripheral regions of the structures.

---

[8]As defined in appendix A, the polarization P and polarization angle χ are obtained as $P = \sqrt{Q^2 + U^2}$ and $\chi = \frac{1}{2}tg^{-1}(\frac{U}{Q})$.

The polarization vectors show directions that differ from those detected in the SRT data. This noticeable discrepancy motivates the rotation measure synthesis presented in Section 7.2.1.

On the other hand, the fractional polarization of the northern relic is consistent with that obtained at 18.6 GHz, suggesting that depolarization is minimal. This implies that the Faraday rotation across the region encompassing the relic is relatively uniform.

Next section reports the process conducted to obtain the Faraday depth of the different regions of the relic and de-rotate the vectors of polarization accordingly.
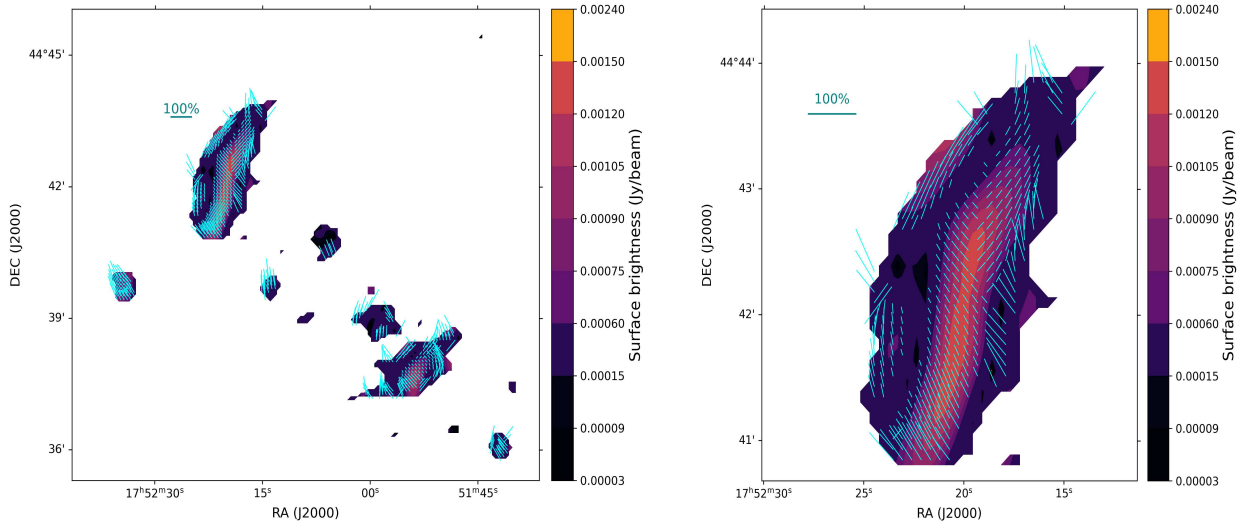
Figure 38. *Left:* Polarization image from JVLA data at frequencies from 1.19 to 2.19 GHz, beam of 25.0" x 22.3". The vectors are oriented along the **E** field of the detected emission, with length proportional to the computed fractional polarization. *Right:* Zoom on the northern relic for better comparison with detected polarization from SRT data.

7.2.1   Rotation Measure synthesis

JVLA data are expected to be affected by bandwidth depolarization due to the Faraday effect: due to birefringence of the magneto-ionic medium, the polarization angle of linearly polarized radiation that propagates through the plasma is rotated as a function of frequency, and this is something that is seen when large frequency bands are used for observations (see Section 2.1.3 for more details).

The RM synthesis is implemented to solve this problem of bandwidth depolarization and sum coherently the polarization vectors from the observed sources across the observed frequency range.

Let's first define the fundamental quantities this method relies on.

The complex polarized surface brightness per unit Faraday depth is defined through:

$$P(\lambda^2) = \int_{-\infty}^{+\infty} F(\phi) \, e^{2i\phi\lambda^2} \, d\phi \tag{7.1}$$

where $F(\phi)$ is the Faraday dispersion function. P is the polarized intensity of the source, that can be written as:

$$P = Q + iU \tag{7.2}$$

The aim of RM synthesis is to recover the Faraday dispersion function $F(\phi)$ from the observed complex polarization $P(\lambda^2)$, measured across a range of wavelengths. The results

are used to obtain the intrinsic polarization angle of the radiation and, therefore, the characteristics of the magnetic field of the source.

The cubes we considered are Stokes U and Q cubes of 150 channels, with each channel of 5 MHz width, from 1.19 to 1.96 GHz.

With this frequency setting, the maximum Faraday depth to which we have more than 50% sensitivity is determined by the channel width in wavelength-squared space, $\delta\lambda^2$, and is given by:

$$|\phi_{\max}| \approx \frac{\sqrt{3}}{\delta\lambda^2} \approx 2000 \text{ rad m}^{-2} \tag{7.3}$$

The resolution in Faraday depth space is set by the total range of wavelength-squared values, $\Delta\lambda^2$, with the full-width at half-maximum given by:

$$\delta\phi \approx \frac{2\sqrt{3}}{\Delta\lambda^2} \approx 86 \text{ rad m}^{-2} \tag{7.4}$$

The largest scale in Faraday space to which the observation is sensitive (i.e., the maximum Faraday structure size that can be resolved) is set by the shortest observed wavelength $\lambda_{\min}$, and is given by:

$$\text{Maximum scale} \approx \frac{\pi}{\lambda_{\min}^2} \approx 130 \text{ rad m}^{-2} \tag{7.5}$$

The RM synthesis process was carried on with RM-Tools [104], a software that analyzes radio polarization data, specifically the use of Faraday rotation measure synthesis and Stokes QU model fitting.
RM-Tools takes as input the cubes for stokes Q and U, chooses a random ϕ and calculates:

$$P'(\lambda^2) = Q(\lambda^2) + iU(\lambda^2)e^{-2i\phi(\lambda^2 - \lambda_0^2)} \tag{7.6}$$

and sums across all wavelengths (or frequencies):

$$F(\phi) = \sum_{\lambda^2} w(\lambda^2)P'(\lambda^2) \tag{7.7}$$

where $w(\lambda^2)$ is a window function that takes into account the sampling in λ^2 space.
Ranging across all predefined ϕ, the software builds a cube for F(ϕ), and then selects the maximum Faraday depth for each pixel of the polarized image to produce. This maximum occurs in the Faraday channel where the polarization vectors add most coherently. For every pixel the situation is the one illustrated on the upper left of Figure 39. The software produces an image with the peak of the Faraday spectrum pixel by pixel, and one with the position of the peak, that corresponds to the Rotation Measure for a specific portion of the image.

Figure 39 shows the results obtained for a RM sampled between -1000 and 1000 rad/m^2, with steps of 6 rad/m^2. The RM values vary as reported in Figure 40. Most of the northern relic is dominated by two large patches with values around -50 and 30 rad/m².
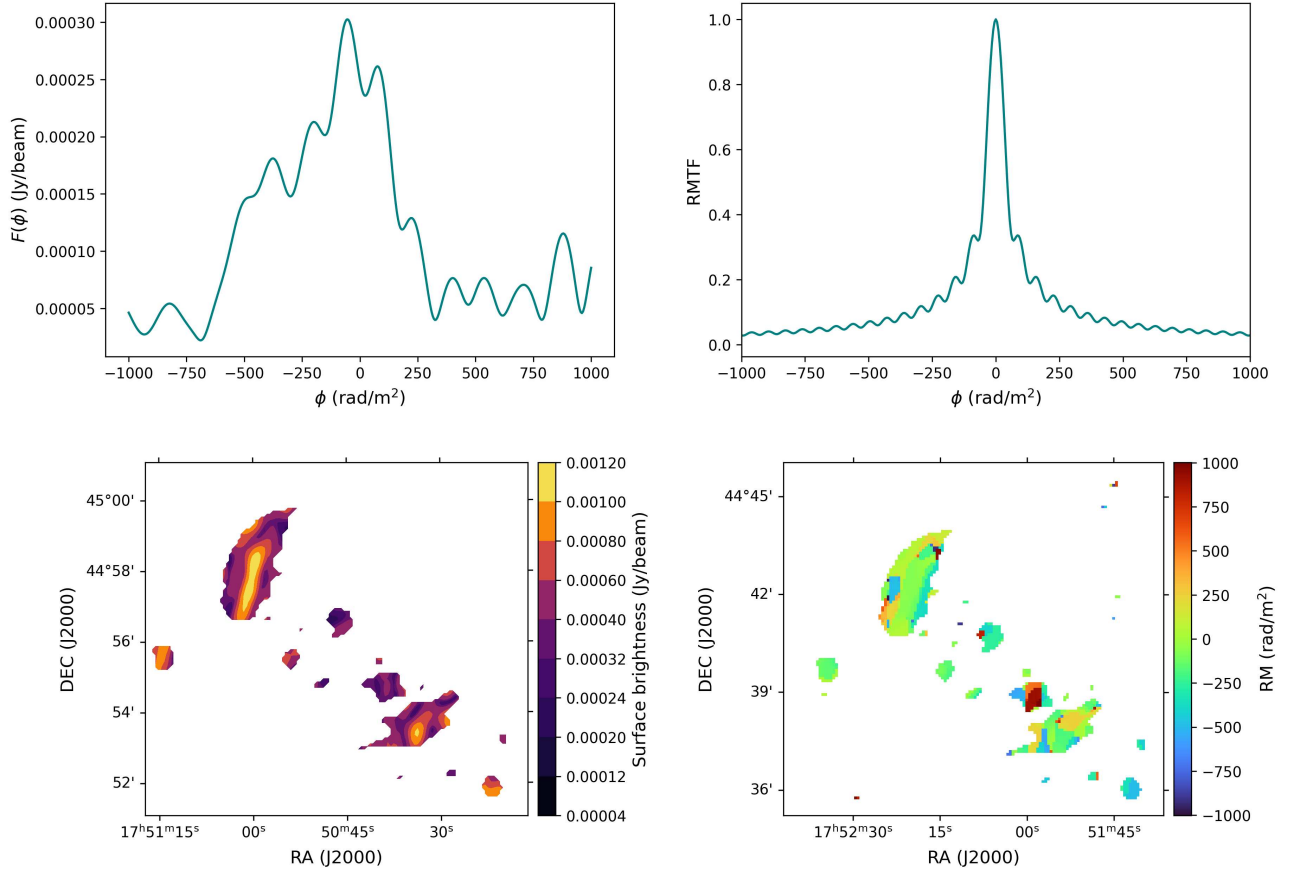
Figure 39. *Upper left:* Example of spectrum F(ϕ) for one pixel inside the northern relic. The peak of the spectrum is selected for every pixel, and the corresponding ϕ is associated to the RM of the peak. *Upper right:* Rotation measure transfer function, corresponding to the Fourier transform of the sampling function in λ^2 space. *Bottom left:* Image showing the polarized intensity corresponding to the peak of the Faraday spectrum corresponding to each pixel (as shown in the top left panel as an example). *Bottom right:* Rotation measure map used to de-rotate the polarization angle of the light from the sources.
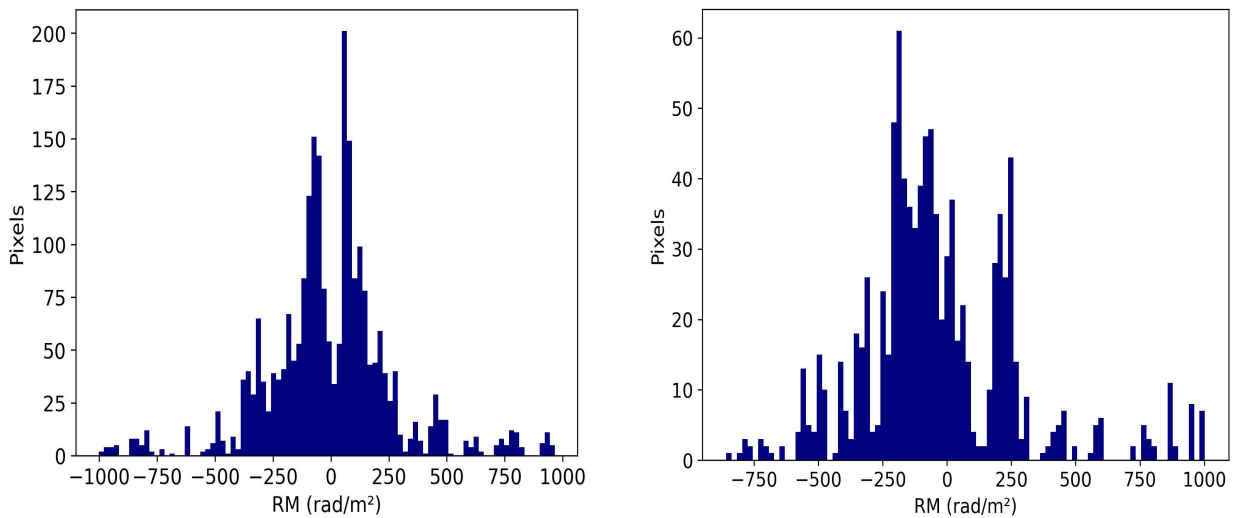
Figure 40. RM values distribution for the northern (left) and southern relics (right).

The maximum polarization image (i.e. the polarization intensity image corresponding to the peak in Faraday depth, in the bottom left of Figure 39) obtained takes into account also a bias factor that has been subtracted, estimated by averaging the background noise from Stokes U and Q images and applying the formula from George et al. [49]:

$$P_{debias} = \sqrt{P^2 - 2.3\sigma_{QU}^2} \qquad (7.8)$$

The obtained RM shown in Figure 39 is applied to equation 2.36 to de-rotate the polarization vectors and obtain the final images reported in Figure 41. The cut of the images is obtained by considering signal to noise ratio above 4, taking as a reference the noise σ_{QU}. The mean fractional polarization after the RM synthesis is of 35±3 % for the NE relic, still consistent with SRT results, and of 41±4 % for the SW relic.

The vectors for the northern relic show a general orientation perpendicular to the major axis of the source, as it is seen from SRT data. Vectors become parallel to the relic at the periphery and in the southernmost regions of the structure, where the field appears to be more turbulent. This is in accordance with what found by SRT data, and it seems to be ulterior proof of the complexity of the magnetic field in these structures, as reported in Section 7.1.

Since the pattern of the electric field vectors seems to reproduce the one obtained by SRT data, we are lead to the conclusion that the RM synthesis process shows sensible results in our case.
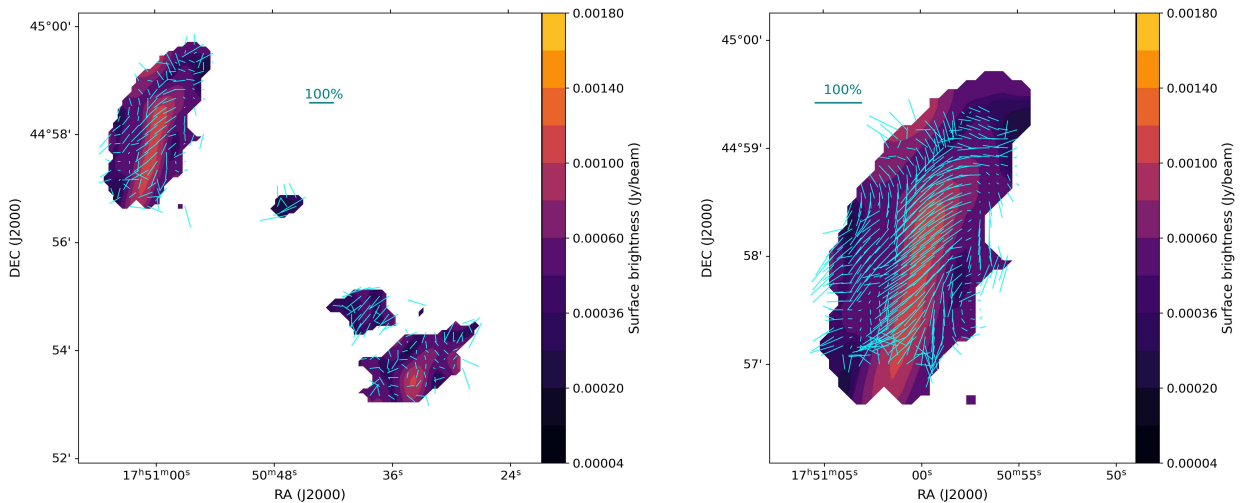
Figure 41. *Left:* Polarization image from JVLA data at 1.6 GHz, beam of 25.0" x 22.3". The vectors are oriented along the **E** field of the detected emission, accounting for Faraday rotation, with length proportional to the computed fractional polarization. *Right:* Zoom on the northern relic for better comparison with detected polarization from SRT data, accounting for Faraday rotation.

7.3 Magnetic field estimates

There are multiple approaches to estimate the magnetic field strength based on the analyses presented thus far. All results in this section aim to provide a rough estimate of the magnetic field's order of magnitude in the region of the relics, and to assess whether the inferred values are physically plausible for magnetic fields in galaxy clusters.

1) THERMAL AND MAGNETIC PRESSURE

The first option we present involves the use of the thermal pressure from X-ray data and assuming that part of it is balanced by magnetic pressure:

$$\frac{B^2}{8\pi} = \alpha P_{\text{th}} = \alpha\, n_e\, k_B\, T_e \quad \Rightarrow \quad B = \sqrt{8\pi\, \alpha\, n_e\, k_B\, T_e}$$

where $\alpha \in [0.01, 1]$ is the magnetic-to-thermal pressure fraction (with $\alpha = 1$ corresponding to equipartition). Considering the value of n_e at the radius of the relics from the center (around 3.5 arcminutes) and the temperature calculated by Finner et al. [46] and adopted for the modeling in Section 6.4, we obtain a magnetic field of 9 μG for $\alpha{=}1$ and 1 μG for $\alpha{=}0.01$.

While this estimate provides an upper limit on the magnetic field strength under equipartition, it relies on the assumption of static pressure balance between thermal and magnetic components. This condition is a strong simplification, especially in the context of merging galaxy clusters as the one this thesis focuses on, where the intracluster medium is highly disturbed, turbulent, and far from hydrostatic equilibrium. Moreover, this approach does not account for spatial variations in magnetic field structure, projection effects, or pressure anisotropies introduced by shocks and bulk flows. As such, while useful for a first-order approximation, this has to be considered as primarily used to provide bounds rather than precise measurements.

2) EQUIPARTITION THEOREM

Another option to obtain a magnetic field estimate is to use the equipartition theorem, following the computations by Govoni et al. [56], reported in Section 2.1.1, from which the equipartition magnetic field results:

$$B_{\text{eq}} = \left(\frac{24\pi}{7} u_{\text{min}} \right)^{1/2}$$

with

$$u_{\text{min}} \left[\frac{\text{erg}}{\text{cm}^3} \right] = \xi(\alpha, \nu_1, \nu_2)(1{+}k)^{4/7}\, (\nu_0\, [\text{MHz}])^{4\alpha/7}\, (1{+}z)^{(12+4\alpha)/7} \left(I_0 \left[\frac{\text{mJy}}{\text{arcsec}^2} \right] \right)^{4/7} (d\, [\text{kpc}])^{-4/7}$$

where z is the source redshift, I_0 is the source brightness at frequency ν_0, d is the source depth along the line of sight, $\xi(\alpha, \nu_1, \nu_2)$ is a constant that depends on the spectral index and frequency range (tabulated in [56]). The values of magnetic field varying the parameters are reported in tables 5 and 6. The value of k, ratio of the energy in relativistic protons to that in electrons, depends on the mechanism of generation of relativistic electrons, which is so far poorly known. Uncertainties are also related to the volume filling factor ϕ. Values usually assumed in literature for clusters are $k = 1$ (or $k = 0$) and $\phi = 1$. Another parameter difficult to infer is the extent of the source along the line of sight d, assumed for our estimates to be between 500 and 800 kpc for the NE relic, and between 200 and 500 kpc for the SW relic.

The value of ξ is taken from Table 1 from Govoni et al. [56], assumed to be $3.43 \cdot 10^{-13}$ for spectral index values around 1.2 .

k	d [kpc]	B [µG]
0	500	8.7
0	800	7.6
1	500	10
1	800	9.2

k	d [kpc]	B [µG]
0	200	8.9
0	500	6.9
1	200	11
1	200	8.4

Table 5. Magnetic field strength B [µG] for different values of k and d for the northern relic (left) and the southern relic (right), from JVLA data.

k	d [kpc]	B [µG]
0	500	4.5
0	800	3.9
1	500	5.5
1	800	4.8

k	d [kpc]	B [µG]
0	200	4.8
0	500	3.6
1	200	5.8
1	500	4.5

Table 6. Magnetic field strength B [µG] for different values of k and d for the northern relic (left) and the southern relic (right), from SRT data.

3) RM MODELING

One fundamental method relies on the definition of the rotation measure, which relates the observed Faraday rotation to the properties of the magnetized intracluster medium, as per equation 2.38:

$$\mathrm{RM}\left[\frac{\mathrm{rad}}{\mathrm{m}^2}\right] = 812 \int_0^L n_e \left[\mathrm{cm}^{-3}\right] B_\parallel \left[\mu\mathrm{G}\right] \, dl \left[\mathrm{kpc}\right],$$

where n_e is the electron density, $B_\parallel$ is the line-of-sight component of the magnetic field, and the integration is performed along the path length L through the cluster.

Inverting equation 2.38 requires a detailed knowledge of the thermal plasma density distribution and advanced numerical techniques that can explore different magnetic field models and find the best parametrization (see e.g. Murgia et al. [86], Govoni et al. [53]).

In the context of this thesis we decided instead to start evaluating the magnetic field strength with a simple approach.
If we consider an external screen containing a gas with a constant density and a uniform magnetic field that produces a rotation of the polarization angle proportional to $\lambda^2 \langle RM \rangle$, we can provide an approximate estimate of the order of magnitude of the magnetic field in the relic region using the average RM value and the following formula [56]:

$$\langle \mathrm{RM} \rangle = 812 \, B_\parallel \, n_e \, L \quad \Rightarrow \quad B_\parallel = \frac{\langle \mathrm{RM} \rangle}{812 \, n_e \, L} \tag{7.9}$$

We estimated an average RM of -80 rad/m^2 for the northern relic and -30 rad/m^2 for the southern relic in the regions defined at 3σ of the polarized intensity. This values have to be corrected for the galactic Faraday depth, estimated to be 37.65 ± 11.15 rad/m^2 [92], and shifted for the redshift (e.g. Amaral et al. [2]), according to :

$$RM_{int} = (RM_{obs} - RM_{gal})(1 + z)^2 \ .$$ (7.10)

Adopting the electron density estimated from the Bayesian retrieval described in Section 6.4 at the radius of the relics from the center (around 3.5 arcminutes), the magnetic field is found to vary from $B_{NE} \approx 1.4$ μG for L=500 kpc and $B_{NE} \approx 0.84$ μG for L=800 kpc for the northern relic, and $B_{SW} \approx 0.77$ μG for L=500 kpc and $B_{SW} \approx 1.9$ μG for L=200 kpc for the southern relic. The values of L have been chosen assuming an approximate spherical symmetry for the relics, and so a diameter corresponding to the projected distance in the sky, reported in Section 6.1.2.

In the simple scenario of random magnetic field directions in cells of size Λ_c (kpc), with uniform magnetic field strength and uniform electron density, the observed RM results from a random walk process. Due to the central limit theorem, the RM distribution is expected to follow a Gaussian with zero mean and a variance given by Murgia et al. [86]:

$$\sigma_{\mathrm{RM}}^2 = 812^2 \Lambda_c^2 \int (n_e B_{\parallel})^2 \, dl$$ (7.11)

where dl is the infinitesimal path length increment along the line of sight (LOS) in kpc, n_e is measured in cm^{-3} and $B_{\parallel}$ is the magnetic field strength parallel to the line of sight in μG. If one considers the RM scatter to determine the strength of the magnetic field, assuming the simple random walk scenario denoted by equation 7.11, the most rudimentary estimate of the line-of-sight magnetic field strength, as estimated by Osinga et al. [94], is given by:

$$\left(\frac{B_{\parallel}}{\mu G} \right) = 2.46 \left(\frac{\sigma_{\mathrm{RM}}}{200 \text{ rad m}^{-2}} \right) \left(\frac{n_e}{10^{-3} \text{ cm}^{-3}} \right)^{-1} \left(\frac{\Lambda_c}{10 \text{ kpc}} \right)^{-1/2} \left(\frac{L}{1000 \text{ kpc}} \right)^{-1/2}$$ (7.12)

where L indicates the line-of-sight column length.
We adopted $\sigma_{\mathrm{RM}} \approx 70$ rad m^{-2} in both the northern and southern relic regions, as estimated from the σ_{RM} profile reported in Figure 43 at the radius of distance of the relics from the cluster center. Using the electron density inferred from the Bayesian retrieval in Section 6.4, and assuming $\Lambda_c = 100$ kpc (the average dimension of the patches from the RM map), we estimate the magnetic field to be approximately $B_{\parallel} \approx 2.1$ μG for a line-of-sight depth $L = 100$ kpc. If we instead assume $L = 500$ kpc, the resulting magnetic field decreases to $B_{\parallel} \approx 0.95$ μG.

A more precise approach entails considering the observed RM dispersion profile extracted by the data reported in Figure 42 as a function of the distance from the cluster center, as shown in Figure 43. The profile of the rotation measure was obtained by averaging the absolute values of the RM map in annuli around the cluster center, using as weights the errors associated with the RM map [49]:

$$\sigma_{RMmap} = \frac{\sigma_{QU}}{maxPI} \frac{\sqrt{3}}{(\frac{c}{\nu_1})^2 - (\frac{c}{\nu_2})^2}$$ (7.13)

where c is the light speed, ν_1 and ν_2 are the first and last frequency of the observation bandwith (for the JVLA), $maxPI$ is the maxmum of F(ϕ), reported in Figure 41.
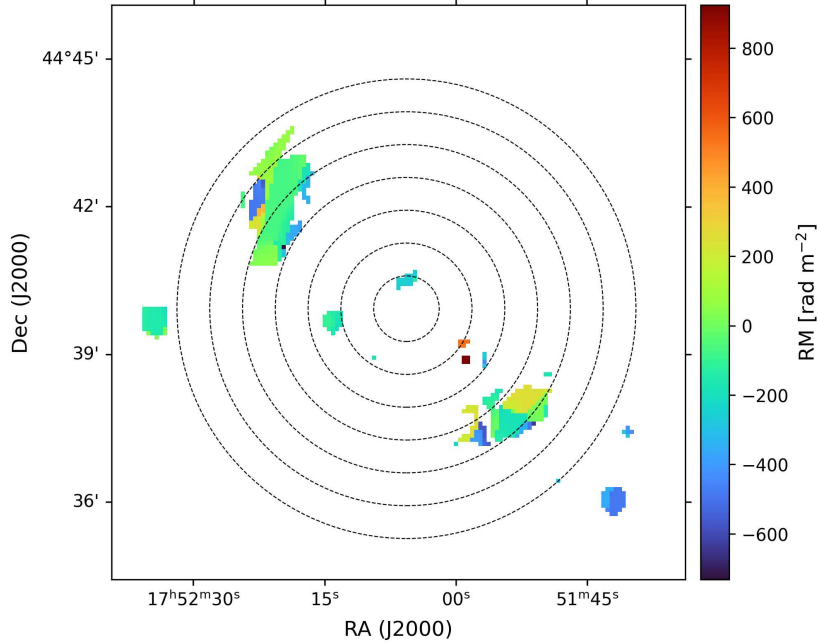
Figure 42. The image shows the rotation measure map and the annuli used for an evaluation of the RM profile. The center of the cluster was not considered, due to the absence of enough independent measurements. We can notice that relatively high error bars in the plots in Figure 43 are easily associated to a low number of independent measurements or to annuli where the radio galaxy just north-east of the southern relic, probably external to the cluster, is visible. The cut is performed considering regions detected at at least SNR$\gtrsim$ 3.

The RM dispersion was evaluated using a median absolute deviation estimate (a simple standard deviation was in this case not applicable, since the values do not follow a Gaussian distribution). Both the profiles show the characteristic random-walk behaviour expected from the fact that the cluster magnetic fields are thought to be generally turbulent and disordered.
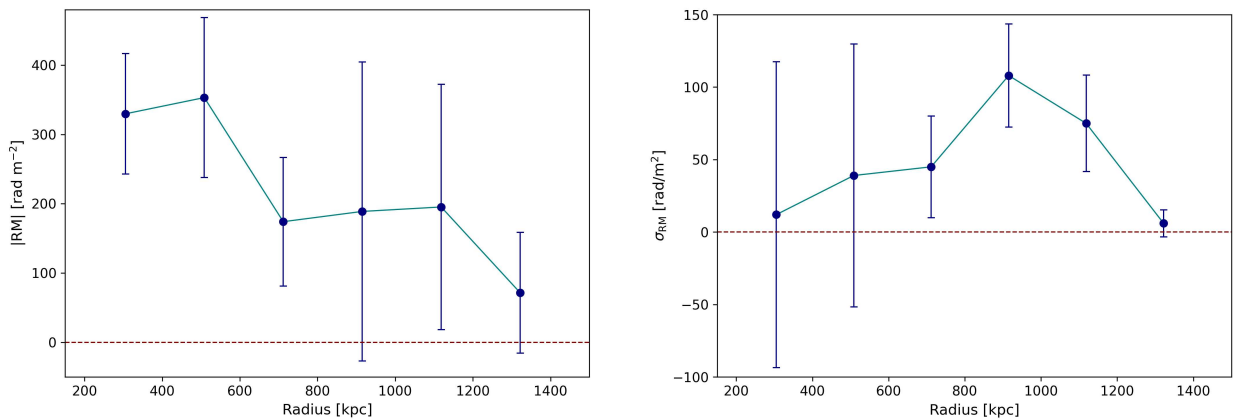
Figure 43. *Left:* Mean RM in annuli around the cluster center. *Right:* Dispersion of RM in annuli around the cluster center. Measures closer to the cluster center have been excluded since very small samples of RM measures durvived the SNR cut.

The RM profile appears to follow a decreasing trend with radius, while the dispersion remains significant. The relatively noisy profiles are likely due to the limited number of measurements that survive the 4σ polarization cut, leaving only a small sample of RM values available for this statistical analysis, as reported in Figure 43.

To estimate the magnetic field, the σ_{RM} profile was modeled following what Dolag et al. [33] derived, assuming a β-model for the thermal density and setting a model for the magnetic field structure. A commonly used model assumes a Gaussian random magnetic field with a power-law power spectrum [125]:

$$|B_k|^2 \propto k^{-n},\tag{7.14}$$

where k is the wave number and n is the slope of the power spectrum. The field fluctuates between a minimum spatial scale $\Lambda_{\min} = \frac{2\pi}{k_{\max}}$ and a maximum scale $\Lambda_{\max} = \frac{2\pi}{k_{\min}}$.
The normalization of this power spectrum is determined by assuming a radial dependence of the average magnetic field strength $\langle B(r)\rangle$, which follows the thermal gas density profile:

$$\langle B(r)\rangle = \langle B_0\rangle \left(\frac{n_e(r)}{n_0}\right)^{\eta},\tag{7.15}$$

where $\langle B_0\rangle$ and n_0 are the magnetic field strength and electron density at the cluster center, respectively, and η governs the radial scaling of the magnetic field with the gas density. Following this reasoning, Dolag et al. [33] derived:

$$\sigma_{\mathrm{RM}}(r) = K\, B_0^{1/2}\, \Lambda_c^{0.5}\, n_0\, r_c^{1/2} \left(1 + \frac{r^2}{r_c^2}\right)^{-\frac{6\beta(1+\eta)-1}{4}} \sqrt{\frac{\Gamma(3\beta(1+\eta)-0.5)}{\Gamma(3\beta(1+\eta))}}.\tag{7.16}$$

A modeling of this kind involves multiple assumptions. We performed a Bayesian retrieval fixing the values of n_0, r_c, β derived from the process described in Section 6.4, fixing the dimensions of the cell Λ_c to a standard value of 100 kpc, and assuming the constant K varying from 400 to 800. However, we do not show the results, since they shows too great a degeneracy between the parameters η and B_0 to be significative. Figure 44 shows some possible plots of the profile of σ_{RM}, at the varying of the parameters reported in the image. Higher or lower values of both B_0 and η lead to results highly incompatible with the data. The most compatible profile yields $B_0 \sim 2$ μG and η varying from 1 to 1.5 .
These large uncertainties are likely due to the fact that radio relics provide information on the magnetic field only locally, within regions where its properties are strongly modified by the passage of shock waves, and are therefore not representative of the cluster as a whole. By contrast, the radio galaxy included in this analysis (if external to the cluster as assumed) is not directly affected by such disturbances. Moreover, since only peripheral sources are being considered, the estimates become even more challenging to constrain.

In practice, we cannot draw very robust conclusions from these profiles: the σ_{RM} trend does not follow a clear monotonic decrease, and the limited number of independent RM measurements in the central regions prevents us from constraining the inner properties of the cluster. Moreover, the β-model employed to describe the electron density is an oversimplification, as merging clusters often exhibit irregular, multi-component gas distributions that deviate significantly from spherical symmetry.
Additionally, the RM profiles do not approach zero at the largest radii considered, as it is instead expected by this kind of modeling. This may arise from the presence of coherent

magnetic structures, such as those associated with radio relic shocks, which can bias the average RM value ⟨RM⟩ away from zero. Finally, numerical simulations (e.g., Osinga et al. 94) have shown that intracluster magnetic fields in merging systems can display turbulent and filamentary morphologies, producing RM profiles far more complex than those predicted by simple analytical models.
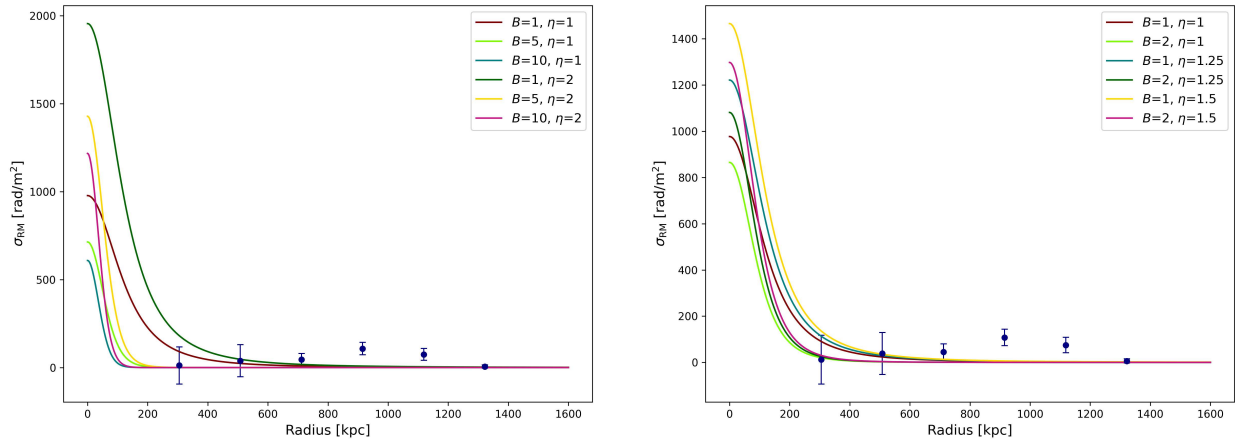
Figure 44. Modeling of σ_{RM} profile, assuming K=400, Λ_c=100 kpc.

More deep polarization data of sources distributed across all the cluster volume would be necessary to better constrain the magnetic field of MACS J1752+4440 based on an RM analysis. Comparisons with simulations can help determine the values of B_0 and η, as well as assess whether the observed behavior is consistent with expectations for a merging cluster based on its σ_{RM} profile (see Osinga et al. [94] for this kind of profile study).

Considering all the methods explored, we obtain magnetic field strengths ranging from approximately 0.1 to 11 μG, with values above 2 μG reached under the highly simplified assumptions of magnetic-thermal or magnetic-cosmic ray equipartition.

These values are compatible with other estimations of magnetic fields in radio relics (e.g. Bonafede et al. [14]) and with what is expected in general in galaxy clusters: magnetic fields at the center of merging clusters show usually $\approx \mu$G strengths and are ordered up to scales of $\approx$500 kpc, while in relaxed systems magnetic fields are detected with $\approx$ 10 μG central strengths and turbulence down to scales of a few kpc or less [125].

8

Conclusions

This work presented new JVLA observations at 1.6 GHz and SRT observations at 18.6 GHz of the galaxy cluster MACS J1752+4440 in total intensity and polarization.

In both datasets, the two components of the double radio relic system, located to the north-east and south-west of the cluster center, were clearly detected and analyzed. In the JVLA data, both relics were detected with a signal-to-noise ratio (SNR) of $\gtrsim 3$, while in the SRT observations the northern relic reached an SNR of $\gtrsim 3$, and the southern relic was only marginally detected with an SNR of $\gtrsim 2$.

The total intensity results were incorporated in a spectral fit, which, when complemented with literature data from the GMRT and WSRT, LOFAR images from the LoTSS-2 survey mosaics, and RACS and NVSS images, reveals that the flux density of the two relics follows a power-law behaviour up to 20 GHz. This is consistent with the Diffusive Shock Acceleration theory and with previous results from literature.

The resulting integrated spectral indices are 1.24 ± 0.03 for the NE relic and 1.17 ± 0.03 for the SW relic.

This thesis also reports the first detection of the Sunyaev–Zel'dovich (SZ) effect at ~ 19 GHz. The observed decrement was modeled using a Bayesian retrieval assuming a simple β-model for the intracluster gas density. The derived physical parameters are consistent with expectations for a massive galaxy cluster of $\sim 10^{15}$ M$_\odot$, such as MACS J1752.0+4440. The modeling yielded an average Compton y-parameter of $(2.6 \pm 0.3) \times 10^{-5}$ within a radius of $3'$ from the cluster center. It is important to note that this value may be overestimated due to the use of a simplified spherical β-model, which does not fully account for the finite size and non-spherical structure of the cluster, or for the possible presence of a polytropic temperature profile.

The polarization analysis with SRT data reveals a fractional polarization average of $33 \pm 4\%$ for the northern relic, with peaks of 60% in the external regions.

The JVLA polarization images showed high-quality results, with average fractional polarizations of $31 \pm 3\%$ for the northern relic and $35 \pm 3\%$ for the southern relic. These results were obtained after applying a RM synthesis analysis, since the polarization angles in the JVLA data differed from those in the SRT data, suggesting the presence of Faraday rotation. We obtained RM values primarily in the range from -50 to $+70$ rad m^{-2}. These RM values were used to de-rotate the JVLA polarization vectors. The resulting vectors aligned well with those observed in the SRT data, suggesting that SRT observations successfully recover the intrinsic polarization of the sources.

Finally, we presented preliminary estimates of the magnetic field strength using various approaches. These are highly approximate, as they rely on oversimplified assumptions for the cluster's temperature and density structure—particularly inadequate for a merging system. Nevertheless, the estimated values mostly fall in the range 0.5–5 μG, with an

estimate from the RM profile of $\sim 2\mu G$, consistent with typical magnetic field strengths estimated in radio relics (e.g. Bonafede et al. [14]).

In view of future observations and studies, this work is fundamental for various aspects. First of all, as presented in the introduction, this is only the third relic observed up to ~ 20 GHz, thereby enlarging the current sample by 50%. As mentioned, observations at such high frequencies are crucial to test whether diffusive shock acceleration is a valid mechanism for these structures. Assuming that the correction factor applied to the LOFAR data, based on the point-like source analysis, is accurate—the option we have presented as the most probable given our analysis—the results are compatible with DSA, and are consistent with what was found in previous studies for other relics at these frequencies by Loi et al. [78] and Rajpurohit et al. [107]. However, if the calibrated LOFAR data are instead correct, then a continuous injection (CI) model, or more generally a curved spectrum, may be required to explain these results and to provide an estimate of the break frequency for this particular relic. New observations between 150 MHz and 800 MHz will be particularly interesting in this context.

Studying other relics at these frequencies will also be particularly important to expand the sample and to assess whether this power-law behaviour is common to all relics, or whether it depends, for example, on their morphology. In this regard, analyzing both more complex relics, such as Abell 2256, and relics very similar to MACS1752, such as PSZ1 G108.18-11.5, will be fundamental.

Another aspect to further explore is the use of SRT data at 20 GHz as a probe to investigate the SZ decrement from lower to higher frequencies, for instance with the MISTRAL receiver at 90 GHz, which has now entered its phase of scientific commissioning at the SRT. Observations of the SZ decrement, paired with accurate modeling of clusters in various merger states, represent a powerful alternative to X-ray data for deriving cluster physical parameters, such as density and core radius.

Finally, our results highlight the power of combining radio polarimetry with SZ observations to jointly probe the non-thermal and thermal components of the ICM in merging galaxy clusters, to arrive at a derivation of the strength of magnetic fields in these regions. The upcoming SKA1-Mid, with its Band 2 (0.95–1.76GHz) and Band 5b (8.3–15.3GHz) receivers, will provide a significant improvement in this field, enabling high-sensitivity polarimetric studies at low frequencies and SZ–polarimetry synergy at higher frequencies.
In this context, our work is a fundamental precursor to future multi-frequency studies with next generation radio telescopes.

References

[1] H. Akamatsu, Y. Fujita, and et al. Akahori, T. Properties of the cosmological filament between two clusters: A possible detection of a large-scale accretion shock by Suzaku. *aap*, 606:A1, September 2017. doi: 10.1051/0004-6361/201730497.

[2] A. D. Amaral, T. Vernstrom, and B. M. Gaensler. Constraints on large-scale magnetic fields in the intergalactic medium using cross-correlation methods. *mnras*, 503(2):2913–2926, May 2021. doi: 10.1093/mnras/stab564.

[3] S. Andreon and M. Radovich. Gravity-selected Cluster Samples: A New Take on the Compton-y–Mass Relation. *apj*, 985(1):78, May 2025. doi: 10.3847/1538-4357/adc71e.

[4] J. Bagchi et al. Giant ringlike radio structures around galaxy clusters: Evidence for magnetic fields and merger relics. *Science*, 314:791–795, 2006. doi: 10.1126/science.1131565.

[5] J. et al. Bagchi. Shock acceleration of cosmic rays in large-scale structure formation. *New Astronomy*, 7:249–277, 2002.

[6] Kaustuv Basu, Franco Vazza, Jens Erler, and Martin Sommer. The impact of the SZ effect on cm-wavelength (1-30 GHz) observations of galaxy cluster radio relics. *aap*, 591:A142, July 2016. doi: 10.1051/0004-6361/201527726.

[7] Elia S. Battistelli, Carlo Burigana, Paolo de Bernardis, and et al. Kirillov. Galaxy clusters as probes for cosmology and dark matter. *International Journal of Modern Physics D*, 25(10):1630023, July 2016. doi: 10.1142/S0218271816300238.

[8] Mark Birkinshaw. The Sunyaev-Zel'dovich effect: an update. In Luciano Maiani, Francesco Melchiorri, and Nicola Vittorio, editors, *3K cosmology*, volume 476 of *American Institute of Physics Conference Series*, pages 298–309. AIP, May 1999. doi: 10.1063/1.59334.

[9] Roger Blandford and David Eichler. Particle acceleration at astrophysical shocks: A theory of cosmic ray origin. *physrep*, 154(1):1–75, October 1987. doi: 10.1016/0370-1573(87)90134-7.

[10] George R. Blumenthal and Robert J. Gould. Bremsstrahlung, Synchrotron Radiation, and Compton Scattering of High-Energy Electrons Traversing Dilute Gases. *Reviews of Modern Physics*, 42(2):237–271, January 1970. doi: 10.1103/RevModPhys.42.237.

[11] P. Bolli, A. Orlati, L. Stringhetti, and et al. Orfei. Sardinia Radio Telescope. *Journal of Astronomical Instrumentation*, 4:1550008-880, December 2015. doi: 10.1142/S2251171715500087.

[12] A. Bonafede, L. Feretti, F. Govoni, M. Murgia, and G. Giovannini et al. The coma cluster magnetic field from faraday rotation measures. *Astronomy & Astrophysics*, 503(2):707–719, 2009.

[13] A. Bonafede, M. Brüggen, R. van Weeren, and F. et al. Vazza. Discovery of radio haloes and double relics in distant MACS galaxy clusters: clues to the efficiency of particle acceleration. *mnras*, 426(1):40–56, October 2012. doi: 10.1111/j.1365-2966.2012.21570.x.

[14] A. Bonafede, F. Vazza, M. Brüggen, and M.et al. Murgia. Measurements and simulation of Faraday rotation across the Coma radio relic. *mnras*, 433(4):3208–3226, August 2013. doi: 10.1093/mnras/stt960.

[15] A. Bonafede, G. Brunetti, L. Rudnick, F. Vazza, and H. et al. Bourdin. The Coma Cluster at LOFAR Frequencies. II. The Halo, Relic, and a New Accretion Relic. *apj*, 933(2):218, July 2022. doi: 10.3847/1538-4357/ac721d.

[16] A. Botteon, F. Gastaldello, G. Brunetti, and D. Dallacasa. Radio shocks in el gordo and the toothbrush cluster: constraining cosmic-ray acceleration with x-ray and radio observations. *MNRAS*, 463(2):1534–1544, 2016. doi: 10.1093/mnras/stw2106.

[17] A. Botteon, G. Brunetti, D. Ryu, and S. Roh. Shock acceleration efficiency in radio relics. *aap*, 634: A64, February 2020. doi: 10.1051/0004-6361/201936216.

[18] M. A. Brentjens. The polarization of the radio relic in abell 2256. *Astronomy & Astrophysics*, 489: 69–84, 2008.

[19] M. A. Brentjens and A. G. de Bruyn. Faraday rotation measure synthesis. *aap*, 441(3):1217–1228, October 2005. doi: 10.1051/0004-6361:20052990.

[20] Gianfranco Brunetti and Thomas W. Jones. Cosmic Rays in Galaxy Clusters and Their Nonthermal Emission. *International Journal of Modern Physics D*, 23(4):1430007-98, March 2014. doi: 10.1142/S0218271814300079.

[21] Franco Buffa, Giampaolo Serra, Pietro Bolli, Antonietta Fara, G.L. Deiana, F. Nasir, Carluccio Castiglia, and Alessandro Delitala. K-band system temperature forecast for the sardinia radio telescope, 04 2016.

[22] Ettore Carretti, V. Vacca, S. P. O'Sullivan, and et al. Heald. Magnetic field strength in cosmic web filaments. *mnras*, 512(1):945–959, May 2022. doi: 10.1093/mnras/stac384.

[23] CASA Team, Ben Bean, Sanjay Bhatnagar, Sandra Castro, and Jennifer et al. Donovan Meyer. CASA, the Common Astronomy Software Applications for Radio Astronomy. *pasp*, 134(1041):114501, November 2022. doi: 10.1088/1538-3873/ac9642.

[24] A. Cavaliere and R. Fusco-Femiano. X-rays from hot plasma in clusters of galaxies. *Astronomy and Astrophysics*, 49:137–144, 1976.

[25] A. Cavaliere and R. Fusco-Femiano. The distribution of hot gas in clusters of galaxies. *Astronomy and Astrophysics*, 70:677–686, 1978.

[26] E. Churazov, R. Sunyaev, W. Forman, and H. Böhringer. Cooling flows as a calorimeter of active galactic nucleus mechanical power. *mnras*, 332(3):729–734, May 2002. doi: 10.1046/j.1365-8711.2002.05332.x.

[27] T. E. Clarke and T. A. Enßlin. Magnetic fields and shock waves in the merging cluster a2256. *Astronomical Journal*, 131:2900–2910, 2006.

[28] J. J. Condon, W. D. Cotton, E. W. Greisen, Q. F. Yin, R. A. Perley, G. B. Taylor, and J. J. Broderick. The NRAO VLA Sky Survey. *aj*, 115(5):1693–1716, May 1998. doi: 10.1086/300337.

[29] F. de Gasperin and et al. Gently re-energised tails (greets) in galaxy clusters. *Astronomy & Astrophysics*, 597:A15, 2017.

[30] F. de Gasperin, L. Rudnick, A. Finoguenov, and D. et al. Wittor. MeerKAT view of the diffuse radio sources in Abell 3667 and their interactions with the thermal plasma. *aap*, 659:A146, March 2022. doi: 10.1051/0004-6361/202142658.

[31] F. de Gasperin et al. The discovery of the double radio relics in the planck cluster psz1 g108.18–11.53. *MNRAS*, 446(1):L26–L30, 2015. doi: 10.1093/mnrasl/slu164.

[32] F. et al. de Gasperin. The steep-spectrum radio relic in abell 2256: evidence for a pre-existing population of relativistic electrons. *Monthly Notices of the Royal Astronomical Society*, 444:3130–3143, 2014.

[33] K. Dolag, S. Schindler, F. Govoni, and L. Feretti. Correlation of the magnetic field and the intra-cluster gas density in galaxy clusters. *aap*, 378:777–786, November 2001. doi: 10.1051/0004-6361:20011219.

[34] J. M. F. Donnert, A. Stroe, G. Brunetti, D. Hoang, and H. Roettgering. Magnetic field evolution in giant radio relics using the example of CIZA J2242.8+5301. *mnras*, 462(2):2014–2032, October 2016. doi: 10.1093/mnras/stw1792.

[35] L. Oc. Drury. REVIEW ARTICLE: An introduction to the theory of diffusive shock acceleration of energetic particles in tenuous plasmas. *Reports on Progress in Physics*, 46(8):973–1027, August 1983. doi: 10.1088/0034-4885/46/8/002.

[36] K. S. et al. Dwarakanath. Diffuse radio emission in abell 168. *Monthly Notices of the Royal Astronomical Society*, 475:3114–3121, 2018.

[37] H. Ebeling, A. C. Edge, and J. P. Henry. MACS: A Quest for the Most Massive Galaxy Clusters in the Universe. *apj*, 553(2):668–676, June 2001. doi: 10.1086/320958.

[38] A. C. Edge, H. Ebeling, M. Bremer, and H. et al. Röttgering. The discovery of two distant, massive clusters of galaxies in the ROSAT All-Sky Survey. *mnras*, 339(4):913–924, March 2003. doi: 10.1046/j.1365-8711.2003.06270.x.

[39] T. A. Enßlin and Gopal-Krishna. Reviving fossil radio plasma in clusters of galaxies by adiabatic compression in environmental shock waves. *aap*, 366:26–34, January 2001. doi: 10.1051/0004-6361:20000198.

[40] Torsten A. Enßlin and Gopal-Krishna. Are cluster radio relics revived fossil radio cocoons? In Robert A. Laing and Katherine M. Blundell, editors, *Particles and Fields in Radio Galaxies Conference*, volume 250 of *Astronomical Society of the Pacific Conference Series*, page 454, January 2001. doi: 10.48550/arXiv.astro-ph/0010600.

[41] Torsten A. Ensslin, Peter L. Biermann, Ulrich Klein, and Sven Kohle. Cluster radio relics as a tracer of shock waves of the large-scale structure formation. *aap*, 332:395–409, April 1998. doi: 10.48550/arXiv.astro-ph/9712293.

[42] A. Bonafede et al. Faraday rotation measure synthesis of abell 2255. *Astronomy & Astrophysics*, 503: 707–719, 2009.

[43] Luigina Feretti, Gabriele Giovannini, Federica Govoni, and Matteo Murgia. Clusters of galaxies: observational properties of the diffuse radio emission. *A&ARv*, 20:54, May 2012. doi: 10.1007/s00159-012-0054-z.

[44] E. Fermi. An hypothesis on the origin of the cosmic radiation. *Il Nuovo Cimento*, 6(3):317–323, January 1949. doi: 10.1007/BF02822004.

[45] K. Finner et al. Multiwavelength analysis of plck g287.0+32.9: A massive cluster at z=0.39 with double radio relics. *ApJ*, 851:46, 2017. doi: 10.3847/1538-4357/aa9983.

[46] Kyle Finner, Kim HyeongHan, M. James Jee, and Wittmanet al. Exemplary Merging Clusters: Weak-lensing and X-Ray Analysis of the Double Radio Relic, Merging Galaxy Clusters MACS J1752.0+4440 and ZWCL 1856.8+6616. *apj*, 918(2):72, September 2021. doi: 10.3847/1538-4357/ac0d00.

[47] A. Finoguenov et al. X-ray confirmation of a shock in the galaxy cluster a3667. *MNRAS*, 403: 2063–2070, 2010. doi: 10.1111/j.1365-2966.2009.16210.x.

[48] Daniel Foreman-Mackey, David W. Hogg, Dustin Lang, and Jonathan Goodman. emcee: The MCMC Hammer. *pasp*, 125(925):306, March 2013. doi: 10.1086/670067.

[49] Samuel J. George, Jeroen M. Stil, and Ben W. Keller. Detection Thresholds and Bias Correction in Polarized Intensity. *pasa*, 29(3):214–220, October 2012. doi: 10.1071/AS11027.

[50] G. Giovannini, L. Feretti, and C. Stanghellini. Radio structures of the coma cluster. *Astronomy and Astrophysics*, 252:528–534, 1991.

[51] N. Golovich et al. Optical and spectroscopic survey of the fields of merging galaxy clusters. *ApJ*, 838 (2):110, 2017. doi: 10.3847/1538-4357/aa63f7.

[52] Nathan Golovich, William A. Dawson, David Wittman, et al. High-resolution spectroscopy of massive galaxy cluster mergers: Constraints on the dynamics of the 'el gordo' merger. *The Astrophysical Journal*, 882(1):69, 2019. doi: 10.3847/1538-4357/ab2f9a.

[53] F. Govoni, M. Murgia, V. Vacca, F. Loi, M. Girardi, and F. et al. Gastaldello. Sardinia Radio Telescope observations of Abell 194. The intra-cluster magnetic field power spectrum. *aap*, 603:A122, July 2017. doi: 10.1051/0004-6361/201630349.

[54] F. Govoni, E. Orrù, A. Bonafede, and et al. Iacobelli. A radio ridge connecting two galaxy clusters in a filament of the cosmic web. *Science*, 364(6444):981–984, June 2019. doi: 10.1126/science.aat7500.

[55] F. et al. Govoni. A multi-frequency study of the radio halo in abell 115. *Astronomy and Astrophysics*, 376:803–817, 2001.

[56] Federica Govoni, Luigina Feretti, Gabriele Giovannini, Daniele Dallacasa, and Gregory B. Taylor. Magnetic Fields in Clusters of Galaxies. In Marat Gilfanov, Rashid Sunyaev, and Eugene Chura-zov, editors, *Lighthouses of the Universe: The Most Luminous Celestial Objects and Their Use for Cosmology*, page 78, January 2002. doi: 10.1007/10856495_10.

[57] Ji-Hoon Ha, Dongsu Ryu, and Hyesung Kang. Properties of Merger Shocks in Merging Galaxy Clusters. *apj*, 857(1):26, April 2018. doi: 10.3847/1538-4357/aab4a2.

[58] D. N. Hoang, X. Zhang, C. Stuardi, and T. W. et al. Shimwell. A 3.5 Mpc long radio relic in the galaxy cluster ClG 0217+70. *aap*, 656:A154, December 2021. doi: 10.1051/0004-6361/202141428.

[59] J. A. Högbom. Aperture Synthesis with a Non-Regular Distribution of Interferometer Baselines. *aaps*, 15:417, June 1974.

[60] A. W. Hotan, J. D. Bunton, A. P. Chippendale, M. Whiting, and J. et al. Tuthill. Australian square kilometre array pathfinder: I. system description. *pasa*, 38:e009, March 2021. doi: 10.1017/pasa.2021. 1.

[61] W. J. Jaffe and G. C. Perola. Dynamical Models of Tailed Radio Sources in Clusters of Galaxies. *aap*, 26:423, August 1973.

[62] M. J. Jee et al. Weak-lensing analysis of the merging galaxy cluster zwcl 0008.8+5215. *ApJ*, 802:46, 2015. doi: 10.1088/0004-637X/802/1/46.

[63] M. J. Jee et al. The merging galaxy cluster ciza j2242.8+5301 (sausage): Mass distribution and geometry of a binary merger. *ApJ*, 817:179, 2016. doi: 10.3847/0004-637X/817/2/179.

[64] M. Johnston-Hollitt. Magnetic fields in merging clusters. *PhD thesis, University of Adelaide*, 2003.

[65] J. Jonas and MeerKAT Team. The MeerKAT Radio Telescope. In *MeerKAT Science: On the Pathway to the SKA*, page 1, January 2016. doi: 10.22323/1.277.0001.

[66] J. S. Kaastra, C. Ferrigno, T. Tamura, and et al. Paerels. XMM-Newton observations of the cluster of galaxies Sérsic 159-03. *aap*, 365:L99–L103, January 2001. doi: 10.1051/0004-6361:20000041.

[67] R. Kale et al. A new sample of giant radio halos from the gmrt radio halo survey. *A&A*, 579:A92, 2015. doi: 10.1051/0004-6361/201424896.

[68] Hyesung Kang and Dongsu Ryu. Re-acceleration of Non-thermal Particles at Weak Cosmological Shock Waves. *apj*, 734(1):18, June 2011. doi: 10.1088/0004-637X/734/1/18.

[69] Hyesung Kang and Dongsu Ryu. Radio Spectra from Shock Accelerated Electrons in the Cluster Outskirts. In *IAU General Assembly*, volume 29, page 2227971, August 2015.

[70] N. S. Kardashev. Nonstationarity of Spectra of Young Sources of Nonthermal Radio Emission. *azh*, 39:393, January 1962.

[71] J. C. Kempner and et al. A new class of radio phoenixes. In *The Riddle of Cooling Flows in Galaxies and Clusters of Galaxies*. EAS Publications Series, 2004.

[72] J. C. Kempner and C. L. Sarazin. A merger shock in the galaxy cluster abell 1240. *ApJ*, 548:639–651, 2001. doi: 10.1086/319005.

[73] M. Kierdorf and et al. High-frequency radio polarization observations of the sausage relic. *Astronomy & Astrophysics*, 600:A18, 2017.

[74] Lev Davidovich Landau and E. M. Lifshitz. *Fluid mechanics*. 1959.

[75] W. Lee, A. Pillepich, J. ZuHone, and et al. Nelson. Radio relics in massive galaxy cluster mergers in the TNG-Cluster simulation. *aap*, 686:A55, June 2024. doi: 10.1051/0004-6361/202348194.

[76] R. R. Lindner et al. Diffuse radio emission in the high-redshift merging cluster act-cl j0102–4915 ("el gordo") observed with the gmrt and the vla. *ApJ*, 786(1):49, 2014. doi: 10.1088/0004-637X/786/1/49.

[77] F. Loi and et al. High-frequency observations of the toothbrush relic. *Monthly Notices of the Royal Astronomical Society*, 472(3):3605–3616, 2017.

[78] F. Loi, M. Murgia, V. Vacca, and F. et al. Govoni. Erratum: Spectropolarimetric observations of the CIZA J2242.8+5301 northern radio relic: no evidence of high-frequency steepening. *mnras*, 501(3): 3183–3183, March 2021. doi: 10.1093/mnras/staa3947.

[79] Maxim Markevitch and Alexey Vikhlinin. Shocks and cold fronts in galaxy clusters. *physrep*, 443(1): 1–53, May 2007. doi: 10.1016/j.physrep.2007.01.001.

[80] D. McConnell, C. L. Hale, E. Lenc, J. K. Banfield, George Heald, and et al. Hotan. The Rapid ASKAP Continuum Survey I: Design and first results. *pasa*, 37:e048, November 2020. doi: 10.1017/pasa.2020.41.

[81] B. R. McNamara and P. E. J. Nulsen. Mechanical feedback from active galactic nuclei in galaxies, groups and clusters. *New Journal of Physics*, 14(5):055023, May 2012. doi: 10.1088/1367-2630/14/5/055023.

[82] A. Melis, R. Concu, A. Trois, and A. et al. Possenti. SArdinia Roach2-based Digital Architecture for Radio Astronomy (SARDARA). *Journal of Astronomical Instrumentation*, 7(1):1850004, March 2018. doi: 10.1142/S2251171718500046.

[83] F. Menanteau et al. The atacama cosmology telescope: Act-cl j0102-4915 'el gordo', a massive merging cluster at redshift 0.87. *ApJ*, 748(1):7, 2012. doi: 10.1088/0004-637X/748/1/7.

[84] S. M. Molnar et al. Numerical simulations of merging galaxy clusters: Effects of mass ratio, impact parameter, and velocity on the formation of double radio relics. *ApJ*, 846:60, 2017. doi: 10.3847/1538-4357/aa7d12.

[85] M. Murgia, C. Fanti, R. Fanti, and L. at al. Gregorini. Synchrotron spectra and ages of compact steep spectrum radio sources. *aap*, 345:769–777, May 1999.

[86] M. Murgia, F. Govoni, L. Feretti, and et al. Giovannini. Magnetic fields and Faraday rotation in clusters of galaxies. *aap*, 424:429–446, September 2004. doi: 10.1051/0004-6361:20040191.

[87] M. Murgia, F. Govoni, E. Carretti, and et al. Melis. Sardinia Radio Telescope wide-band spectral-polarimetric observations of the galaxy cluster 3C 129. *mnras*, 461(4):3516–3532, October 2016. doi: 10.1093/mnras/stw1552.

[88] M. Murgia, F. Govoni, and V.et al. Vacca. Sardinia Radio Telescope observations of the Coma cluster. *mnras*, 528(4):6470–6495, March 2024. doi: 10.1093/mnras/stae436.

[89] S. E. et al. Nuza. Radio relics in simulated galaxy clusters: Insights from the music-2 sample. *Monthly Notices of the Royal Astronomical Society*, 470:240–261, 2017.

[90] A. R. Offringa, B. McKinley, N. Hurley-Walker, and F.et al. Briggs. WSCLEAN: an implementation of a fast, generic wide-field imager for radio astronomy. *mnras*, 444(1):606–619, October 2014. doi: 10.1093/mnras/stu1368.

[91] N. Okabe et al. Subaru weak-lensing survey of dark matter subhalos in the coma cluster: subhalo mass function and statistical properties. *PASJ*, 67:86, 2015. doi: 10.1093/pasj/psv061.

[92] N. Oppermann, H. Junklewitz, G. Robbers, and M. R. et al. Bell. An improved map of the Galactic Faraday sky. *aap*, 542:A93, June 2012. doi: 10.1051/0004-6361/201118526.

[93] A. Orfei, L. Carbonaro, A. Cattani, and et al. Cremonini. A Multi-Feed Receiver in the 18 to 26.5 GHz Band for Radio Astronomy. *IEEE Antennas and Propagation Magazine*, 52(4):62–72, August 2010. doi: 10.1109/MAP.2010.5638236.

[94] E. Osinga, R. J. van Weeren, L. Rudnick, and et al. Andrade-Santos. Probing cluster magnetism with embedded and background radio sources in Planck clusters. *aap*, 694:A44, February 2025. doi: 10.1051/0004-6361/202451885.

[95] F. N. Owen and et al. Observations of faraday rotation in abell clusters. *Astrophysical Journal*, 794 (1):24, 2014.

[96] T. Ozawa and et al. Low-frequency observations of cluster radio relics. *PASJ*, 67(5):81, 2015.

[97] A. G. Pacholczyk. *Radio astrophysics. Nonthermal processes in galactic and extragalactic sources.* 1970.

[98] A. Paiella, F. Cacciotti, G. Isopi, and et al. Barbavara. The kinetic inductance detectors for the MISTRAL instrument: Installation and characterization at the Sardinia Radio Telescope. *Nuclear Instruments and Methods in Physics Research A*, 1075:170373, June 2025. doi: 10.1016/j.nima.2025. 170373.

[99] C. J. J. Pearce and et al. Magnetic field alignment and turbulence in the toothbrush relic. *Monthly Notices of the Royal Astronomical Society*, 466(3):2736–2748, 2017.

[100] R. A. Perley and B. J. Butler. An Accurate Flux Density Scale from 1 to 50 GHz. *apjs*, 204(2):19, February 2013. doi: 10.1088/0067-0049/204/2/19.

[101] R. F. Pizzo and et al. Faraday tomography of abell 2255 with wsrt. *Astronomy & Astrophysics*, 525: A104, 2011.

[102] Planck Collaboration. Planck 2015 results. XXVII. The second Planck catalogue of Sunyaev-Zeldovich sources. *aap*, 594:A27, September 2016. doi: 10.1051/0004-6361/201525823.

[103] I. Prandoni, M. Murgia, A. Tarchi, and et al. Burgay. The Sardinia Radio Telescope . From a technological project to a radio observatory. *aap*, 608:A40, December 2017. doi: 10.1051/0004-6361/ 201630243.

[104] C. R. Purcell, C. L. Van Eck, J. West, X. H. Sun, and B. M. Gaensler. RM-Tools: Rotation measure (RM) synthesis and Stokes QU-fitting. Astrophysics Source Code Library, record ascl:2005.003, May 2020.

[105] D. Puy, L. Grenacher, Ph. Jetzer, and M. Signore. Asphericity of galaxy clusters and the Sunyaev-Zel'dovich effect. *aap*, 363:415–424, November 2000. doi: 10.48550/arXiv.astro-ph/0009114.

[106] K. Rajpurohit, M. Hoeft, F. Vazza, and L. et al. Rudnick. New mysteries and challenges from the Toothbrush relic: wideband observations from 550 MHz to 8 GHz. *aap*, 636:A30, April 2020. doi: 10.1051/0004-6361/201937139.

[107] K. Rajpurohit, F. Vazza, M. Hoeft, and F. et al. Loi. A perfect power-law spectrum even at the highest frequencies: The Toothbrush relic. *aap*, 642:L13, October 2020. doi: 10.1051/0004-6361/202039165.

[108] K. Rajpurohit, R. J. van Weeren, M. Hoeft, and et al. Vazza. Deep Low-frequency Radio Observations of A2256. I. The Filamentary Radio Relic. *apj*, 927(1):80, March 2022. doi: 10.3847/1538-4357/ac4708.

[109] Michael Reefe, Michael McDonald, Marios Chatzikos, and et al. Seebeck. Directly imaging the cooling flow in the Phoenix cluster. *nature*, 638(8050):360–364, February 2025. doi: 10.1038/ s41586-024-08369-x.

[110] A. Remijan, A. Biggs, P. A. Cortes, and B.et al. Dent. ALMA Technical Handbook,ALMA Doc. 7.3, ver. 1.1. 2019, ALMA Technical Handbook,ALMA Doc. 7.3, ver. 1.1ISBN 978-3-923524-66-2, June 2019.

[111] R. B. Rengelink, Y. Tang, A. G. de Bruyn, and G.et al. Miley. The Westerbork Northern Sky Survey (WENSS), I. A 570 square degree Mini-Survey around the North Ecliptic Pole. *aaps*, 124:259–280, August 1997. doi: 10.1051/aas:1997358.

[112] Timothy Robishaw and Carl Heiles. The Measurement of Polarization in Radio Astronomy. In Alex Wolszczan, editor, *The WSPC Handbook of Astronomical Instrumentation, Volume 1: Radio Astronomical Instrumentation*, pages 127–158. 2021. doi: 10.1142/9789811203770_0006.

[113] H. J. A. et al. Röttgering. A radio halo in a3667. *Monthly Notices of the Royal Astronomical Society*, 290:577–584, 1997.

[114] C. L. Sarazin. *X-ray Emission from Clusters of Galaxies*. Cambridge University Press, 1988.

[115] C. L. Sarazin and J. N. Bahcall. X-ray line emission for clusters of galaxies. II. Numerical models. *apjs*, 34:451–467, August 1977. doi: 10.1086/190457.

[116] Craig L. Sarazin. The Physics of Cluster Mergers. In L. Feretti, I. M. Gioia, and G. Giovannini, editors, *Merging Processes in Galaxy Clusters*, volume 272 of *Astrophysics and Space Science Library*, pages 1–38, June 2002. doi: 10.1007/0-306-48096-4_1.

[117] T. W. Shimwell, H. J. A. Röttgering, P. N. Best, W. L. Williams, and et al. Dijkema. The LOFAR Two-metre Sky Survey. I. Survey description and preliminary data release. *aap*, 598:A104, February 2017. doi: 10.1051/0004-6361/201629313.

[118] S. W. et al. Skillman. Cosmological magnetohydrodynamic simulations of radio relics in galaxy clusters. *Astrophysical Journal*, 735:96, 2011.

[119] S. W. et al. Skillman. Radio relics in cosmological simulations. *Astrophysical Journal*, 765:21, 2013.

[120] David C Smolinski, Denis Wittor, Franco Vazza, and Marcus Brüggen. A multishock scenario for the formation of radio relics. *Monthly Notices of the Royal Astronomical Society*, 526(3):4234–4244, 10 2023. ISSN 0035-8711. doi: 10.1093/mnras/stad3009. URL https://doi.org/10.1093/mnras/stad3009.

[121] Andra Stroe, Jeremy J. Harwood, Martin J. Hardcastle, and Huub J. A. Röttgering. Spectral age modelling of the 'Sausage' cluster radio relic. *mnras*, 445(2):1213–1222, December 2014. doi: 10.1093/mnras/stu1839.

[122] Andra Stroe, Timothy Shimwell, Clare Rumsey, and Reinout et al. van Weeren. The widest frequency radio relic spectra: observations from 150 MHz to 30 GHz. *mnras*, 455(3):2402–2416, January 2016. doi: 10.1093/mnras/stv2472.

[123] S. J. Tingay, R. Goeke, J. D. Bowman, and D. et al. Emrich. The Murchison Widefield Array: The Square Kilometre Array Precursor at Low Radio Frequencies. *pasa*, 30:e007, January 2013. doi: 10.1017/pasa.2012.007.

[124] M. Trasatti, H. Akamatsu, L. Lovisari, and U. et al. Klein. The radio relic in Abell 2256: overall spectrum and implications for electron acceleration. *aap*, 575:A45, March 2015. doi: 10.1051/0004-6361/201423972.

[125] Valentina Vacca, Matteo Murgia, Federica Govoni, and et al. Enßlin. Magnetic Fields in Galaxy Clusters and in the Large-Scale Structure of the Universe. *Galaxies*, 6(4):142, December 2018. doi: 10.3390/galaxies6040142.

[126] M. P. van Haarlem, M. W. Wise, A. W. Gunst, and G. et al. Heald. LOFAR: The LOw-Frequency ARray. *aap*, 556:A2, August 2013. doi: 10.1051/0004-6361/201220873.

[127] R. J. van Weeren and et al. A shock front in the toothbrush cluster. *Astronomy & Astrophysics*, 546: A124, 2012.

[128] R. J. van Weeren, H. J. A. Röttgering, M. Brüggen, and M. Hoeft. Particle acceleration on megaparsec scales in a merging galaxy cluster. *Science*, 330(6002):347–349, 2010. doi: 10.1126/science.1194293.

[129] R. J. van Weeren, H. J. A. Röttgering, M. Brüggen, and M. Hoeft. Particle acceleration on megaparsec scales in a merging galaxy cluster. *Science*, 330:347–349, 2010.

[130] R. J. van Weeren, A. Bonafede, H. Ebeling, and A.et al. Edge. Diffuse radio emission in MACS J1752.0+4440. *mnras*, 425(1):L36–L40, September 2012. doi: 10.1111/j.1745-3933.2012.01301.x.

[131] R. J. van Weeren, G. Brunetti, M. Brüggen, and et al. Andrade-Santos. Lofar, vla, and chandra observations of the toothbrush galaxy cluster. *The Astrophysical Journal*, 818(2):204, feb 2016. doi: 10.3847/0004-637X/818/2/204. URL https://dx.doi.org/10.3847/0004-637X/818/2/204.

[132] R. J. van Weeren, F. de Gasperin, H. Akamatsu, and M. et al. Brüggen. Diffuse Radio Emission from Galaxy Clusters. *ssr*, 215(1):16, February 2019. doi: 10.1007/s11214-019-0584-z.

[133] R. J. van Weeren et al. Radio observations of the galaxy cluster ciza j2242.8+5301 with the gmrt and wsrt. *A&A*, 533:A35, 2011. doi: 10.1051/0004-6361/201117118.

[134] R. J. van Weeren et al. The discovery of double radio relics in the merging galaxy cluster zwcl 0008.8+5215. *ApJL*, 726(1):L8, 2011. doi: 10.1088/2041-8205/726/1/L8.

[135] R. J. et al. van Weeren. The complex diffuse radio emission in zwcl 2341.1+0000. *Astronomy & Astrophysics*, 506:1083–1099, 2009.

[136] F. Vazza, M. Brüggen, D. Wittor, and C. et al. Gheller. Constraining the efficiency of cosmic ray acceleration by cluster shocks. *mnras*, 459(1):70–83, June 2016. doi: 10.1093/mnras/stw584.

[137] F. et al. Vazza. Turbulent motions and shocks waves in galaxy clusters simulated with adaptive mesh refinement. *Monthly Notices of the Royal Astronomical Society*, 421:1868–1880, 2012.

[138] W. Voges, B. Aschenbach, Th. Boller, and H. et al. Bräuninger. The ROSAT all-sky survey bright source catalogue. *aap*, 349:389–405, September 1999. doi: 10.48550/arXiv.astro-ph/9909315.

[139] Thomas L. Wilson, Kristen Rohlfs, and Susanne Hüttemeister. *Tools of Radio Astronomy*. 2013. doi: 10.1007/978-3-642-39950-3.

[140] D. Wittor, M. Hoeft, F. Vazza, M. Brüggen, and P. Domínguez-Fernández. Polarization of radio relics in galaxy clusters. *mnras*, 490(3):3987–4006, December 2019. doi: 10.1093/mnras/stz2715.

[141] D. et al. Wittor. Cosmic-ray acceleration at structure formation shocks in magnetized cosmological simulations. *Monthly Notices of the Royal Astronomical Society*, 464:4448–4460, 2017.

Appendix

A. Polarization in radio signals

The polarization of a radio wave is defined by the motion of its electric field vector as a function of time within a plane perpendicular to the direction of propagation [112]. That plane is known as the *plane of polarization*, and the general shape that the electric field traces with time is an ellipse. We can quantify this polarization ellipse in terms of any orthonormal basis in the plane of polarization; in radio astronomy, we commonly encounter two: the standard Cartesian linear basis and a basis of circularly rotating unit vectors of opposite handedness.

The electric field vector of a monochromatic light wave traveling along the $+\hat{z}$ direction can be written in terms of both a linear and a circular set of orthonormal bases:

$$\vec{E}(z,t) = \vec{E}_0 e^{i(2\pi\nu t - kz)} = (E_x\hat{x} + E_y\hat{y})e^{i(2\pi\nu t - kz)} = (E_R\hat{R} + E_L\hat{L})e^{i(2\pi\nu t - kz)}, \tag{8.1}$$

where $\hat{R} = (\hat{x} - i\hat{y})/\sqrt{2}$ and $\hat{L} = (\hat{x} + i\hat{y})/\sqrt{2}$ are the unit vectors for IEEE right-hand circular polarization (RCP) and left-hand circular polarization (LCP), respectively. As seen from an observer located at $z > 0$ looking back toward the origin, IEEE RCP appears to rotate counterclockwise with time, while IEEE LCP rotates clockwise. At a given position z along the direction of propagation (let us take $z = 0$ for simplicity), the tip of the electric field vector $\vec{E}$ traces out an ellipse in time. In the linear basis, the orthogonal components of the electric field are given by:

$$E_x(t) = E_{0x}e^{i(2\pi\nu t + \phi_x)}, \quad E_y(t) = E_{0y}e^{i(2\pi\nu t + \phi_y)}, \tag{8.2}$$

or in the circular basis by:

$$E_R(t) = E_{0R}e^{i(2\pi\nu t + \phi_R)}, \quad E_L(t) = E_{0L}e^{i(2\pi\nu t + \phi_L)}. \tag{8.3}$$

These components define the polarization ellipse described earlier. While many treatments of polarization ignore the absolute phase (an approximation that must be avoided when working with interferometers), it is common to define the relative phase difference as $\Delta\phi \equiv \phi_y - \phi_x$.

The orientation of the major axis of the polarization ellipse, denoted by the angle χ with respect to the x-axis, is given by:

$$\tan 2\chi = \frac{2E_{0x}E_{0y}\cos(\phi_y - \phi_x)}{E_{0x}^2 - E_{0y}^2} = \tan(\phi_R - \phi_L), \quad 0° \leq \chi \leq 180°. \tag{8.4}$$

Astronomical radio signals are, in general, partially polarized. To describe such signals, we the Stokes parameters are used.

The Stokes parameters are typically denoted as I, Q, U, and V in astronomical measurements. Because they can be conveniently manipulated using matrix algebra, they are often grouped into the Stokes vector:

$$\vec{S} = \begin{bmatrix} S_0 \\ S_1 \\ S_2 \\ S_3 \end{bmatrix} \equiv \begin{bmatrix} I \\ Q \\ U \\ V \end{bmatrix} \tag{8.5}$$

The Stokes parameters are defined in terms of the intensities of orthogonal polarization states, such as $(I_{0°}, I_{90°})$, $(I_{+45°}, I_{-45°})$, and $(I_{\mathrm{RCP}}, I_{\mathrm{LCP}})$:

- **Stokes** I: Total intensity. It is the sum of the intensities of any two orthogonal polarization components:

$$I \equiv I_{\text{tot}} \equiv I_{0°} + I_{90°} \equiv I_{+45°} + I_{-45°} \equiv I_{\text{RCP}} + I_{\text{LCP}}$$

- **Stokes** Q: Difference in intensities between horizontal and vertical linear polarizations:

$$Q \equiv I_{0°} - I_{90°}$$

A positive Q indicates excess horizontal polarization; negative Q indicates excess vertical.

- **Stokes** U: Difference between linear polarizations at $+45°$ and $-45°$:

$$U \equiv I_{+45°} - I_{-45°}$$

Positive U implies a preference for $+45°$ polarization, and negative U implies $-45°$.

- **Stokes** V: Difference between RCP and LCP intensities:

$$V \equiv I_{\text{RCP}} - I_{\text{LCP}}$$

A positive V indicates right-circular polarization (IEEE convention); negative V indicates left-circular.

The *degree of polarization* or fractional polarization is given by:

$$p = \frac{I_{\text{pol}}}{I_{\text{tot}}} = \frac{\sqrt{Q^2 + U^2 + V^2}}{I}, \quad 0 \le p \le 1 \tag{8.6}$$

The fractional linear and circular polarizations are:

$$p_{\text{lin}} = \frac{\sqrt{Q^2 + U^2}}{I}, \quad 0 \le p_{\text{lin}} \le 1 \tag{8.7}$$

$$p_{\text{cir}} = \frac{V}{I}, \quad -1 \le p_{\text{cir}} \le 1 \tag{8.8}$$

When combining or smoothing polarized signals, one must operate directly on the Stokes parameters—not on fractional polarization, linearly polarized intensities, or polarization angles.

The Stokes parameters can also be written in terms of the time-averaged products of electric field components:

$$I = \langle E_x \overline{E_x} \rangle + \langle E_y \overline{E_y} \rangle = \langle E_R \overline{E_R} \rangle + \langle E_L \overline{E_L} \rangle \tag{8.9}$$

$$Q = \langle E_x \overline{E_x} \rangle - \langle E_y \overline{E_y} \rangle = \langle E_R \overline{E_L} \rangle + \langle E_L \overline{E_R} \rangle \tag{8.10}$$

$$U = \langle E_x \overline{E_y} \rangle + \langle E_y \overline{E_x} \rangle = -i(\langle E_R \overline{E_L} \rangle - \langle E_L \overline{E_R} \rangle) \tag{8.11}$$

$$V = -i(\langle E_x \overline{E_y} \rangle - \langle E_y \overline{E_x} \rangle) = \langle E_R \overline{E_R} \rangle - \langle E_L \overline{E_L} \rangle \tag{8.12}$$

Substituting from the component forms of the electric field, we obtain the commonly used expressions:

$$I = \langle E_{0x}^2 \rangle + \langle E_{0y}^2 \rangle = \langle E_{0R}^2 \rangle + \langle E_{0L}^2 \rangle \tag{8.13}$$

$$Q = \langle E_{0x}^2 \rangle - \langle E_{0y}^2 \rangle = 2\langle E_{0R} E_{0L} \rangle \cos(\phi_R - \phi_L) \tag{8.14}$$

$$U = 2\langle E_{0x} E_{0y} \rangle \cos(\phi_y - \phi_x) = 2\langle E_{0R} E_{0L} \rangle \sin(\phi_R - \phi_L) \tag{8.15}$$

$$V = -2\langle E_{0x} E_{0y} \rangle \sin(\phi_y - \phi_x) = \langle E_{0R}^2 \rangle - \langle E_{0L}^2 \rangle \tag{8.16}$$

From these expressions, the angle χ that the polarization ellipse makes with the x-axis—known as the polarization angle—can be calculated as:

$$\chi = \frac{1}{2}\tan^{-1}\left(\frac{U}{Q}\right), \quad 0° \leq \chi \leq 180° \tag{8.17}$$

Note that χ describes adirection, not an orientation. It ranges over 180° and is typically visualized as a line segment on the sky representing the amplitude and orientation of linear polarization. While these line segments are often referred to as "polarization vectors," the term "*segtor*" has been suggested to reflect the lack of inherent directionality.

The images of the polarized intensity P are derived from the Stokes parameters:

$$P = \sqrt{Q^2 + U^2}. \tag{8.18}$$

$$\tag{8.19}$$

when we assume for our case V=0 since circular polarization is negligible for most of extragalactic sources, and for the object of the observations presented in this work.

The fractional polarization is obtained deriving the polarized intensity P for the total intensity I.

The SRT feeds are circlar polarization feeds. In the circular system, the linear components (Q and U) are uniquely found in the cross-hand components, while in the linear system, they require all four correlations. This is a major advantage to circular systems, if linear polarization is what you're interested in, as it is in the case of radio relics. Also, calibrator sources are often significantly linearly polarized, but have imperceptible circular polarization, and their polarization is variable and often not known a priori. Therefore, you cannot isolate instrumental effects from intrinsic source polarization, unless you observe a known unpolarized source (rare), or you observe over a wide range of parallactic angles to separate source polarization from instrumental leakage (which takes time). This makes polarization calibration with circular feeds noticeably more straightforward than with linear feeds.

B. The CLEANing algorithm

CLEANing is the most commonly used technique to improve single radio interferometer images. What comes out after calibration, the dirty map, is a representation of the principal solution, but with shortcomings. In addition to its inherent low dynamic range, the dirty map often contains features such as negative intensity artifacts. The CLEAN method approximates the actual but unknown intensity distribution $I(x, y)$ by the superposition of a finite number of point sources with positive intensity A_i placed at positions (x_i, y_i). The goal of CLEAN is to determine the A_i, (x_i, y_i) such that

$$I''(x, y) = \sum_i A_i\, P_D(x - x_i, y - y_i) + I_\varepsilon(x, y), \tag{8.20}$$

where $I''(x, y)$ is the dirty map obtained from the inversion of the visibility function, and PD is the dirty beam. The concept of CLEAN was first devised by Högbom [59]. The algorithm

is most commonly applied in the image plane. It is an iterative method that functions as follows: first, find the peak intensity of the dirty image, then subtract a fraction γ of the dirty beam—centered at the peak position—from the image. This process is repeated n times. The loop gain, $0 < \gamma < 1$, ensures convergence of the iteration, and the process is typically continued until the intensities of the remaining peaks fall below a predefined threshold. The resulting point source model is then convolved with a clean beam, typically a Gaussian with a full width at half power similar to that of the dirty beam [139].